OIL-COATED BUBBLES IN COMPLEX COLLOIDAL SYSTEMS: FUNDAMENTALS AND APPLICATIONS

A Dissertation
Presented to
The Academic Faculty

by

Songcheng Wang

In Partial Fulfillment
of the Requirements for the Degree
Doctor of Philosophy in the
School of Chemical & Biomolecular Engineering

Georgia Institute of Technology
December 2018

OIL-COATED BUBBLES IN COMPLEX COLLOIDAL SYSTEMS: FUNDAMENTALS AND APPLICATIONS

Approved by:

Dr. Sven H. Behrens, Advisor
School of Chemical & Biomolecular Engineering
Georgia Institute of Technology

Dr. Christopher Luettgen
School of Chemical & Biomolecular Engineering
Georgia Institute of Technology

Dr. J. Carson Meredith, Advisor
School of Chemical & Biomolecular Engineering
Georgia Institute of Technology

Dr. Justin Burton
Department of Physics
Emory University

Dr. Yulin Deng
School of Chemical & Biomolecular Engineering
Georgia Institute of Technology

Date Approved: October 12th, 2018

To my families and friends for their love and continued support.

ACKNOWLEDGEMENTS

First of all, I would like to thank my Ph.D. thesis advisors Dr. Sven H. Behrens and Dr. J. Carson Meredith for their continued support and guidance over the past few years. They not only gave me valuable academic advice, but also showcased their excellent soft skills and great personalities, which will benefit my whole life. I would also like to thank my Ph.D. thesis committee members: Dr. Yulin Deng, Dr. Christopher Luettgen and Dr. Justin Burton. They spent a lot of time and efforts with my Ph.D. Thesis Proposal, Pre-Doctoral Review and Ph.D. Thesis Defense. I really appreciate their support!

I could not have today's accomplishments without the support from my group members. They are Joohyung Lee, Abiola Shitta, Yi Zhang, Joanna Tsao, Xiaotang (Tony) Du, Maritza Mujica, Scott Essenmacher, Omotola Okesanjo, and Yali Li from Dr. Sven H. Behrens's research group; Oluwatimilehin Fadiran, Natalie Girouard, Haisheng Lin, Zifu Li, Yi Zhang, Zihao Qu, Chinmay Satam, Scott Essenmacher, Omotola Okesanjo and Ezgi Dogan-Guner from Dr. J. Carson Meredith's research group. They helped me make through the challenges and frustrating occasions on the way of doing research. There are also two undergraduate researchers Mikello Bonus and Xue Zong who helped me a lot with the experiments. They both did an excellent job and wish all the best to them in the future.

I feel very lucky that I have been accompanied by many good friends over the years. I have to admit that it was a bit difficult for me to leave my hometown and come alone to a different country to pursue knowledge. Fortunately, my friends were always on my side and helped me overcome the dark times.

I also would like to express my deepest thanks to my dear families: my parents and my sister! Although separated in two different continents, their love is always my strongest power to succeed. I could not make it without their continued support and encouragement.

Finally, the work in this thesis was made possible with the financial support from the Renewable Bioproduct Institute (RBI), Georgia Institute of Technology, and from the National Science Foundation (CBET-1706475). We would also like to acknowledge the generous donation of silica particles from Wacker-Chemie (Germany).

TABLE OF CONTENTS

LIST OF TABLES

LIST OF FIGURES

LIST OF SYMBOLS AND ABBREVIATIONS

E_{col}	Particle collection efficiency
E_c	Particle-bubble collision efficiency
E_a	Particle attachment efficiency
E_s	Particle stability efficiency
U	Particle-interface interaction energy
H	Hamaker constant
r	Particle radius
h	Separation distance or depletion depth
ε	Dielectric permittivity
ν	Frequency
n	Refractive index
k_B	Boltzmann constant
T	Temperature
z	Ion valence
e	Elementary charge
κ^{-1}	Debye length
ψ	Surface potential
q	Particle charge
ΔG_{ad}	Free energy change of particle adsorption
γ	Interfacial tension
θ	Contact angle

Γ	Surface concentration
c_0	Particle concentration
t	Time
D	Diffusion coefficient or equivalent-volume spherical bubble diameter
R	Particle radius or gas constant
ΔE_b	Particle adsorption energy barrier
N_A	Avogadro's number
ΔE	Energy benefit for a single particle to adsorb at the interface
α	Desorption constant
β	Adsorption constant
K	Interaction parameter in the Frumkin model
b	Bubble radius or droplet radius
τ	Kinetic time scale or diffusion time scale
p	Pressure
ρ	Density
μ	Viscosity
g	Gravity acceleration
δ	Dirac delta function
κ	Interfacial curvature
c	Volume fraction
S_o	Spreading coefficient
V	Bubble volume
d	Orifice diameter
Bo	Bond number (or Eötvös number)

V_T	Bubble terminal velocity
F	Particle-interface interaction force
CFD	Computational fluid dynamics
DLS	Dynamic light scattering
DLVO	Derjaguin, Landau, Vervey, and Overbeek
EDL	Electric double layer
ERIC	Effective residual ink concentration
HDDA	1,6-Hexanediol diacrylate
INGEDE	International association of the deinking industry
OTS	Octadecyltrichlorosilane
PVC	Polyvinyl chloride
TMPTMA	Trimethylolpropane trimethacrylate
VOF	Volume-of-fluid

SUMMARY

Froth flotation is an efficient method to selectively separate particulate species from aqueous dispersions or slurries. It has been widely utilized in many industries, such as mineral operation, oil recovery, waste paper recycling and waste water treatment, to name but a few. It relies on the principle that hydrophobic particles can attach to gas bubbles while hydrophilic ones cannot. For instance, in the flotation de-inking process, it can remove hydrophobic ink particles (such as offset inks and flexographic inks) but retain hydrophilic paper fibers.

However, froth flotation has fundamental limitations that make it unsuitable for current separation challenges in the paper recycling process, as well as in other application areas. In order to be separated from aqueous dispersions or slurries by gas flotation, the particles need to be either naturally hydrophobic or need to be rendered as hydrophobic by surface treatments. Some reagents, called collectors, can selectively adsorb onto the particle surface and tune the hydrophobicity of the particles. However, this may sometimes cause undesired synergistic interactions among collectors, activators, depressants and dispersants in the slurry. The use of collectors also tends to decrease the separation selectivity and increase costs. An alternative approach is not to tune the hydrophobicity of the particles, but to tune the hydrophobicity of the bubbles. This can be achieved by coating the bubbles with a thin film of oil, making its surface less hydrophobic than uncoated air bubbles, which is usually referred to as oily-bubble flotation in the literature. In recent years, there have been some studies on the application of oil-coated bubble flotation in mining operation and bitumen recovery, but the underlying mechanism is not fully

understood yet. To the best of our knowledge, there has not yet been a systematic comparison of oil-coated bubble flotation and uncoated bubble flotation.

In this study, we have systematically examined the fundamental aspects of oil-coated bubble flotation and compared it with the conventional uncoated bubble flotation. Oil-coated bubble flotation exhibits advantages over the traditional method from the following perspectives: 1) thermodynamics: for some hydrophilic particles, the adsorption energy benefit is higher at the oil-water interface compared with air-water interface, indicating stronger particle adsorption at the bubble surface; 2) kinetics: the particle adsorption barrier is lower at the oil-water interface compared with air-water interface, therefore particles adsorb to the oil-water interface more readily; 3) hydrodynamics: oil-coated bubbles rising in water display lower rising velocity, reduced magnitude of lateral excursions and more spherical shape compared with uncoated bubbles. These hydrodynamic differences can be beneficial to the flotation process. For example, lower rising velocity means the bubbles can stay longer in the slurry, therefore having more opportunities to interact with the particles.

After obtaining a better fundamental understanding of oil-coated bubble flotation, we aim at evaluating its performance in separating some less hydrophobic or even mildly hydrophilic particles, which are usually difficult to separate with the current technology. Inspired by our previous studies on capillary foams, we first developed a simple and convenient assay: a foaming test to evaluate the ability of particles to be collected and separated by gas bubbles (referred to as “particle floatability” in the remaining thesis). Particles that can create a significant amount of capillary foam display high affinity to the

oil-water interface, and are therefore more likely to be separated using oil-coated bubble flotation.

Finally, we focused on an industrially-relevant separation system to examine the performance of oil-coated bubble flotation. Flotation de-inking provides an interesting application area because the most modern types of ink particles are hydrophilic and therefore difficult to separate with current technology, but potentially amenable to oil-coated bubble flotation. Recycled paper pulps are also a convenient system to investigate, because the absorbance of ink particles at UV-vis wavelength range allows for quantitative evaluation of the flotation performance. In this study, flotation de-inking using both uncoated and oil-coated bubbles was performed with miniaturized and larger-scale tests. System parameters including oil type, salt type, salt concentration and pH were systematically evaluated. We found that oil-coated bubble flotation often dramatically outperforms the standard technique with uncoated bubbles; the highest ink removal efficiency was observed in systems containing multivalent salts at low pH when using bubbles coated with 1-octanol. This work sheds light on the mechanism of oil-coated bubble flotation in the separation of less hydrophobic or even mildly hydrophilic particles, and is expected to trigger broader interests in many other separation systems.

CHAPTER 1. INTRODUCTION

1.1 Froth Flotation

The selective separation of particulates from aqueous dispersions or slurries is crucial to many industrial processes, including mineral separation,[1-3] bitumen recovery,[4-6] deinking processing[7-9] and waste water treatment,[10-12] only to name but a few. Froth flotation, which relies on the selective adsorption of small particles to rising gas bubbles (or the attachment of small gas bubbles to larger solids in some cases) and their joint rise into a readily separable froth, has been one of the enabling technologies of the past century and is still one of the most widespread large-scale separation techniques.[13]

1.1.1 Mechanism

As shown in Figure 1-1, the basic principle of froth flotation is that hydrophobic particles will attach to rising gas bubbles and will be lifted to the surface, whereas more hydrophilic components will remain in the slurry. A slightly different scenario is when separating larger solids, gas bubbles will preferentially attach to the surface of hydrophobic solids, and the complex will jointly float to the top due to increased buoyant force. In this study, we are more interested in separating some small particles (less than 10 μm) to address some industrially-related separation challenges such as de-inking, therefore we will only focus on the former scenario.

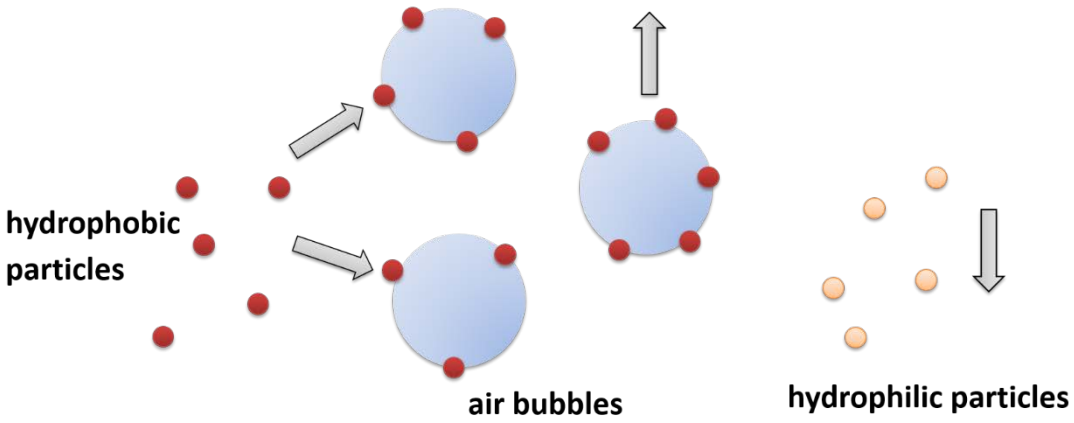

Figure 1-1 Mechanism of conventional froth flotation.

In order for the particles to be collected and removed by the rising gas bubbles, the following three sub-processes are necessary: the collision between particles and bubbles, the attachment of particles onto bubble surfaces, and particles staying stable on bubble surfaces until being lifted to the froth layer and being removed. Derjaguin and Dukhin [14] defined the overall particle collection efficiency, E_{col}, in terms of the efficiency of above three independent sub-processes, namely the particle-bubble collision efficiency, E_c, particle attachment efficiency, E_a, and particle stability efficiency E_s:

$$E_{col} = E_c \times E_a \times E_s . \tag{1-1}$$

To achieve a high particle collection efficiency, each of the sub-processes need to be optimized. The particle-bubble collision is mainly influenced by the hydrodynamics of bubble motion; the particle-bubble attachment is mainly influenced by the interactions between the particle and bubble; the stability of particles on bubble surfaces is influenced

by both the particle-bubble interaction and the bubble motion.[13, 15-16] Therefore, the following discussion will focus on these two important perspectives: particle-bubble interaction and bubble rise dynamics.

1.1.1.1 Particle-Bubble Attachment: Interaction Force and Energy

For the conventional froth flotation, the interaction between the particle and the bubble surface (air-water interface) can be calculated based on the extended DLVO (Derjaguin, Landau, Vervey, and Overbeek) theory. The particle-bubble interaction results from the joint contributions of van der Waals, electric double layer, and image force interactions.

The van der Waals interaction between a spherical particle and a flat air-water interface is given by Equation 1-2:[17]

$$U_{vdw} = -H_{awp}\frac{r}{6h}, \tag{1-2}$$

where H_{awp} is the nonretarded Hamaker constant obtained by the mixing rule

$$H_{awp} = (\sqrt{H_{aa}} - \sqrt{H_{ww}})(\sqrt{H_{pp}} - \sqrt{H_{ww}}), \tag{1-3}$$

and where r is the particle radius and h is the separation distance. H_{aa}, H_{ww} and H_{pp} are the Hamaker constants from the exact Lifshiftz theory results for the symmetric interaction of air, water, and solid particle across a vacuum.[18]

The electrostatic double layer (EDL) energy of interaction between the particle and the interface was calculated as[18]

$$U_{EDL} = 64\pi\varepsilon_0\varepsilon_r r(\frac{k_B T}{ze})^2 \tanh(\frac{ze\psi_p}{4k_B T}) \tanh(\frac{ze\psi_a}{4k_B T}) \exp(-\kappa h) \quad (1\text{-}4)$$

where ε_0 is the dielectric permittivity of the vacuum, ε_r is the relative dielectric constant of water, k_B is Boltzmann constant, T is temperature, z is the ion valence of the electrolyte solution, e is the elementary charge, κ^{-1} is the Debye length , ψ_p is the surface potential of particle, and ψ_a is the surface potential of air-water interface. Equation 1-4 is based on a linear superposition of the Gouy-Chapman solutions for the electrostatic potential near flat charged surfaces and implements the Derjaguin approximation to account for the particle curvature, against which the curvature of the fluid-fluid interface is neglected.

It is well-known that a charged particle near an interface with discontinuity of dielectric permittivity experiences a force pointing towards the more polarizable medium, which is called the image force interaction (as if the interaction resulted from an "image charge" positioned across the interface).[18] The magnitude of the "image charge" is given by

$$q_{image} = q\frac{\varepsilon_1 - \varepsilon_2}{\varepsilon_1 + \varepsilon_2}, \quad (1\text{-}5)$$

where ε_1 is the dielectric constant of the medium where the particle is located, and ε_2 is the dielectric constant of the particle-free medium. The interaction between two spherical particles is given by[18]

$$U_{image} = 32\pi\varepsilon_0\varepsilon_r r(\frac{k_B T}{ze})^2 \tanh(\frac{ze\psi_p}{4k_B T}) \tanh(\frac{ze\psi_i}{4k_B T}) \exp(-2\kappa h), \quad (1\text{-}6)$$

where ψ_i is the surface potential of the image charge, is given by Equation 1-7:[18]

$$\psi_i = \frac{2k_B T}{e} \sinh^{-1}[\frac{\varepsilon_w - \varepsilon_a}{\varepsilon_w + \varepsilon_a} \sinh(\frac{e\psi_p}{2k_B T})], \quad (1\text{-}7)$$

where ε_w is the dielectric constant of water and ε_a is the dielectric constant of air.

In most cases, the overall repulsion force outweighs the attraction force, leading to an adsorption energy barrier. Only particles with sufficient energy can overcome this energy barrier and come in contact with the interface. In the next chapter, the difference between the particle adsorption at the air-water interface (uncoated bubble surface) and the oil-water interface (oil-coated bubble surface) will be compared, showing the lower adsorption energy barrier at the oil-water interface and the resulting kinetic benefit of oil-coated bubble flotation.

1.1.1.2 Particle-Bubble Attachment: Induction Time

Particles collided with the gas bubbles do not necessarily get attached immediately, even the particle wetting at the interface is thermodynamically beneficial. It requires some

time (known as “induction time”) for the intervening liquid film between the particle and bubble to thin and rupture, and for a stable three-phase contact line to form.[19-20] Ye and Miller[19] measured the induction time for coal particles of different surface hydrophobicities, and found it ranged from less than 1 ms to 100 ms. Hewitt et al.[21] found that the thinning rate of the intervening liquid film on some hydrophobic quartz plates increased with increasing electrolyte concentration. Recently, Gu et al. [22] investigated the induction time between silica particle and air bubbles. They found that the induction time decreases with increasing temperature, and it was shortest in deionized water but longest in process water containing 50 ppm calcium ions. Wang et al. [23] developed a model to describe the induction time of an air bubble in contact with a methylated silica bead, based on an analytical solution of Reynolds approximation under the specific boundary conditions. It was found that the induction time increased with increasing bubble size.

Considering the relatively narrow range that induction time varies (compared to the more significant change of bubble residence time in the slurry by coating the bubbles with a thin layer of oil, which will be presented in Chapter Three) and limited impact on flotation performance, it will not be the focus of this thesis. However, future studies will still be meaningful to confirm whether the induction time exhibits remarkable difference between uncoated and oil-coated gas bubbles and the resulting influence on particle adsorption in froth flotation.

1.1.1.3 Bubble Rise Dynamics

Since flotation performance is closely related to the dynamic rise behavior of air bubbles, it is of great interest to understand and predict bubble rise dynamics. The motion of uncoated bubbles has already been studied extensively by several researchers (see *e.g.*, ref. [24-28]). The shape deformation, breakup, and path instability have been investigated thoroughly. Recently, we have successfully used the volume-of-fluid (VOF) method with dynamic adaptive grid refinement to simulate the rise dynamics of an initially spherical air bubble rising from a quiescent liquid,[29] and then applied the model to predict dynamics under several different flow conditions.[30-32] Tripathi et al.[29] have also identified five different regimes of starkly distinct behaviors (namely: axisymmetric, skirted, zigzagging/spiraling, peripheral break-up and central breakup regions of an air bubble rising in water).

1.1.2 Limitation and Remedies

Based on the discussion of the separation mechanism, one of the most serious limitations of conventional froth flotation is that water-dispersible particles can be simply too hydrophilic to adhere strongly to gas bubbles.[33] For effective particle removal from aqueous dispersions or slurries by gas flotation, the particles need to be naturally hydrophobic, which is not always the case.

A straightforward approach to this problem is to render the hydrophobicity of the particles, therefore enhancing particle-bubble attachment. Some reagents, called collectors, can selectively adsorb onto the particle surface and tune the hydrophobicity of the particles.[34-35] As early as 1920s, Taggart pointed out that oils added to the system can enhance the performance of phosphate and coal flotation.[36] Many other chemicals

including fatty acids and surfactants have also been used as collectors, but they often cause undesired synergistic interactions among collectors, activators, depressants and dispersants in the slurry.[13] The use of collectors also tends to decrease the separation selectivity and increases costs.[13, 37]

Inspired by the use of oil as collectors in flotation, an alternative method has been developed: using oils to tune the surface properties of gas bubbles, not particles. By coating the gas bubble with a thin film of oil, the bubble surface can be adjusted less hydrophobic (compared to uncoated bubbles) to allow more efficient adsorption of less hydrophobic or even mildly hydrophilic particles (as shown in Figure 1-2). This idea of oil-coated bubbles has been applied in many areas in recent years. Liu et al.[37] covered air bubbles with a thin layer of kerosene, and investigated the attachment of coated-bubbles on silica, sphalerite and galena surfaces, and established the concept of reactive oily-bubble flotation. Zhou and his co workers[38-39] demonstrated the application of reactive oily bubbles in bastnaesite flotation. Wallwork et al.[40] and Su et al.[41] applied reactive oily bubbles to bitumen recovery. Chen et al.[42] and Tarkan et al.[43-45] developed a novel process, compressed air-assisted solvent extraction, to generate micro-sized solvent-coated air bubbles for metal extraction and bitumen recovery. Recently, Chen et al.[46] explored the interaction energy between long-flame coal particles and diesel oily bubbles and improved the flotation process.

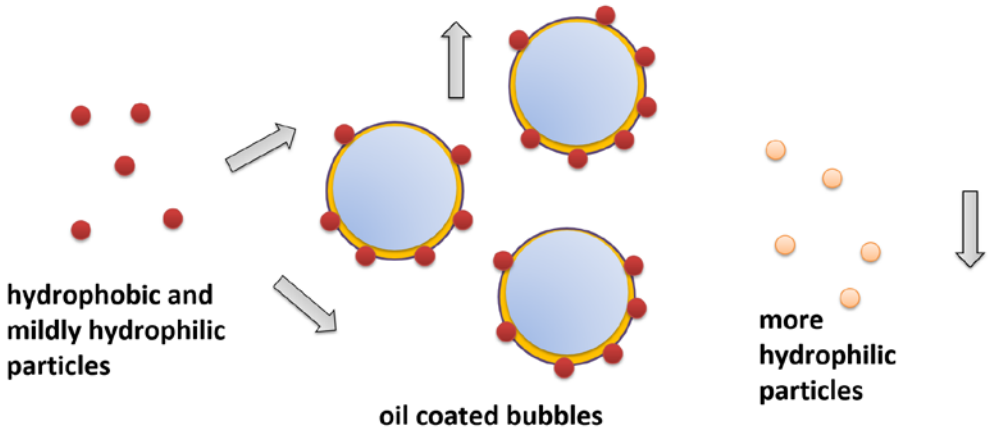

Figure 1-2 Mechanism of oil-coated bubble flotation.

1.2 Paper Recycling Process and Flotation De-Inking

The paper recycling process has gained growing attention over recent decades. Some of the reasons include the shortage of virgin wood fibers and the government restrictions on solid wastepaper landfilling. According to the American Forest & Paper Association, the amount of recycled paper keeps increasing each year and more than 60% of the paper products in the US are now being recycled.[47]

Waste paper products of different grades such as mixed office waste (MOW), old corrugated containers (OCC), old newspaper (ONP) and old magazine (OMG) are being collected and sent to the paper recycling mills. The quality of recycled fibers cannot compete with the virgin fibers, therefore a series of physical and chemical treatments are required in order to reuse these recycled fibers. The typical processes include pulping, screening, cleaning and de-inking, along with combinations of kneading, soaking, and washing.

Flotation de-inking is one of the most essential operations in the paper recycling industry to remove ink particles from the pulp slurry. The basic principle is that hydrophobic ink particles can attach to the hydrophobic air bubble surface and be lifted to the top where they can form a readily removable froth layer, while those hydrophilic paper fibers cannot attach and remain in the slurry.

There are several important steps involved during pulping and de-inking: [48]

- Ink particles detach from fibers;
- Ink particles collide with gas bubbles;
- The collision must provide sufficient energy to overcome the repulsive forces between the particles and the bubbles in order to form a stable complex;
- The air bubble must carry ink particles to the top;
- The air bubble/ink particle complex must be removed and cannot be recycled back into the slurry.

Our study focuses on the second through the fourth steps - the interactions between ink particles and bubbles and the rise of gas bubbles. The detachment of ink particles from fibers is a very complicated research topic on its own and it is beyond the scope of this thesis.

The traditional ink particles such as offset ink particles and flexographic ink particles are typically hydrophobic, and have a higher affinity for the gas bubbles, therefore can be collected and removed efficiently. However, due to changes in printing methods, waterborne inkjet inks containing hydrophilic ink particles have been used more widely in recent years. It is generally believed that this kind of waterborne ink is more environmentally benign, but it has actually led to an issue in the paper recycling industry: they cannot be efficiently removed by the conventional flotation de-inking due to lower affinity to the gas bubbles.[49-50]

To solve this problem, people first tried to use some regents (called “collectors”) to make the ink particle more hydrophobic. However, these chemicals often cause undesired synergistic interactions among collectors, activators, depressants and dispersants in the slurry.[13] The use of collectors also tends to decrease the separation selectivity and increases costs.[13, 37] As an alternative, people have also been exploring some other methods such as adsorption de-inking[51] and enzymatic de-inking[52-53], but it has not been completely confirmed whether these methods can remove hydrophilic ink particles efficiently and economically.

1.3 Capillary Foam

Foams are concentrated dispersions of gas bubbles in a continuous liquid phase. They are ubiquitous in our daily lives as well as in many industrial processes, such as food and beverages,[54-55] cosmetic products,[56] ceramic foam catalysts,[57] polyurethane foam products,[58] the oil recovery process[59-60] and in wastewater treatment,[61] to name but a few. Two of the most important foam properties are stability and foamability. Foam stability describes the long-term existence of foam without bubble bursting, and can be quantified by the time taken by the foam to decay to half the original height after the gas flow or frothing is stopped.[62-64] Foamability, on the other hand, is the foam-generating capability at the initial stage of foaming, which we will characterize, as is most commonly done, through the initial foam volume generated from a certain volume of liquid by a given frothing procedure,[65-69] and point out that an alternative definition in terms of the time taken to form a specific volume of foam has also been used occasionally.[70]

High foam stability is often desired,[60, 71] and traditional surfactants are still routinely used as stabilizers.[72-73] However, due to the low adsorption energy, surfactant molecules adsorb at the air-water interface loosely and desorb easily, therefore surfactant-stabilized foams typically last for only a few days at most.[74] In addition to these stability problems, some surfactants are not biodegradable and harm the environment.[75]

Particles are known to have a much larger adsorption energy benefit at the air-water interface compared with surfactants.[76] In recent decades, there have been many studies on particle-stabilized foams (Pickering foams), which can last much longer compared to surfactant-stabilized foams.[74, 76] However, the number of particle types suitable for aqueous Pickering foams are rather limited. This is because on one hand, these particles need to be sufficiently hydrophilic to be water-dispersible; on the other hand, they also need to be sufficiently hydrophobic to adsorb strongly at a gas-water interface.[77]

Recently, our group discovered a new type of aqueous foam (capillary foam, as shown in Figure 1-3), which has significantly expanded the domain of particle-stabilized foams.[78-80] We found that in the presence of a small amount of a secondary, immiscible fluid ("oil"), particles with a strong affinity to the oil-water interface (but not necessarily to the gas-water interface) can facilitate the spreading of an oil coat around gas bubbles[81] and stabilize these oil-coated bubbles against coalescence and ripening by covering the oil-water interface (Figure 1-4). Moreover, excess particles in the aqueous bulk can connect via oil bridges into a continuous gel network (familiar from capillary suspensions[82]), which entraps the (oil-and-particle) coated bubbles (Figure 1-3).

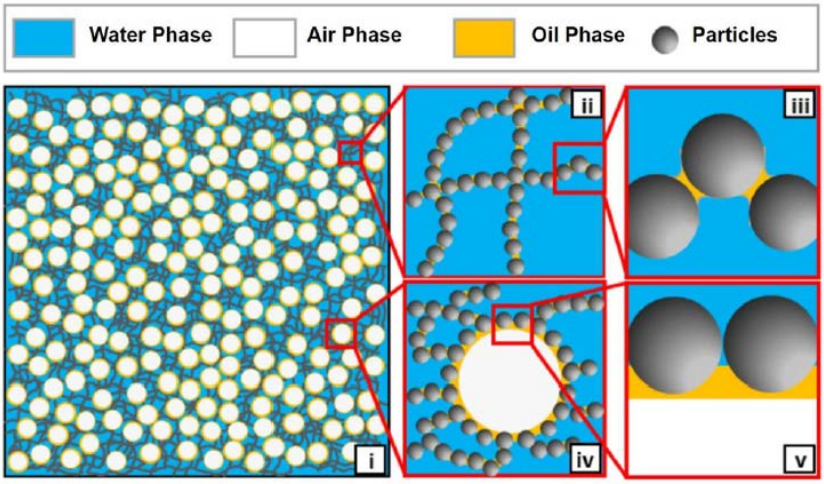

Figure 1-3 Structure of capillary foams.[80, 83] The system contains a continuous water phase, a gas phase, an oil phase, as well as particles. The agitation of the mixture results in a space-spanning network of particles in water (ii) connected by bridges of oil phase (iii), with air bubbles embedded in the network (iv) via a joint adsorption of particles and a thin oil film. Reproduced with permission from Ind. Eng. Chem. Res. 56, 34, 9533-9540. Copyright (2017) American Chemical Society.

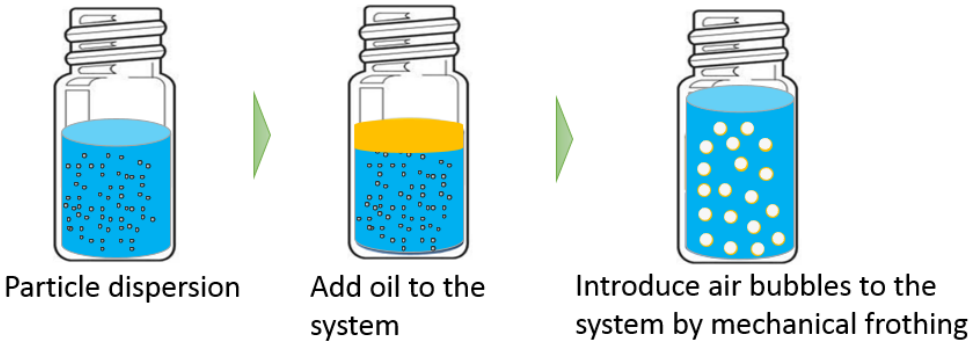

Figure 1-4 Procedure to make capillary foams.

This new type of aqueous foam displays excellent long-term stability and has many interesting applications, such as but not limited to colored foams, load-bearing porous materials, oil spill cleanup and enhanced oil recovery (as shown in Figure 1-5).[79]

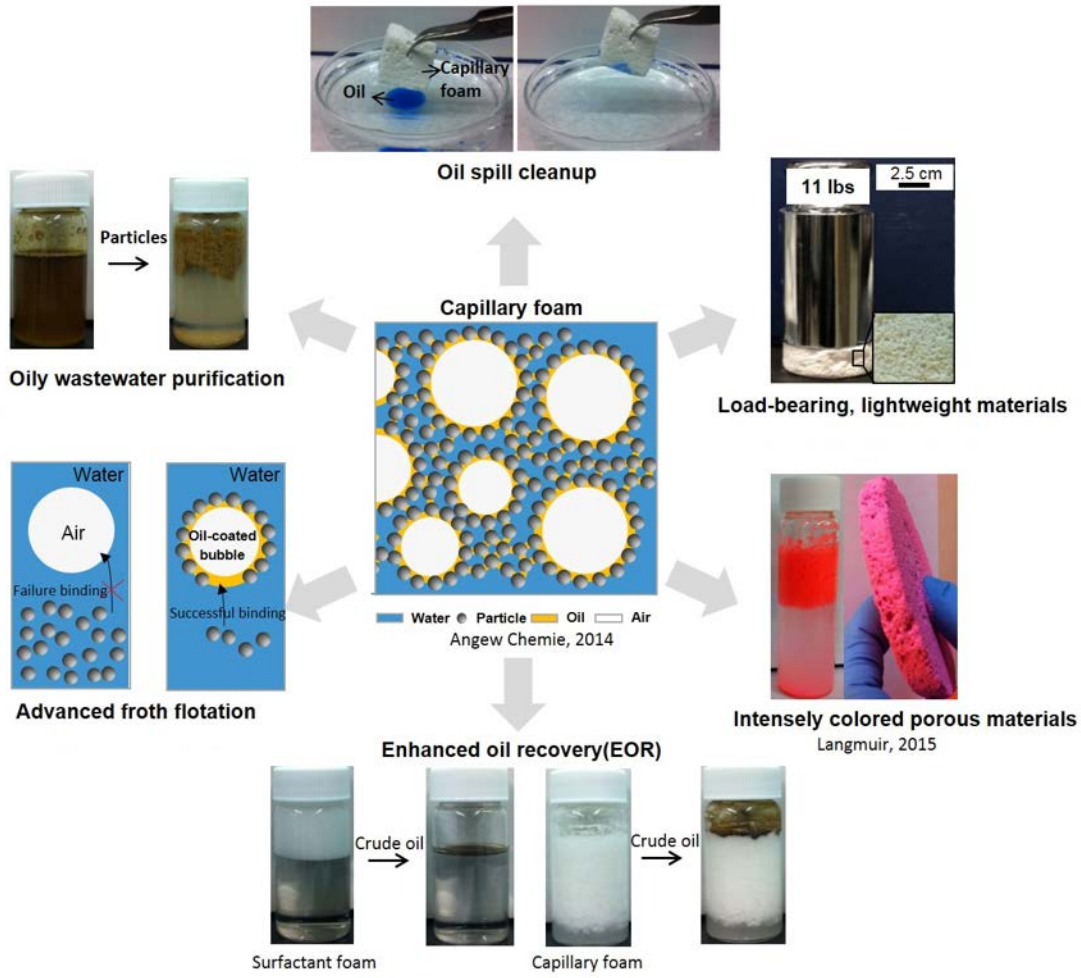

Figure 1-5 Some applications of capillary foams.[78-79]

Besides good long-term stability, good foamability is also desirable for many applications, such as personal care, food and beverages, firefighting, and many others.[84-

86]. Despite extensive research on the foam stability in recent years, there have been very few studies on the foamability of particle-stabilized foams. Binks et al[87] have shown that both pH and salt concentration have a significant impact on particle surface charge and subsequently on the formation of Pickering emulsions. Since the formation of capillary foam similarly relies on particle accumulation in the oil-water interface, it is pertinent to examine how and to what extent the foamability of capillary foams is influenced by particle surface charge. Recently, Lin et al.[88] prepared some interesting pH-responsive Pickering foams using silica nanoparticles in the presence of dodecyl dimethyl carboxyl betaine as stabilizer, and showed that the foamability is pH-dependent because the surfactant has different affinity for the particle surface under different pH, rendering the wettability of the particles. In the capillary foam system, there is no surfactant involved. It would be very interesting to investigate the foamability in terms of the impact of particles alone, without the confounded impact from surfactants.

In our previous studies, we have observed that several different types of particles cannot adsorb strongly at the air-water interface and create Pickering foams, but can adsorb strongly at the oil-water interface and create capillary foams.[78-80] Since the particle separation in froth flotation also relies on efficient particle adsorption at the fluid-fluid interface (air-water interface for conventional flotation, and oil-water interface for oil-coated bubble flotation), our hypothesis is that the foaming test – whether the particles can be used to create noticeable amount of foams can be used as a convenient method to evaluate the particle floatability (whether can be collected and removed by rising bubbles) in the flotation process.

1.4 Thesis Motivation and Objectives

The current froth flotation method is facing some challenges regarding separating some less hydrophobic or even mildly hydrophilic particulates, resulting from the lower affinity between the particulates and gas bubbles. Our study addresses this problem by adopting the oil-coated bubble flotation, and tries to better understand this complex colloidal system from both the fundamental and practical perspectives. The objectives of this study include:

(a) understand the thermodynamics, kinetics and hydrodynamics of oil-coated bubble flotation;

(b) develop a convenient method to evaluate the ability of particles to get collected and removed by rising gas bubbles (either coated or uncoated);

(c) apply oil-coated bubble flotation to some industrially-relevant separation systems as a proof-of-concept.

The structure of the thesis following the above objectives is presented in Figure 1-6.

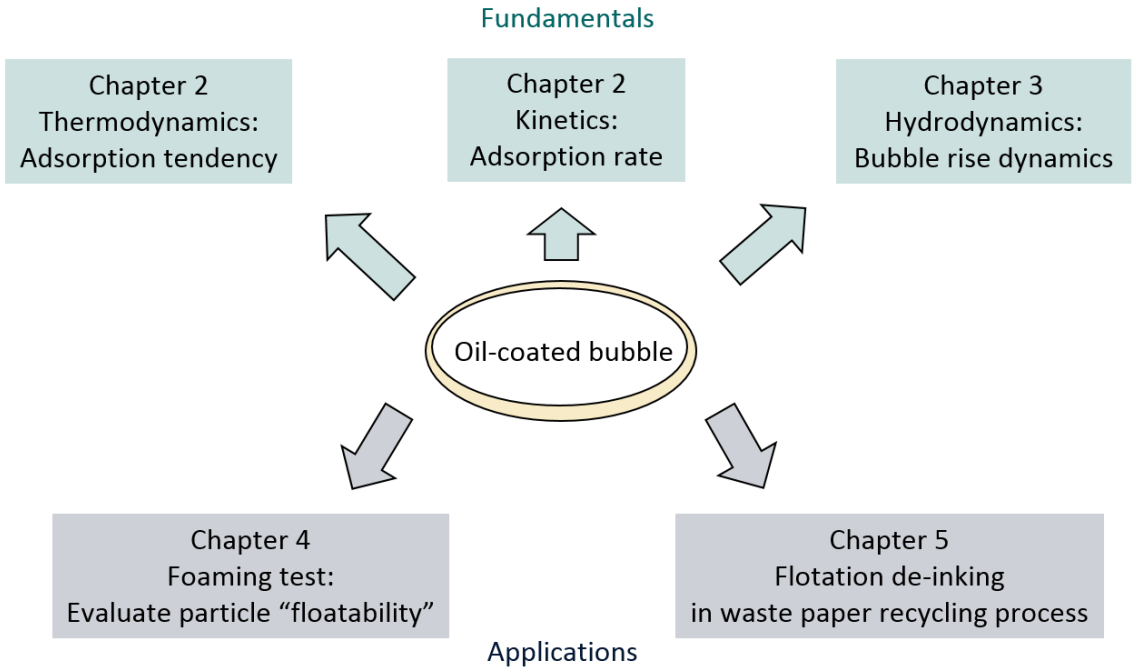

Figure 1-6 Structure of this thesis.

1.5 Thesis Outline

Chapter Two presents a review on the fundamentals of particle adsorption at the fluid-fluid interface, including the adsorption thermodynamics, adsorption kinetics and mass transfer. It points out the thermodynamic and kinetic advantages of oil-coated bubble flotation.

Chapter Three thoroughly investigates the rise dynamics of oil-coated bubbles in an aqueous media, which demonstrates the hydrodynamic benefit of oil-coated bubble flotation.

Chapter Four explores a complicated colloidal system – capillary foam, which is consisted of oil-coated bubbles as the basic units. It serves as a simple method to evaluate the floatability of particles (the ability to be collected and removed by rising gas bubbles) without the efforts to performing the experiments on large-scale equipment a priori.

Chapter Five focuses on the de-inking process in waste paper recycling industry and evaluates the feasibility of using oil-coated bubbles to remove the newer type of hydrophilic ink particles which are difficult to remove with the current technology.

Chapter Six summarizes the above chapters and offers some suggestions for future work on this research topic.

1.6 References

[1] Rodrigues, R. T.; Rubio, J. Daf-dissolved air flotation: Potential applications in the mining and mineral processing industry. *Int. J. Miner. Process.* **2007,** *82* (1), 1-13.

[2] Lee, K.; Archibald, D.; McLean, J.; Reuter, M. A. Flotation of mixed copper oxide and sulphide minerals with xanthate and hydroxamate collectors. *Miner. Eng.* **2009,** *22* (4), 395-401.

[3] Irannajad, M.; Ejtemaei, M.; Gharabaghi, M. The effect of reagents on selective flotation of smithsonite-calcite-quartz. *Miner. Eng.* **2009,** *22* (9-10), 766-771.

[4] Zhou, Z. A.; Li, H. H.; Chow, R.; Roberge, K. Role of carrier flotation in accelerating bitumen extraction recovery from mineable athabasca oil sands. *Can. J. Chem. Eng.* **2013,** *91* (8), 1340-1348.

[5] Al-Otoom, A.; Allawzi, M.; Al-Omari, N.; Al-Hsienat, E. Bitumen recovery from jordanian oil sand by froth flotation using petroleum cycles oil cuts. *Energy* **2010,** *35* (10), 4217-4225.

[6] Zhou, Z.; Kasongo, T.; Xu, Z.; Masliyah, J. Assessment of bitumen recovery from the athabasca oil sands using a laboratory denver flotation cell. *Can. J. Chem. Eng.* **2004,** *82* (4), 696-703.

[7] Gubitz, G. M.; Mansfield, S. D.; Bohm, D.; Saddler, J. N. Effect of endoglucanases and hemicellulases in magnetic and flotation deinking of xerographic and laser-printed papers. *J. Biotechnol.* **1998,** *65* (2-3), 209-215.

[8] Pesman, E.; Imamoglu, S.; Kalyoncu, E. E.; Kirci, H. The effects of sodium percarbonate and perborate usage on pulping and flotation deinking instead of hydrogen peroxide. *BioResources* **2014,** *9* (1), 523-536.

[9] Imamoglu, S.; Karademir, A.; Pesman, E.; Aydemir, C.; Atik, C. Effects of flotation deinking on the removal of main colors of oil-based inks from uncoated and coated office papers. *BioResources* **2013,** *8* (1), 45-58.

[10] Mahmoud, M. R.; Lazaridis, N. K.; Matis, K. A. Study of flotation conditions for cadmium(ii) removal from aqueous solutions. *Process Saf. Environ. Prot.* **2015,** *94*, 203-211.

[11] Fu, F. L.; Wang, Q. Removal of heavy metal ions from wastewaters: A review. *J. Environ. Manage.* **2011,** *92* (3), 407-418.

[12] Rubio, J.; Souza, M. L.; Smith, R. W. Overview of flotation as a wastewater treatment technique. *Miner. Eng.* **2002,** *15* (3), 139-155.

[13] Maurice C. Fuerstenau, G. J., Roe-Hoan Yoon. Froth flotation-a century of innovation. **2007**.

[14] Derjaguin, B. V.; Dukhin, S. S. Theory of flotation of small and medium-size particles. *Prog. Surf. Sci.* **1993,** *43* (1-4), 241-266.

[15] Nguyen, A. V.; Evans, G. M. Attachment interaction between air bubbles and particles in froth flotation. *Exp. Therm Fluid Sci.* **2004,** *28* (5), 381-385.

[16] Nguyen, A. V. Hydrodynamics of liquid flows around air bubbles in flotation: A review. *Int. J. Miner. Process.* **1999,** *56* (1-4), 165-205.

[17] Bhattacharjee, S.; Elimelech, M. Surface element integration: A novel technique for evaluation of dlvo interaction between a particle and a flat plate. *J. Colloid Interface Sci.* **1997,** *193* (2), 273-285.

[18] Israelachvili, J. Intermolecular and surface forces. Elsevier: Amsterdam, 2011.

[19] Ye, Y.; Khandrika, S. M.; Miller, J. D. Induction-time measurements at a particle bed. *Int. J. Miner. Process.* **1989,** *25* (3-4), 221-240.

[20] Yoon, R. H.; Yordan, J. L. Induction time measurements for the quartz-amine flotation system. *J. Colloid Interface Sci.* **1991,** *141* (2), 374-383.

[21] Hewitt, D.; Fornasiero, D.; Ralston, J.; Fisher, L. R. Aqueous film drainage at the quartz/water/air interface. *J. Chem. Soc. Faraday Trans.* **1993,** *89* (5), 817-822.

[22] Gu, G. X.; Xu, Z. H.; Nandakumar, K.; Masliyah, J. Effects of physical environment on induction time of air-bitumen attachment. *Int. J. Miner. Process.* **2003,** *69* (1-4), 235-250.

[23] Wang, W. X.; Zhou, Z.; Nandakumar, K.; Masliyah, J. H.; Xu, Z. G. An induction time model for the attachment of an air bubble to a hydrophobic sphere in aqueous solutions. *Int. J. Miner. Process.* **2005,** *75* (1-2), 69-82.

[24] Clift, R.; Grace, J. R.; Weber, M. E. *Bubbles, drops, and particles*; Dover: Mineola, NY, 2013.

[25] Sussman, M.; Puckett, E. G. A coupled level set and volume-of-fluid method for computing 3d and axisymmetric incompressible two-phase flows. *J. Comput. Phys.* **2000,** *162* (2), 301-337.

[26] Cano-Lozano, J. C.; Bohorquez, P.; Martínez-Bazán, C. Wake instability of a fixed axisymmetric bubble of realistic shape. *Int. J. Multiphase Flow* **2013,** *51*, 11-21.

[27] Cano-Lozano, J. C.; Martinez-Bazan, C.; Magnaudet, J.; Tchoufag, J. Paths and wakes of deformable nearly spheroidal rising bubbles close to the transition to path instability. *Phys. Rev. Fluids* **2016,** *1* (5).

[28] Zenit, R.; Magnaudet, J. Path instability of rising spheroidal air bubbles: A shape-controlled process. *Phys. Fluids* **2008,** *20* (6), 061702.

[29] Tripathi, M. K.; Sahu, K. C.; Govindarajan, R. Dynamics of an initially spherical bubble rising in quiescent liquid. *Nat. Commun.* **2015,** *6*, 6268.

[30] Sahu, K. C. Double-diffusive instability in core-annular pipe flow. *J. Fluid Mech.* **2016,** *789*, 830-855.

[31] Premlata, A. R.; Tripathi, M. K.; Sahu, K. C. Dynamics of rising bubble inside a viscosity-stratified medium. *Phys. Fluids* **2015,** *27* (7).

[32] Premlata, A. R.; Tripathi, M. K.; Karri, B.; Sahu, K. C. Dynamics of an air bubble rising in a non-newtonian liquid in the axisymmetric regime. *J. Nonnewton. Fluid. Mech.* **2017,** *239*, 53-61.

[33] Schwarz, S.; Grano, S. Effect of particle hydrophobicity on particle and water transport across a flotation froth. *Colloids Surf., A* **2005,** *256* (2-3), 157-164.

[34] Sis, H.; Chander, S. Reagents used in the flotation of phosphate ores: A critical review. *Miner. Eng.* **2003,** *16* (7), 577-585.

[35] Erol, M.; Colduroglu, C.; Aktas, Z. The effect of reagents and reagent mixtures on froth flotation of coal fines. *Int. J. Miner. Process.* **2003,** *71* (1-4), 131-145.

[36] Taggart. Handbook of ore dressing. **1927**.

[37] Liu, J.; Mak, T.; Zhou, Z.; Xu, Z. Fundamental study of reactive oily-bubble flotation. *Miner. Eng.* **2002,** *15* (9), 667-676.

[38] Zhou, F.; Wang, L.; Xu, Z.; Liu, Q.; Chi, R. Interaction of reactive oily bubble in flotation of bastnaesite. *J. Rare Earths* **2014,** *32* (8), 772-778.

[39] Zhou, F.; Wang, L.; Xu, Z.; Liu, Q.; Deng, M.; Chi, R. Application of reactive oily bubbles to bastnaesite flotation. *Miner. Eng.* **2014,** *64*, 139-145.

[40] Wallwork, V.; Xu, Z. H.; Masliyah, J. Bitumen recovery with oily air bubbles. *Can. J. Chem. Eng.* **2003,** *81* (5), 993-997.

[41] Su, L.; Xu, Z.; Masliyah, J. Role of oily bubbles in enhancing bitumen flotation. *Miner. Eng.* **2006,** *19* (6-8), 641-650.

[42] Chen, F.; Finch, J. A.; Distin, P. A.; Gomez, C. O. Air assisted solvent extraction. *Can. Metall. Q.* **2003,** *42* (3), 277-280.

[43] Tarkan, H. M.; Finch, J. A. Air-assisted solvent extraction: Towards a novel extraction process. *Miner. Eng.* **2005,** *18* (1), 83-88.

[44] Tarkan, H. M.; Finch, J. A. Foaming properties of solvents for use in air-assisted solvent extraction. *Colloids Surf., A* **2005,** *264* (1-3), 126-132.

[45] Tarkan, H. M.; Gelinas, S.; Finch, J. A. Measurement of thickness and composition of a solvent film on a bubble. *J. Colloid Interface Sci.* **2006,** *297* (2), 732-7.

[46] Chen, S., Tang, L., Tao, X., He, H., Yang, Z., Chen, L. Exploration on the mechanism of oily-bubble flotation of long-flame coal. *Fuel* **2018,** *216*, 427-435.

[47] Statistics of paper & paperboard recovery. Available at: http://www.paperrecycles.org/statistics/paper-paperboard-recovery.

[48] McKinney, R. W. J. Technology of paper recycling. 1994.

[49] Hsieh, J. S. Deinking of inkjet digital nonimpact printing. *Tappi J.* **2012,** *11* (9), 9-15.

[50] Mohandass, C.; Raghukumar, C. Biological deinking of inkjet-printed paper using vibrio alginolyticus and its enzymes. *J. Ind. Microbiol. Biotechnol.* **2005,** *32* (9), 424-429.

[51] Du, X. T.; Lee, D. T.; Hsieh, J. S. Inkjet ink behaviors and its implication in adsorption deinking. *Sep. Sci. Technol.* **2016,** *51* (18), 2857-2867.

[52] Pathak, P.; Bhardwaj, N. K.; Singh, A. K. Optimization of chemical and enzymatic deinking of photocopier waste paper. *BioResources* **2011,** *6* (1), 447-463.

[53] Ibarra, D.; Monte, M. C.; Blanco, A.; Martinez, A. T.; Martinez, M. J. Enzymatic deinking of secondary fibers: Cellulases/hemicellulases versus laccase-mediator system. *J. Ind. Microbiol. Biotechnol.* **2012,** *39* (1), 1-9.

[54] Green, A. J.; Littlejohn, K. A.; Hooley, P.; Cox, P. W. Formation and stability of food foams and aerated emulsions: Hydrophobins as novel functional ingredients. *Curr. Opin. Colloid Interface Sci.* **2013,** *18* (4), 292-301.

[55] Asghari, A. K.; Norton, I.; Mills, T.; Sadd, P.; Spyropoulos, F. Interfacial and foaming characterisation of mixed protein-starch particle systems for food-foam applications. *Food Hydrocoll.* **2016,** *53*, 311-319.

[56] Arzhavitina, A.; Steckel, H. Foams for pharmaceutical and cosmetic application. *Int. J. Pharm.* **2010,** *394* (1-2), 1-17.

[57] Twigg, M. V.; Richardson, J. T. Theory and applications of ceramic foam catalysts. *Chem. Eng. Res. Des.* **2002,** *80* (A2), 183-189.

[58] Giannitelli, S. M.; Basoli, F.; Mozetic, P.; Piva, P.; Bartuli, F. N.; Luciani, F.; Arcuri, C.; Trombetta, M.; Rainer, A.; Licoccia, S. Graded porous polyurethane foam: A potential scaffold for oro-maxillary bone regeneration. *Mater. Sci. Eng., C* **2015,** *51*, 329-335.

[59] Sun, Q.; Li, Z. M.; Li, S. Y.; Jiang, L.; Wang, J. Q.; Wang, P. Utilization of surfactant-stabilized foam for enhanced oil recovery by adding nanoparticles. *Energy & Fuels* **2014,** *28* (4), 2384-2394.

[60] Duan, X. G.; Hou, J. R.; Cheng, T. T.; Li, S.; Ma, Y. F. Evaluation of oil-tolerant foam for enhanced oil recovery: Laboratory study of a system of oil-tolerant foaming agents. *J. Pet. Sci. Eng.* **2014,** *122*, 428-438.

[61] Lu, K.; Zhang, X. L.; Zhao, Y. L.; Wu, Z. L. Removal of color from textile dyeing wastewater by foam separation. *J. Hazard. Mater.* **2010,** *182* (1-3), 928-932.

[62] Hunter, T. N.; Wanless, E. J.; Jameson, G. J.; Pugh, R. J. Non-ionic surfactant interactions with hydrophobic nanoparticles: Impact on foam stability. *Colloids Surf., A* **2009,** *347* (1-3), 81-89.

[63] Bhattacharyya, A.; Monroy, F.; Langevin, D.; Argillier, J. F. Surface rheology and foam stability of mixed surfactant-polyelectrolyte solutions. *Langmuir* **2000,** *16* (23), 8727-8732.

[64] Petkova, R.; Tcholakova, S.; Denkov, N. D. Foaming and foam ftability for mixed polymer-surfactant solutions: Effects of surfactant type and polymer charge. *Langmuir* **2012,** *28* (11), 4996-5009.

[65] Sett, S.; Sahu, R. P.; Pelot, D. D.; Yarin, A. L. Enhanced foamability of sodium dodecyl sulfate surfactant mixed with superspreader trisiloxane-(poly)ethoxylate. *Langmuir* **2014,** *30* (49), 14765-14775.

[66] Oh, S. G.; Shah, D. O. Relationship between micellar lifetime and foamability of sodium dodecyl sulfate and sodium dodecyl sulfate/1-hexanol mixtures. *Langmuir* **1991,** *7* (7), 1316-1318.

[67] Amaral, M. H.; das Neves, J.; Oliveira, A. Z.; Bahia, M. F. Foamability of detergent solutions prepared with different types of surfactants and waters. *J. Surfact. Deterg.* **2008,** *11* (4), 275-278.

[68] Marinova, K. G.; Basheva, E. S.; Nenova, B.; Temelska, M.; Mirarefi, A. Y.; Campbell, B.; Ivanov, I. B. Physico-chemical factors controlling the foamability and foam stability of milk proteins: Sodium caseinate and whey protein concentrates. *Food Hydrocoll.* **2009,** *23* (7), 1864-1876.

[69] Sakai, T.; Kaneko, Y. The effect of some foam boosters on the foamability and foam stability of anionic systems. *J. Surfact. Deterg.* **2004,** *7* (3), 291-295.

[70] Deng, Q. H.; Li, H. P.; Li, C. X.; Lv, W. Q.; Li, Y. Enhancement of foamability and foam stability induced by interactions between a hyperbranched exopolysaccharide and a zwitterionic surfactant dodecyl sulfobetaine. *Rsc Advances* **2015,** *5* (76), 61868-61875.

[71] Jing, J. Q.; Sun, J.; Zhang, M.; Wang, C. S.; Xiong, X. Q.; Hu, K. Preparation and rheological properties of a stable aqueous foam system. *Rsc Advances* **2017,** *7* (62), 39258-39269.

[72] Lv, Q. C.; Li, Z. M.; Li, B. F.; Li, S. Y.; Sun, Q. Study of nanoparticle-surfactant-stabilized foam as a fracturing fluid. *Ind. Eng. Chem. Res.* **2015,** *54* (38), 9468-9477.

[73] Sun, L.; Pu, W. F.; Xin, J.; Wei, P.; Wang, B.; Li, Y. B.; Yuan, C. D. High temperature and oil tolerance of surfactant foam/polymer-surfactant foam. *Rsc Advances* **2015,** *5* (30), 23410-23418.

[74] Binks, B. P.; Horozov, T. S. Aqueous foams stabilized solely by silica nanoparticles. *Angew. Chem. Int. Ed. Engl.* **2005,** *44* (24), 3722-3725.

[75] Scott, M. J.; Jones, M. N. The biodegradation of surfactants in the environment. *Biochim. Biophys. Acta* **2000,** *1508* (1-2), 235-251.

[76] Binks, B. P. Particles as surfactants - similarities and differences. *Curr. Opin. Colloid Interface Sci.* **2002,** *7* (1-2), 21-41.

[77] Gonzenbach, U. T.; Studart, A. R.; Tervoort, E.; Gauckler, L. J. Stabilization of foams with inorganic colloidal particles. *Langmuir* **2006,** *22* (26), 10983-10988.

[78] Zhang, Y.; Wu, J.; Wang, H.; Meredith, J. C.; Behrens, S. H. Stabilization of liquid foams through the synergistic action of particles and an immiscible liquid. *Angew. Chem. Int. Ed. Engl.* **2014,** *53* (49), 13603-13607.

[79] Zhang, Y.; Allen, M. C.; Zhao, R. Y.; Deheyn, D. D.; Behrens, S. H.; Meredith, J. C. Capillary foams: Stabilization and functionalization of porous liquids and solids. *Langmuir* **2015,** *31* (9), 2669-2676.

[80] Zhang, Y.; Wang, S. C.; Zhou, J. R.; Benz, G.; Tcheimou, S.; Zhao, R. Y.; Behrens, S. H.; Meredith, J. C. Capillary foams: Formation stages and effects of system parameters. *Ind. Eng. Chem. Res.* **2017,** *56* (34), 9533-9540.

[81] Zhang, Y.; Shitta, A.; Meredith, J. C.; Behrens, S. H. Bubble meets droplet: Particle-assisted reconfiguration of wetting morphologies in colloidal multiphase systems. *Small* **2016,** *12* (24), 3309-3319.

[82] Koos, E.; Willenbacher, N. Capillary forces in suspension rheology. *Science* **2011,** *331* (6019), 897-900.

[83] Zhang, Y. Particles as stabilizers and wetting modifiers in colloidal multiphase systems. Doctoral Thesis., Georgia Institute of Technology. 2016.

[84] Arnaudov, L.; Denkov, N. D.; Surcheva, I.; Durbut, P.; Broze, G.; Mehreteab, A. Effect of oily additives on foamability and foam stability. 1. Role of interfacial properties. *Langmuir* **2001,** *17* (22), 6999-7010.

[85] Zaggia, A.; Conte, L.; Padoan, G.; Bertani, R. Synthesis and application of perfluoroalkyl quaternary ammonium salts in protein-based fire-fighting foam concentrates. *J. Surfact. Deterg.* **2010,** *13* (1), 33-40.

[86] Nunes, F. M.; Coimbra, M. A.; Duarte, A. C.; Delgadillo, I. Foamability, foam stability, and chemical composition of espresso coffee as affected by the degree of roast. *J. Agric. Food. Chem.* **1997,** *45* (8), 3238-3243.

[87] Binks, B. P.; Murakami, R.; Armes, S. P.; Fujii, S. Effects of ph and salt concentration on oil-in-water emulsions stabilized solely by nanocomposite microgel particles. *Langmuir* **2006,** *22* (5), 2050-2057.

[88] Lin, Q.; Liu, K. H.; Cui, Z. G.; Pei, X. M.; Jiang, J. Z.; Song, B. L. Ph-responsive pickering foams stabilized by silica nanoparticles in combination with trace amount of dodecyl dimethyl carboxyl betaine. *Colloids Surf., A* **2018,** *544*, 44-52.

CHAPTER 2. FUNDAMENTALS OF PARTICLE ADSORPTION AT FLUID-FLUID INTERFACES

2.1 Introduction

Efficient particle adsorption at the fluid-fluid interface is one of the essential steps in the flotation process. The tendency and strength of particle adsorption (thermodynamics) and the rate of particle adsorption (kinetics and mass transfer) are two important perspectives to investigate, and will be discussed in this chapter.

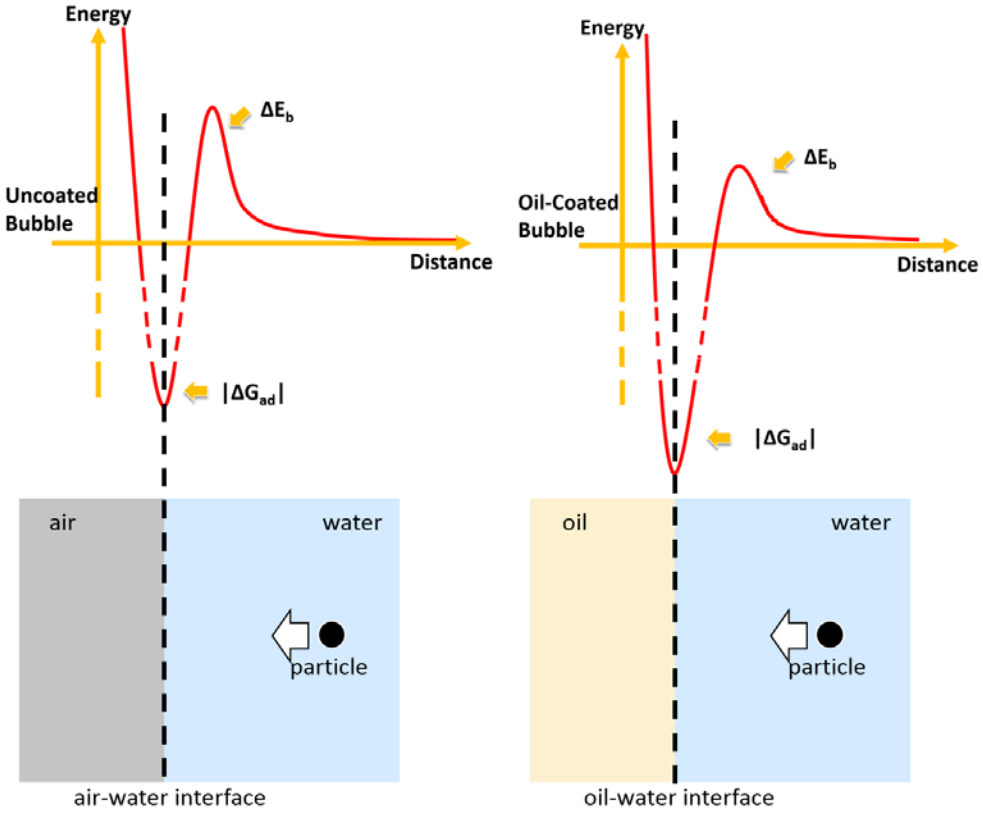

Figure 2-1 The energy profile of particle adsorption at air-water and oil-water interfaces.

Figure 2-1 shows the energy profile of particle adsorption at fluid-fluid interfaces: 1) Energy at infinite distance is set to zero as a reference; 2) Particles feel some repulsive force when they get closer to the interface, therefore only particles with sufficient energy (obtained through thermal fluctuations or mechanical energy input) can overcome the energy barrier and come in contact with the interface; 3) When a particle adsorbs at the interface, the total free energy decreases to some extent. The lower it becomes, the more strongly particles are held in the interface. As will be discussed in this chapter, the oil-water interface (*e.g.* of an oil-coated bubble) typically displays multiple benefits for particle adsorption over the air-water interface (uncoated bubble surface): a lower adsorption energy barrier as well as a larger free energy reduction.

2.2 Adsorption Thermodynamics[1]

2.2.1 Overview

The reduction in the interfacial energy upon adsorption of a single particle to the interface is given by:[1-2]

$$\Delta G_{ad,ij} = -\pi R^2 \gamma_{ij} \left(1 - \left|\cos\theta_{ijk}\right|\right)^2 \tag{2-1}$$

where γ_{ij} denotes the surface (or interfacial) tension of the clean interface, θ_{ikj} is the contact angle of a single particle at the interface (phase i in contact with phase k, measured through phase j), and R is the particle radius. The larger the free energy reduction upon

[1] Part of this section has been published in Industrial Engineering & Chemistry Research (Zhang Y., Wang S., et.al., Capillary foams: Formation stages and effects of system parameters. Ind. Eng. Chem. Res. 2017, 56, 9533-9540) and is reproduced with permission from American Chemical Society.

particle adsorption, the more strongly particles are held in the interface. For particles above a radius R of around 10 nm, this energy can easily exceed the thermal energy by orders of magnitude ($\left|\Delta G_{ad,ij}\right| >> k_B T$), making particle attachment to the interface practically irreversible; therefore neither thermal forces nor flow-induced forces during agitation are strong enough to remove adsorbed particles from the interface, which is desirable for particle separation by froth flotation.

The particle three-phase contact angle, θ, can be a useful (yet not always precise) indicator of the particle attachment strength at the interface and the particle's "affinity" for the bubble surface. Our previous studies[3] showed the difference in the adsorption of hydrophilic PVC (polyvinyl chloride) particles at an air-water interface (Figure 2-2 a) and an oil-water interface (Figure 2-2 b-d). The obviously low contact angle in Figure 2-2 a) suggests only a weak particle attachment to the air-water interface, whereas the contact angles near 90° in Figure 2-2 b-d) indicate stronger adsorption to the oil-water interfaces. These observations are consistent with the stability of aqueous foams stabilized by PVC particles: PVC particles cannot stabilize Pickering foams but can stabilize capillary foams.

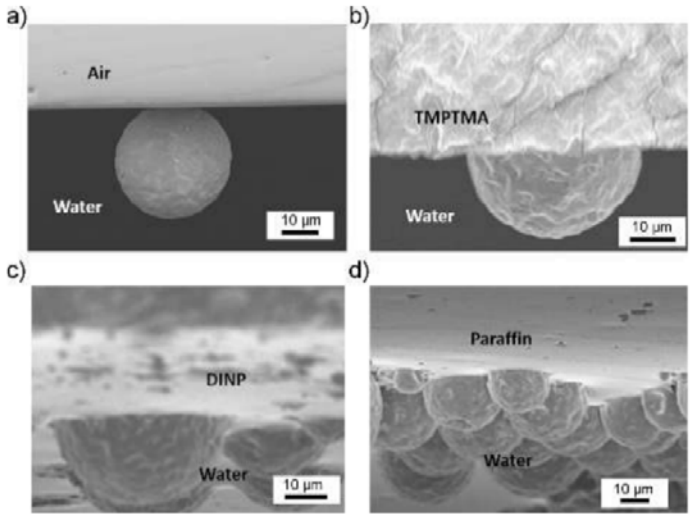

Figure 2-2 SEM images of PVC particles trapped in the PDMS replica of a macroscopic air-water interface (a) and of several oil-water interfaces (b-d) using the gel trapping technique. The visible part of the particle originally resided in the water phase. Figure reproduced from Angewandte Chemie (Zhang et al. "Stabilization of liquid foams through the synergistic action of particles and an immiscible liquid." Angewandte Chemie 126.49 (2014): 13603-13607.) with permission from Wiley.[3]

2.2.2 Experiments

Our hypothesis is that the free energy change of particle adsorption at the oil-water interface is more significant than that at the air-water interface, leading to stronger particle adsorption. To make a quantitative comparison, we need to know both the surface tension and the three-phase contact angle.

The air-water surface tension and oil-water interfacial tension were measured using a ramé-hart goniometer. Trimethylolpropane trimethacrylate (TMPTMA) purchased from Sigma-Aldrich was used as the oil phase, and was purified with a C-18 silica column before use.

The particle three-phase contact angle indicates the configuration of particles sitting at the interface. Fumed silica is used as the model particle, mainly because it allows convenient modification of the surface hydrophobicity. Wacker-Chemie AG (Germany) provided amorphous fumed silica particles with various degrees of hydrophobicity (modified by dichlorodimethylsilane): 100% SiOH (unmodified), 70% SiOH (30% methylsilyl capped), 50% SiOH (50% methylsilyl capped), and 32% SiOH (68% methylsilyl capped). Direct measurement of the particle contact angle, for example by the gel trapping method,[4] freeze-fracture shadow-casting cryo-scanning electron microscopy (FreSCa cryo-SEM),[5] or digital holography,[6] is challenging for fumed silica particles with a few hundred nanometers and non-spherical shapes. The wettability of these silica particles was therefore assessed in an approximate fashion by measuring the contact angle of an air bubble or an oil droplet in water against a pressed tablet of silica particles. The pressed substrate was immersed into a quartz cell filled with deionized water, and an air bubble or an oil droplet was then deposited with a 22 gauge needle. Images were obtained using the DROPimage software. The reported values are the angles measured through water (supplementary to the angles measured through the oil phase).

2.2.3 Results and Discussion

The measured air-water surface tension and TMPTMA-water interfacial tension are 72.0 mN/m and 19.0 mN/m, respectively. The particle three-phase contact angles at the air-water interface and TMPTMA-water interface are shown in Figure 2-3, Table 2-1 and Table 2-2. The ratio of the magnitude of energy reduction upon particle adsorption at TMPTMA-water interface versus at air-water interface (based on Equation 2-1) is shown in Table 2-3. It is interesting that the free energy reduction at both interfaces are of the

same order of magnitude. However, for the most hydrophilic silica particle, the free energy change upon adsorption at the TMPTMA-water interface is almost three times that for adsorption at the air-water interface, implying stronger particle attachment. In other words, this comparison shows that the oil-coated bubble flotation can be more efficient to separate these type of hydrophilic particles compared with uncoated bubble flotation. At the same time, it should be noted that this ratio can be dependent on the type of oil and type of particle, and the oil corresponding to the highest ratio should ideally be chosen for flotation purpose.

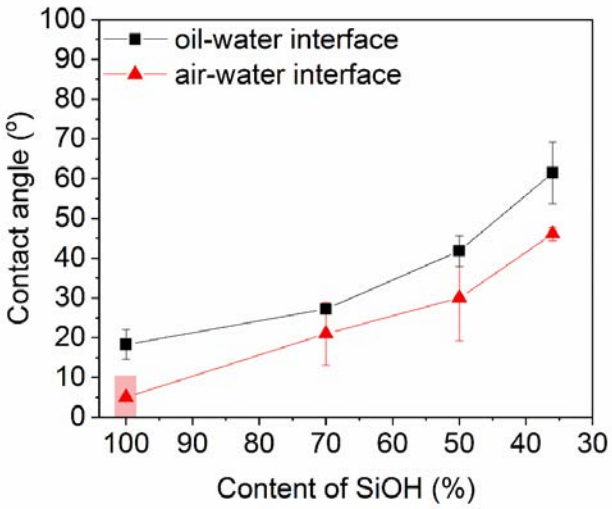

Figure 2-3 Contact angle measurement at air-water and oil-water interfaces by placing an air bubble or an oil droplet against silica particle pellet.[7] The uncertainty represents the standard deviation of at least three replicate measurements. Reproduced with permission from Industrial Engineering & Chemistry Research (Zhang Y., Wang S., et.al., Capillary foams: Formation stages and effects of system parameters. Ind. Eng. Chem. Res. 2017, 56, 9533-9540). Copyright (2017) American Chemical Society.

Table 2-1 Contact angle measurement at the air-water interface by placing an air bubble against silica particle pellet.[7] The uncertainty represents the standard

deviation of at least three replicate measurements. Reproduced with permission from Industrial Engineering & Chemistry Research (Zhang Y., Wang S., et.al., Capillary foams: Formation stages and effects of system parameters. Ind. Eng. Chem. Res. 2017, 56, 9533-9540). Copyright (2017) American Chemical Society.

Particle	Typical image	Contact angle (˚) at air-water interface
Silica (100% SiOH)	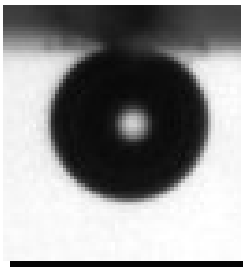	< 10*
Silica (70% SiOH)	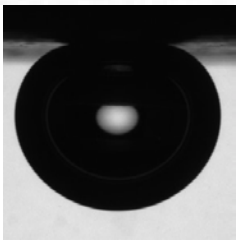	21 ± 8
Silica (50% SiOH)	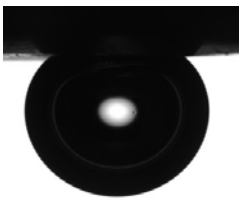	30 ± 10
Silica (36% SiOH)	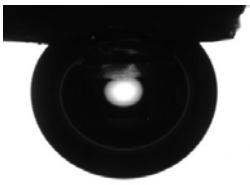	46 ± 2

*** The contact angle of the most hydrophilic (100% SiOH) silica surface with the air-water interface is difficult to measure because the air bubble rolls off the surface easily and the angle is too small for a precise determination.**

Table 2-2 Contact angle measurement at the TMPTMA-water interface by placing an oil droplet against silica particle pellet.[7] The uncertainty represents the standard

deviation of at least three replicate measurements. Reproduced with permission from Industrial Engineering & Chemistry Research (Zhang Y., Wang S., et.al., Capillary foams: Formation stages and effects of system parameters. Ind. Eng. Chem. Res. 2017, 56, 9533-9540). Copyright (2017) American Chemical Society.

Particle	Typical image	Contact angle (˚) at oil-water interface
Silica (100% SiOH)	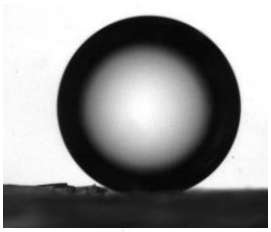	18 ± 4
Silica (70% SiOH)	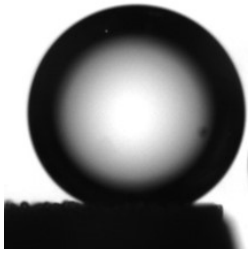	27 ± 0
Silica (50% SiOH)	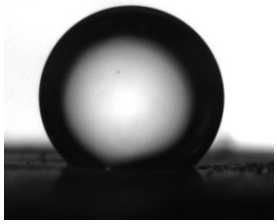	42 ± 4
Silica (36% SiOH)	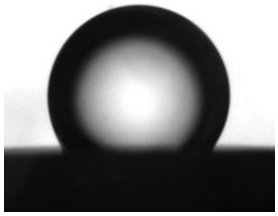	62 ± 8

Table 2-3 Ratio of the magnitude of energy reduction upon particle adsorption at the TMPTMA-water interface versus at the air-water interface.

Particle	Silica (100% SiOH)	Silica (70% SiOH)	Silica (50% SiOH)	Silica (36% SiOH)
Ratio	2.7	0.7	1.0	0.8

2.3 Adsorption Kinetics

2.3.1 Particle-Interface Interaction

As discussed in Chapter One, the interaction between the silica particle and the oil-water interface can be estimated based on the extended DLVO (Derjaguin, Landau, Vervey, and Overbeek) theory. The particle-interface interaction results from the joint contributions of van der Waals, electric double layer, and image force interactions. Next, let us compare each individual interaction at both the air-water interface and oil-water interface.

The van der Waals interaction between a spherical particle and a flat interface is given by Equation 2-2.[8]

$$U_{vdw} = -H_{Total}\frac{r}{6h} \tag{2-2}$$

where H_{Total} is the non-retarded Hamaker constant, r is the particle radius and h is the separation distance. The approximate expression for the non-retarded Hamaker constant for two macroscopic phases 1 and 2 interacting across a medium 3 based on the Lifshiftz theory is given by:[9]

$$H_{Total} = H_{\nu=0} + H_{\nu>0}$$

$$\approx \frac{3}{4} k_B T \left(\frac{\varepsilon_1 - \varepsilon_3}{\varepsilon_1 + \varepsilon_3} \right) \left(\frac{\varepsilon_2 - \varepsilon_3}{\varepsilon_2 + \varepsilon_3} \right)$$

$$+ \frac{3h\nu_e}{8\sqrt{2}} \frac{\left(n_1^2 - n_3^2 \right) \left(n_2^2 - n_3^2 \right)}{\left(n_1^2 + n_3^2 \right)^{1/2} \left(n_2^2 + n_3^2 \right)^{1/2} \left[\left(n_1^2 + n_3^2 \right)^{1/2} + \left(n_2^2 + n_3^2 \right)^{1/2} \right]} \qquad (2\text{-}3)$$

where $H_{\nu=0}$ is the zero-frequency contribution, $H_{\nu>0}$ is the higher-frequency dispersion energy contribution, ε is the static dielectric constant of each phase (typically, $2 < \varepsilon_p < 60$, $\varepsilon_o \approx 2$, $\varepsilon_a = 1$, $\varepsilon_w \approx 80$), n is the refractive index of each phase (typically, $1.4 < n_p < 1.6$, $1.35 < n_o < 1.43$, $n_a \approx 1$, $n_w \approx 1.33$), h is Planck constant, and ν_e is the main electronic absorption frequency in the UV range (typically around $3 \times 10^{15} s^{-1}$).

In the case of particle adsorption at an air-water interface, 1, 2 and 3 denote air, particle and water, respectively; while in the case of particle adsorption at an oil-water interface, 1, 2 and 3 denote oil, particle and water, respectively. In both scenarios, the zero-frequency contribution $H_{\nu=0}$ has the same sign (positive), and is of the same order of magnitude ($< \frac{3}{4} k_B T$), regardless of whether it is air-water interface or oil-water interface. However, for the dominating higher-frequency dispersion energy contribution $H_{\nu>0}$, it is negative at the air-water interface, but positive at the oil-water interface. Therefore, the

overall van der Waals force can be repulsive at the air-water interface, but attractive at the oil-water interface.

The electrostatic double layer (EDL) energy of interaction between the particle and the oil-water interface was calculated as [9]

$$U_{EDL} = 64\pi\varepsilon_0\varepsilon_r r(\frac{k_B T}{ze})^2 \tanh(\frac{ze\psi_p}{4k_B T}) \tanh(\frac{ze\psi_o}{4k_B T}) \exp(-\kappa h), \quad (2\text{-}4)$$

where ε_0 is the dielectric permittivity of the vacuum, ε_r is the relative dielectric constant of water, k_B is Boltzmann constant, T is temperature, z is the ion valence of the electrolyte solution, e is the elementary charge, κ^{-1} is the Debye length , ψ_p is the surface potential of particle, and ψ_o is the surface potential of oil-water interface. The calculation at the air-water interface shares the same formula, except that ψ_o is replaced by the surface potential of air-water interface, ψ_a. Rough estimation (ψ_o is estimated based on the electrophoresis data of pristine oil droplets,[10] and ψ_a is estimated based on the fits to experimental bubble-bubble forces measured by adapted atomic force microscopy[11-13]) reveals that the electrostatic double layer interaction is comparable for the air-water interface and oil-water interface.

It is well-known that a charged particle near an interface with discontinuity of dielectric permittivity experiences a force pointing towards the more polarizable medium.[9] The magnitude of the “image charge” is given by

$$q_{image} = q\frac{\varepsilon_1 - \varepsilon_2}{\varepsilon_1 + \varepsilon_2}, \tag{2-5}$$

where ε_1 is the dielectric constant of the medium where the particle is located, and ε_2 is the dielectric constant of the particle-free medium. The interaction between two spherical particles is given by[9]

$$U_{image} = 32\pi\varepsilon_0\varepsilon_r r(\frac{k_B T}{ze})^2 \tanh(\frac{ze\psi_p}{4k_B T}) \tanh(\frac{ze\psi_i}{4k_B T}) \exp(-2\kappa h), \tag{2-6}$$

where ψ_i is the surface potential of the image charge, is given by Equation 2-7.[9]

$$\psi_i = \frac{2k_B T}{e} \sinh^{-1}[\frac{\varepsilon_w - \varepsilon_o}{\varepsilon_w + \varepsilon_o} \sinh(\frac{e\psi_p}{2k_B T})] \tag{2-7}$$

where ε_w is the dielectric constant of water and ε_o is the dielectric constant of oil. The calculation at the air-water interface shares the same formula, except that ε_o is replaced by the dielectric constant of air, ε_a. Rough estimation also reveals that the image force interaction is comparable for the air-water interface and oil-water interface.

Based on the above discussion, the electric double layer and image force interactions at air-water interface and oil-water interface are comparable, while the van der Waals force interaction is repulsive at the air-water interface but attractive at the oil-water interface. It is then reasonably to argue that the particles should feel stronger repulsion from the air-water interface, and thus a higher particle adsorption energy barrier (as shown

in Figure 2-1). It is worth mentioning that the aforementioned equations are rather sensitive to the precision of each variable and parameter, and quantitative predictions of the resulting net interaction – typically the difference between two large terms for the attractive and repulsive contributions – are notoriously unreliable. Qualitative comparisons, however, can still provide valuable insights.

2.3.2 Adsorption Energy Barrier

As shown in Figure 2-1 and in the above discussion, there exists some energy barrier for the surfactants or particles to overcome and eventually adsorb onto the fluid-fluid interface. It is therefore interesting to understand, determine and adjust the height of this energy barrier, in order to achieve better particle adsorption performance.

Ward and Tordai[14] first established the solution to the surfactant adsorption process in terms of an unknown subsurface concentration $c_s(t)$:

$$\Gamma(t) = 2c_0\sqrt{\frac{Dt}{\pi}} - 2\sqrt{\frac{D}{\pi}}\int_0^{\sqrt{t}} c_s(t-\tau)d\tau^{1/2} \tag{2-8}$$

where t is time, c_0 is surfactant concentration in the bulk, D is diffusion coefficient, Γ is the surface concentration. The first term represents the diffusion of surfactants from the bulk to the interface, and the second term represents the so called “back diffusion”. Derivation with more details will be discussed later. This equation is valid not only for surfactants, but for particles as well.

The above equation only allows numerical solution for the general case, which is not very convenient. Fainerman et al[15] proposed an asymptotic analytical solution at $t \to 0$ (early stage) and $t \to \infty$ (late stage). The surface concentration can further be transformed to the surface tension through the Gibbs adsorption isotherm equation. The common formula of the surface tension at early stage and late stage as shown as follows, respectively: [15-16]

$$t \to 0: \qquad \gamma = \gamma_0 - 2RTc_0\sqrt{\frac{Dt}{\pi}} \tag{2-9}$$

$$t \to \infty: \qquad \gamma = \gamma_\infty + \frac{RT\Gamma_\infty^2}{c_0}\sqrt{\frac{\pi}{4Dt}} \tag{2-10}$$

where R is the gas constant, c_0 is bulk concentration, Γ_∞ is the steady-state surface concentration, D is diffusion coefficient, γ is surface tension, γ_0 is the initial surface tension of the clean interface, and γ_∞ is the steady-state surface tension.

In the presence of particle adsorption energy barrier, the particle diffusion coefficient becomes significantly smaller compared with the Stokes-Einstein diffusion coefficient, and they are correlated as follows:[17-18]

$$D_{eff} = D_{S-E}\exp(-\frac{2\Delta E_b}{k_B T}) \tag{2-11}$$

where D_{eff} is the effective or apparent diffusion coefficient, D_{S-E} is the intrinsic diffusion coefficient calculated using Stokes-Einstein equation, and ΔE_b is the particle adsorption energy barrier.

Bizmark et al.[16] adopted this method (Equation 2-9 and 2-10) when investigating the adsorption energy barrier of ethyl cellulose particles at the air-water interface. However, it was found that the calculated D_{S-E} based on the fitting of experimental results is larger than it should be from the value calculated from Stokes-Einstein equation. It was explained that for particle adsorption at the interface (especially large particles), the adsorption energy benefit is much larger compared to the adsorption energy benefit of surfactants, therefore Equation 2-9 needs to be adjusted otherwise it will lead to the overestimation of the diffusion coefficient. Bizmark et al.[16] presented a revised model for particle adsorption at the early age and determined the adsorption energy barrier of ethyl cellulose particles at the air-water interface.

$$t \to 0: \qquad \gamma = \gamma_0 - 2N_A \left|\Delta E\right| c_0 \sqrt{\frac{Dt}{\pi}} \tag{2-12}$$

where N_A is Avogadro's number and ΔE is the energy benefit for a single particle to adsorb at the interface. All the other symbols share the same meaning as above.

It is important to note that the aforementioned method to determine the adsorption energy barrier relies on the dynamic surface tension measurement using the pendant droplet (or bubble) method, which is based on the assumption that the particle mass transfer from the bulk phase to the fluid-fluid interface falls into the kinetic-limited region.

Unfortunately, this assumption is not valid in most cases, as shown by Alvarez et al.[19-20] The pendant droplet (or bubble) is so large that the overall mass transport process is actually limited by the diffusion process, not by the adsorption kinetics, which will be discussed in following sections in this chapter.

2.3.3 Adsorption Isotherms and Equation of State

For surfactants and small-size particles, both adsorption and desorption occur simultaneously at the fluid-fluid interface; for sub-micron and larger particles, however, since the adsorption energy benefit greatly exceeds the regular thermal fluctuation, the adsorption can be considered as irreversible, therefore desorption is negligible. Next, we will introduce two kinetics models and the corresponding adsorption isotherms and equation of state, which are useful when estimating the characteristic time scale of adsorption/desorption kinetics and solving the couples adsorption/desorption and diffusion system.

The simplest model to describe particle adsorption/desorption kinetics at the interface is the Langmuir model:[17, 21-22]

$$\frac{d\Gamma}{dt} = \beta c_s (1 - \frac{\Gamma}{\Gamma_\infty}) - \alpha\Gamma \tag{2-13}$$

where Γ is surface concentration, Γ_∞ is the equilibrium surface concentration, c_s is the concentration of surfactant or particle at the subsurface close to the interface, α is desorption constant (zero for irreversible adsorption) and β is the adsorption constant. By setting Equation 2-13 to be zero, we can get the Langmuir adsorption isotherm:

$$\frac{\Gamma}{\Gamma_\infty} = \frac{c_s / a}{1 + c_s / a} \tag{2-14}$$

where $a = \alpha / \beta$.

However, the Langmuir model fails to take into account the particle-particle interaction at the interface, which happens simultaneously with the adsorption process. Frumkin model has been proposed to account for this interaction:[23-25]

$$\frac{d\Gamma}{dt} = \beta \Gamma_\infty c_s (1 - \frac{\Gamma}{\Gamma_\infty}) - \alpha \Gamma e^{-K\Gamma/\Gamma_\infty} \tag{2-15}$$

where the parameter K is a measure of (net) attractive or repulsive interactions between the adsorbed particles ($K = 0$ leads to the same format as Langmuir model). By setting Equation 2-15 to be zero, we can get the Frumkin adsorption isotherm:

$$\frac{\Gamma}{\Gamma_\infty} = \frac{c_s / a}{\exp(-K\Gamma / \Gamma_\infty) + c_s / a} \tag{2-16}$$

where $a = \alpha / \beta$. Subsequently, the surface equation of state relating the surface tension γ to the surface concentration Γ is given by:

$$\gamma = \gamma_0 + RT\Gamma_\infty [\ln(1 - \frac{\Gamma}{\Gamma_\infty}) - \frac{K}{2}(\frac{\Gamma}{\Gamma_\infty})^2]. \tag{2-17}$$

where γ_0 is the initial surface tension of the clean interface.

2.4 Mass Transfer

The transport of particles or surfactants to an initially clean fluid-fluid interface is believed to follow three simultaneous transport properties:[19, 21-24, 26] (1) Particles or surfactants adsorb onto the interface from the subsurface region or desorb from the interface into the subsurface region. For large enough particles, desorption can be considered negligible; (2) In the absence of convective transport, particles or surfactants populate the subsurface region near the interface from the bulk by diffusion; (3) Particles or surfactants adsorbed at the interface may continue to re-orientate.

2.4.1 Governing Diffusion Equations

The adsorption of surfactants or particles onto a fresh fluid-fluid interface is modeled. For simplicity, let us start with one-dimensional diffusion and adsorption onto a flat interface from a bulk phase containing surfactants or particles of an initially uniform bulk concentration. The diffusion of particles in the bulk phase is described by Fick's law:

$$\mathrm{D}\frac{\partial^2 c}{\partial x^2} = \frac{\partial c}{\partial t} \quad (x > 0, t > 0) \tag{2-18}$$

with the following initial condition and boundary conditions:

$$c(x,t) = c_0 \qquad (x > 0, t = 0) \tag{2-19}$$

$$c(x,t) = c_0 \qquad (x \to \infty, t > 0) \tag{2-20}$$

$$\Gamma(t) = 0 \qquad (t = 0) \tag{2-21}$$

$$\frac{d\Gamma}{dt} = D\frac{\partial c}{\partial x}\Big|_{x=0^+} \quad (x = 0, t > 0) \tag{2-22}$$

where x and t are spatial and temporal coordinates, $c(x,t)$ is the particle concentration, c_0 is bulk particle concentration, D is diffusion coefficient, Γ is the surface concentration. Ward and Tordai[14] first established the solution to the above system in terms of an unknown subsurface concentration $c_s(t)$:

$$\Gamma(t) = 2c_0\sqrt{\frac{Dt}{\pi}} - 2\sqrt{\frac{D}{\pi}}\int_0^t c_s(t-\tau)d\tau^{1/2}. \tag{2-23}$$

It is worth noting that the previous assumption of one-dimensional diffusion toward a flat interface is not valid in the context of pendant droplet tensionometry, where the interface can be highly curved depending on the size of the droplet. Lin et al[22] showed the revised governing mass transfer equation in spherical coordinates:

$$\mathrm{D}\frac{1}{r}\frac{\partial}{\partial r}\left(r^2\frac{\partial c}{\partial r}\right) = \frac{\partial c}{\partial t} \qquad (r > b, t > 0) \tag{2-24}$$

$$\frac{d\Gamma}{dt} = D\frac{\partial c}{\partial r}\Big|_{x=b^+} \quad (r = b, t > 0) \tag{2-25}$$

$$c(r,t) = c_0 \qquad (r > b, t = 0) \tag{2-26}$$

$$c(r,t) = c_0 \qquad (r \to \infty, t > 0) \tag{2-27}$$

$$\Gamma(t) = 0 \qquad (t = 0) \tag{2-28}$$

where r is the spatial coordinate, b is droplet (or bubble) radius, and all the other symbols share the same meaning as above. It is shown by Lin et al[22] using Laplace transform that the above set of equations has the following solution in terms of unknown subsurface concentration $c_s(t) = c(r = b, t)$:

$$\Gamma(t) = \frac{D}{b}\left[c_0 t - \int_0^t c_s(\tau)d\tau\right] + 2\sqrt{\frac{D}{\pi}}\left[c_0\sqrt{t} - \int_0^{\sqrt{t}} c_s(t-\tau)d\sqrt{\tau}\right]. \qquad (2\text{-}29)$$

2.4.2 Scaling Argument for Coupled Adsorption/Desorption and Diffusion Processes

In the absence of convective mass transfer, the rate of exchange of particles between a fluid-fluid interface and the surrounding bulk phase is controlled by the kinetic flux between the interface and the bulk sublayer next to the interface, and the diffusive flux between the sublayer and the regions of the bulk phases far away from the interface.[23] The particle adsorption/desorption process and bulk diffusion process occur simultaneously, and their relative importance depends on the characteristic time scale for each one of them.

In 1998, Pan et al.[23] first compared the characteristic time scale of bulk diffusion and kinetic adsorption:

$$\tau_d = \pi\Gamma_c^2 / 4Dc_0^2 \qquad (2\text{-}30)$$

$$\tau_{kinetic} = (\alpha + \beta c_0)^{-1} \text{ (based on Langmuir model),} \qquad (2\text{-}31)$$

where τ_d and $\tau_{kinetic}$ are the characteristic time scale for the diffusion process and kinetic adsorption process, respectively, Γ_c is the surface concentration at equilibrium, D is the diffusion coefficient, c_0 is the bulk concentration, α and β are the desorption and adsorption rate constant in the Langmuir equation, respectively. The ratio of the diffusive to the kinetic time scale (which is defined as Φ^2) then becomes

$$\Phi^2 = \frac{\tau_d}{\tau_{kinetic}} = \frac{\Gamma_\infty^2 \beta^2}{D\alpha(c_0 / a)}, \tag{2-32}$$

assuming $c_0 / a \gg 1$ and Γ_c approaching Γ_∞, and ignoring $\pi / 4$, where $a = \alpha / \beta$. The above scaling argument indicates that as the bulk concentration increases, the kinetic time scale becomes longer relative to the diffusion time scale. Pan et al.[23] used the pendant bubble method to measure the dynamic surface tension in the presence of hexaethylene glycol monododecyl ether ($C_{12}E_6$), and showed the shifting to more kinetic influence for higher surfactant concentrations.

In 2004, Jin et al.[24] developed a new length scale, R_{D-K}, to determined whether the process is kinetically controlled or diffusion controlled. For a spherical bubble of radius b, the time scale for diffusion is

$$\tau_{Dsphere} = hb / D, \tag{2-33}$$

where h is the so called adsorption depth or depletion depth ($h = \Gamma_{eq} / c_{\infty}$), and D is the diffusion coefficient. The characteristic timescale for a purely adsorption/desorption-controlled flux (assuming Langmuirian kinetics) is given by

$$\tau_{ads-des} = \frac{1}{\beta c_{\infty} + \alpha}, \tag{2-34}$$

where α and β are the desorption and adsorption rate constant in the Langmuir equation, respectively, and c_{∞} is the bulk concentration. Then the ratio of these two timescales becomes:

$$\Lambda_{sphere} = \frac{hb / D}{1/(\beta c_{\infty} + \alpha)} = \frac{b}{R_{D-K}}, \tag{2-35}$$

neglecting the desorption constant α and Γ_c approaches Γ_{∞}, where $R_{D-K} = \frac{D}{\beta \Gamma_{\infty}}$ is defined. For droplets or bubbles with $b \ll R_{D-K}$, the overall mass transfer is kinetically controlled; for droplets or bubbles with $b \gg R_{D-K}$, the overall mass transfer is diffusion controlled. Jin et al.[24] used some previous literature results and estimated that R_{D-K} ranges roughly from 15 to 65 microns.

In 2010, Alvarez et al.[20] further developed the scaling analysis presented by Jin et al.[24]. They pointed out two flaws in Jin et al.'s argument: 1) although the diffusion-limited timescale $\tau_{Dsphere}$ suggests the radial dependence to account for the increase in the ratio of solution volume to surface area with decreasing radius, the time scale does not

approach that of the planar interface as the radius grows large and the curvature approaches zero, as people would expect; 2) the dimensionless time scale ratio does not contain bulk concentration dependence, which has been shown to shift the transition from diffusion-controlled region to kinetics-controlled region by Pan et al.[23] Instead, Alvarez et al.[20] proposed a new time scale to describe the transition of the dynamics, which accounts for both radius and concentration dependence:

$$\frac{R_{crit}}{R_{D-K}} = \frac{2}{\sqrt{12-3q^2}-3q}, \tag{2-36}$$

where R_{crit} is the critical radius at which the kinetic and diffusion time scales are equal, R_{D-K} shares the same meaning as in Jin et al.'s[24] argument, and $q = (R_{D-K} / h_p)^{1/3}$, where h_p is the depletion depth. This new time scale is validated by both numerical simulations and experimental data in Alvarez et al.'s paper[20].

It is interesting to note that according to the above time scale, any pendant droplet (or bubble) method for interfacial tension measurement falls into the region of diffusion-limited mass transport, because the size of the droplet (or bubble) greatly exceeds the critical radius. Therefore, we need an alternative method to measure interfacial tension to reveal the kinetic limitation. In the same year (2010), Alvarez et al.[19] developed a new experimental apparatus, a microtensiometer, which is capable to measure the dynamic surface tension for bubble radii ranging from 15 to 150 μm. This new technique reduces the time required to reach equilibrium using small bubbles, therefore is better to probe the kinetic-limited region than any other surface tension measurement method.

2.5 Summary

Both the particle adsorption tendency (thermodynamics) and adsorption rate (kinetics and mass transfer) determine the particle attachment efficiency in the flotation process. In this chapter, we first showed that for some hydrophilic particles, there is more energy benefit upon particles adsorption at the oil-water interface compared with the air-water interface. Then, we presented that the particle adsorption energy barrier is lower at the oil-water interface (oil-coated bubble surface) than at the air-water interface (uncoated bubble surface), indicating easier particle adsorption and potential benefit for the oil-coated bubble flotation. These findings add to our understanding of this novel oil-coated bubble system.

It is also worth mentioning that in the real flotation process, the bubble size is typically on the order of hundreds or even thousands of micrometers,[27] therefore the particle mass transport from the bulk phase to the bubble surface actually falls into the diffusion-limited region, and the benefit of lower particle adsorption energy barrier becomes less remarkable. Furthermore, in the presence of additional convection and turbulence, the diffusion limitation is also mitigated.

2.6 References

[1] Pieranski, P. Two-dimensional interfacial colloidal crystals. *Phys. Rev. Lett.* **1980,** *45* (7), 569-572.

[2] Binks, B. P.; Lumsdon, S. O. Influence of particle wettability on the type and stability of surfactant-free emulsions. *Langmuir* **2000,** *16* (23), 8622-8631.

[3] Zhang, Y.; Wu, J.; Wang, H.; Meredith, J. C.; Behrens, S. H. Stabilization of liquid foams through the synergistic action of particles and an immiscible liquid. *Angew. Chem. Int. Ed. Engl.* **2014,** *53* (49), 13603-13607.

[4] Paunov, V. N. Novel method for determining the three-phase contact angle of colloid particles adsorbed at air-water and oil-water interfaces. *Langmuir* **2003,** *19* (19), 7970-7976.

[5] Isa, L.; Lucas, F.; Wepf, R.; Reimhult, E. Measuring single-nanoparticle wetting properties by freeze-fracture shadow-casting cryo-scanning electron microscopy. *Nat. Commun.* **2011,** *2*.

[6] Kaz, D. M.; McGorty, R.; Mani, M.; Brenner, M. P.; Manoharan, V. N. Physical ageing of the contact line on colloidal particles at liquid interfaces. *Nat. Mater.* **2012,** *11* (2), 138-142.

[7] Zhang, Y.; Wang, S. C.; Zhou, J. R.; Benz, G.; Tcheimou, S.; Zhao, R. Y.; Behrens, S. H.; Meredith, J. C. Capillary foams: Formation stages and effects of system parameters. *Ind. Eng. Chem. Res.* **2017,** *56* (34), 9533-9540.

[8] Bhattacharjee, S.; Elimelech, M. Surface element integration: A novel technique for evaluation of dlvo interaction between a particle and a flat plate. *J. Colloid Interface Sci.* **1997,** *193* (2), 273-285.

[9] Israelachvili, J. Intermolecular and surface forces. Elsevier: Amsterdam, 2011.

[10] Marinova, K. G.; Alargova, R. G.; Denkov, N. D.; Velev, O. D.; Petsev, D. N.; Ivanov, I. B.; Borwankar, R. P. Charging of oil-water interfaces due to spontaneous adsorption of hydroxyl ions. *Langmuir* **1996,** *12* (8), 2045-2051.

[11] Tabor, R. F.; Chan, D. Y. C.; Grieser, F.; Dagastine, R. R. Anomalous stability of carbon dioxide in ph-controlled bubble coalescence. *Angew. Chem. Int. Ed.* **2011,** *50* (15), 3454-3456.

[12] Tabor, R. F.; Wu, C.; Lockie, H.; Manica, R.; Chan, D. Y. C.; Grieser, F.; Dagastine, R. R. Homo- and hetero-interactions between air bubbles and oil droplets measured by atomic force microscopy. *Soft Matter* **2011,** *7* (19), 8977-8983.

[13] Tabor, R. F.; Grieser, F.; Dagastine, R. R.; Chan, D. Y. C. Measurement and analysis of forces in bubble and droplet systems using afm. *J. Colloid Interface Sci.* **2012,** *371*, 1-14.

[14] Ward, A. F. H.; Tordai, L. Time-dependence of boundary tensions of solutions 1. The role of diffusion in time-effects. *J. Chem. Phys.* **1946,** *14* (7), 453-461.

[15] Fainerman, V. B.; Makievski, A. V.; Miller, R. The analysis of dynamic surface tension of sodium alkyl sulphate solutions, based on asymptotic equations of adsorption kinetic theory. *Colloids Surf., A* **1994,** *87* (1), 61-75.

[16] Bizmark, N.; Ioannidis, M. A.; Henneke, D. E. Irreversible adsorption-driven assembly of nanoparticles at fluid interfaces revealed by a dynamic surface tension probe. *Langmuir* **2014,** *30* (3), 710-717.

[17] Ravera, F.; Liggieri, L.; Steinchen, A. Sorption kinetics considered as a renormalized diffusion process. *J. Colloid Interface Sci.* **1993,** *156* (1), 109-116.

[18] Liggieri, L.; Ravera, F.; Passerone, A. A diffusion-based approach to mixed adsorption kinetics. *Colloids Surf., A* **1996,** *114*, 351-359.

[19] Alvarez, N. J.; Walker, L. M.; Anna, S. L. A microtensiometer to probe the effect of radius of curvature on surfactant transport to a spherical interface. *Langmuir* **2010,** *26* (16), 13310-13319.

[20] Alvarez, N. J.; Walker, L. M.; Anna, S. L. Diffusion-limited adsorption to a spherical geometry: The impact of curvature and competitive time scales. *Phys. Rev. E.* **2010,** *82* (1).

[21] Lin, S. Y.; McKeigue, K.; Maldarelli, C. Diffusion-controlled surfactant adsorption studied by pendant drop digitization. *AlChE J.* **1990,** *36* (12), 1785-1795.

[22] Lin, S. Y.; Tsay, R. Y.; Lin, L. W.; Chen, S. I. Adsorption kinetics of c(12)e(8) at the air-water interface: Adsorption onto a clean interface. *Langmuir* **1996,** *12* (26), 6530-6536.

[23] Pan, R. N.; Green, J.; Maldarelli, C. Theory and experiment on the measurement of kinetic rate constants for surfactant exchange at an air/water interface. *J. Colloid Interface Sci.* **1998,** *205* (2), 213-230.

[24] Jin, F.; Balasubramaniam, R.; Stebe, K. J. Surfactant adsorption to spherical particles: The intrinsic length scale governing the shift from diffusion to kinetic-controlled mass transfer. *J. Adhes.* **2004,** *80* (9), 773-796.

[25] Hua, X. Q.; Bevan, M. A.; Frechette, J. Reversible partitioning of nanoparticles at an oil-water interface. *Langmuir* **2016,** *32* (44), 11341-11352.

[26] Eastoe, J.; Dalton, J. S. Dynamic surface tension and adsorption mechanisms of surfactants at the air-water interface. *Adv. Colloid Interface Sci.* **2000,** *85* (2-3), 103-144.

[27] Maurice C. Fuerstenau, G. J., Roe-Hoan Yoon. Froth flotation-a century of innovation. **2007**.

CHAPTER 3. THE DYNAMICS OF RISING OIL-COATED BUBBLES: EXPERIMENTS AND SIMULATIONS[2]

3.1 Introduction

Bubble motion is very important in the froth flotation system, because it is related to the collision efficiency between the particles and bubbles, and it influences whether the particles adsorbed on the bubble surface can be retained until the bubble rises to the top surface. Air bubbles rising through an aqueous medium have been studied extensively. Oil-coated bubbles can be more effective for separating hydrophilic particles with low affinity for the air-water interface, but the rise dynamics of oil-coated bubbles has not yet been explored.

In the present work,[1] we report the first systematic study of the shape and rise trajectory of bubbles engulfed in a layer of oil. Results from direct observation of the coated bubbles with a high-speed camera are compared to computer simulations and confirm a pronounced effect of the oil coat on the bubble dynamics. We consistently find that the oil-coated bubbles display a more spherical shape and straighter trajectory, yet slower rise than uncoated bubbles of comparable size. These characteristics may provide practical benefits for flotation separations with oil-coated bubbles.

[2] This chapter has been published in Soft Matter (Wang S. et al, The dynamics of rising oil-coated bubbles: experiments and simulations, 2018, Soft Matter, 14, 2724-2734) and is reproduced by permission of the Roy al Society of Chemistry.

3.2 Methods

The dynamics of an oil coated bubble rising in a liquid is investigated by conducting experiments and direct numerical simulations. The experimental set-up, the method used to post-process the data obtained using the high-speed imagining and numerical method used in order to simulate the rise dynamics of an oil-coated bubble are discussed below.

3.2.1 Experimental Procedure

3.2.1.1 Apparatus

The bubble rise experiments were carried out in a square Plexiglas column with dimensions of 15 cm × 15 cm × 100 cm. The schematic diagram of the set-up is shown in Figure 3-1. The column was filled with deionized water or other testing liquids to a depth of 80 cm. Bubbles were generated at the bottom of the column by using an apparatus described below. The bubble motion was recorded by a high-speed camera (Phantom v7.0, Vision Research, Inc.) and image acquisition software (PCC v2.8, Vision Research, Inc.). The illumination of the test region was provided by a lamp with a diffuser behind the rectangular column. A scale bar was immersed into the column to determine the size and position of the bubbles. Obtained image frames were then analyzed using the Image J software.

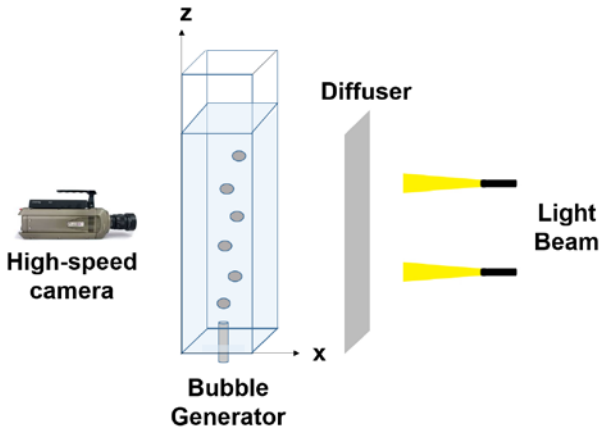

Figure 3-1 Schematic diagram of the experiment apparatus.

3.2.1.2 Materials

Silicone oil (10 cSt), and octane were purchased from Sigma-Aldrich and 1,6-Hexanediol diacrylate (HDDA) was obtained from Allnex Resins Co, Ltd. Octane and HDDA were purified with silica gel to remove any possible impurities. They were used to form oil-coated air bubbles. 2-hydroxy-2-methylopropiophenone was purchased from Sigma-Aldrich as the photo-initiator for the polymerization of HDDA. Ultra-pure water (18.2 MΩ•cm) was used as the medium fluid for observing bubble rise. Food grade cane sugar (“Great Value", Walmart) was used to adjust the medium fluid viscosity. The sugar solutions behave as Newtonian fluids for all the concentrations used in the present study. The purity of the sugar solutions was confirmed by measuring its surface tension and comparing it with literature values.[2-3]

3.2.1.3 Generating Oil-Coated Bubbles

Oils with positive spreading coefficient can completely engulf air bubbles.[4] Based on the material properties displayed in Table 3-1, we chose the fully engulfing silicone oil, octane, and HDDA to form a stable film around the air bubbles. Coated bubbles can be generated in many ways. In our work, we designed a small polystyrene chamber with an orifice at the top as shown in Figure 3-2. The chamber was first filled with oil, then air was introduced slowly. Once a small air bubble penetrates the orifice, it exits into the water with an oil coating. Air and oil were dispensed using two syringe pumps (NE-300, New Era Pump Systems, Inc.).

Table 3-1 Properties of the fluids used. Here, all the interfacial tensions are equilibrium tension (i.e. both phases are mutually saturated before measurement). The interfacial tensions for silicone oil-40 % (w.t.) sugar solution and octane-40 % (w.t.) sugar solution cannot be measured with pendant drop method because the refractive index of both phases are too close to be distinguished.

Fluids	Density $(g \cdot cm^{-3})$	Viscosity (cP)	Oil-air surface tension $(mN \cdot m^{-1})$	Water-air surface tension $(mN \cdot m^{-1})$	Oil-water interfacial tension $(mN \cdot m^{-1})$	Spreading coefficient $S_o(mN \cdot m^{-1})$
Saturated with DI water						
Silicone oil	0.93	9.3	18.8	69.3	41.3	9.2
Octane	0.7	0.5	21.2	72.8	43.9	7.7
HDDA	1.01	9.0	25.8	46.8	17.0	4.0
Saturated with 40 % (wt) sugar solution (5.8 cP)						

Silicone oil	0.93	9.3	19.4	75.0	-	-
Octane	0.7	0.5	21.4	72.4	-	-
HDDA	1.01	9.0	32.0	49.7	16.4	1.3
Saturated with 50 % (wt) sugar solution (13.0 cP)						
Silicone oil	0.93	9.3	21.5	75.3	39.9	13.9
Octane	0.7	0.5	20.7	74.2	35.4	18.1
HDDA	1.01	9.0	34.4	50.3	16.3	-0.4

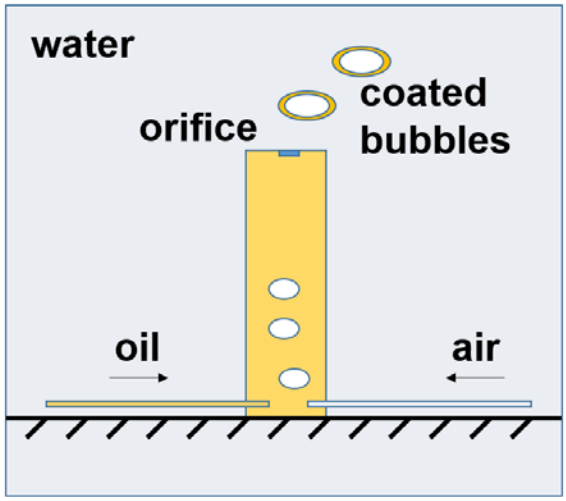

Figure 3-2 Mechanism to generate oil-coated bubbles.

3.2.1.4 Bubbles with Solidified Oil Coatings

In order to observe the coated-bubble morphology directly, we solidified bubble coatings of the photopolymerizable oil HDDA with 1.0 % (w.t.) photo-initiator. The polymerization proceeded fast enough (~ 10 s) under UV irradiation to convert the rising

oil-coated bubbles into hollow solid capsules by the time they reached the top of the column filled with a slightly viscous aqueous solution of the thickener xanthan gum. These hollow solid capsules were then collected and inspected optically.

3.2.1.5 Analytical Method

Bubble images (800 × 600 pixels) were taken at a speed of 500 frames per second. The terminal rising velocity was determined when velocity reached a plateau value. This was usually achieved within 0.5 s and within the first 15 cm above the bottom of the column.

As shown in Figure 3-3, we used Image J software to analyze the shape of the bubbles. The aspect ratio is defined as the minor axis, b, over major axis, a, which is in the range of 0 to 1. A higher aspect ratio indicates a more spherical bubble. We set 0.9 as an operational threshold for delineating a spherical shape.

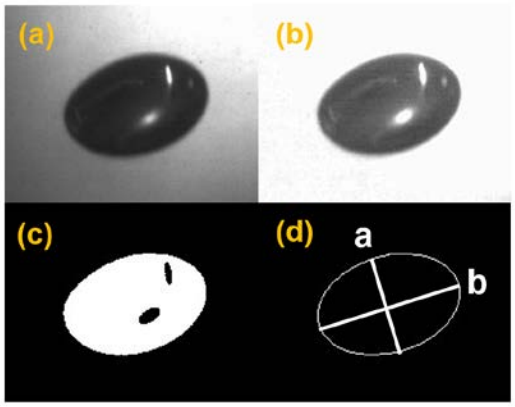

Figure 3-3 Steps followed in the image processing: (a) subtract the background, (b) convert into a binary image, (c) capture the boundary of the bubbles and (d) calculate the aspect ratio.

3.2.2 Numerical Method

The incompressible continuity and Navier-Stokes equations have been solved in the volume-of-fluid framework for numerically simulating a rising bubble in a quiescent liquid. The governing equations are as follows:

$$\nabla \cdot \mathbf{u} = 0 \tag{3-1}$$

$$\rho\left[\frac{\delta \mathbf{u}}{\delta t} + \mathbf{u} \cdot \nabla \mathbf{u}\right] = -\nabla p + \nabla \cdot \left[\mu(\nabla \mathbf{u} + \nabla \mathbf{u}^T)\right] + \delta\gamma\kappa\mathbf{n} - \rho g\mathbf{j} \tag{3-2}$$

$$\frac{\delta c}{\delta t} + \mathbf{u} \cdot \nabla c = 0 \tag{3-3}$$

where $\mathbf{u} = (u, v, w)$ denotes the velocity field, with the components u, v and w in the x, y and z directions, respectively, p denotes the pressure filed, ρ denotes density, μ denotes viscosity, t denotes time, g denotes the acceleration due to gravity, $\mathbf{j}$ denotes the unit vector along the vertical direction, γ denotes the interfacial tension, δ denotes the Dirac delta function (given by $|\nabla c|$), $\kappa = \nabla \cdot \mathbf{n}$ denotes the interfacial curvature and $\mathbf{n}$ denotes outward-pointing unit normal to the interface. The volume fraction variable c (=1 and 0 in the inner and outer phases, respectively) is maintained sharp by reconstructing the interface at every time step and by following a geometrical advection method[5] instead of a simple finite difference solution of the advection equation. The composite bubbles with an oil coat have been simulated in a simplified model as homogeneous effective bubbles

with only one interface, assigned an interfacial tension corresponding to the sum of the actual oil-air and oil-water interfacial tensions, with a density given by the volume average of the air and oil density, and the viscosity of oil.

A finite volume code, Gerris,[6] has been employed to solve the aforementioned equations in a Cartesian coordinate system. The domain geometry corresponds to the actual experimental setup, while the initial bubble shape has been assumed to be spherical in this numerical investigation. The present numerical code employs a balanced-force surface tension force calculation using height function based interface curvature estimation, which reduces the magnitude of spurious currents and makes the curvature estimation second order accurate. The numerical method has been tested and validated extensively in earlier works of the present authors.[7] All data, documentation and code used in this study will be made available upon request.

3.3 Results and Discussion

3.3.1 Bubble Morphology

The wetting behavior of the oil, air and water three-phase system can be predicted based on the spreading coefficient, S_o,[8-10] which is given by

$$S_o = \gamma_{aw} - (\gamma_{oa} + \gamma_{ow}), \tag{3-4}$$

where subscripts aw, oa and ow denote air-water, oil-air and oil-water interfaces, respectively. The spreading coefficient can be considered as the interfacial energy benefit

of replacing the air-water interface with an air-oil interface and an oil-water interface. Oils with positive spreading coefficient can spread spontaneously and form a film at the air-water interface, and thus completely engulf an air bubble in water. Oils with negative spreading coefficient, by contrast, form an oil lens at a flat air-water interface, and only partially engulf an air bubble.

Oil-air surface tension and oil-water interfacial tension were measured using the pendant drop method (ramé-hart Instrument Co.). Table 3-1 shows the measured tensions and the corresponding spreading coefficients for oils used in this work. Figure 3-4 shows a typical image of an air bubble and of a silicone oil coated air bubble dispensed from the orifice of the bubble generator.

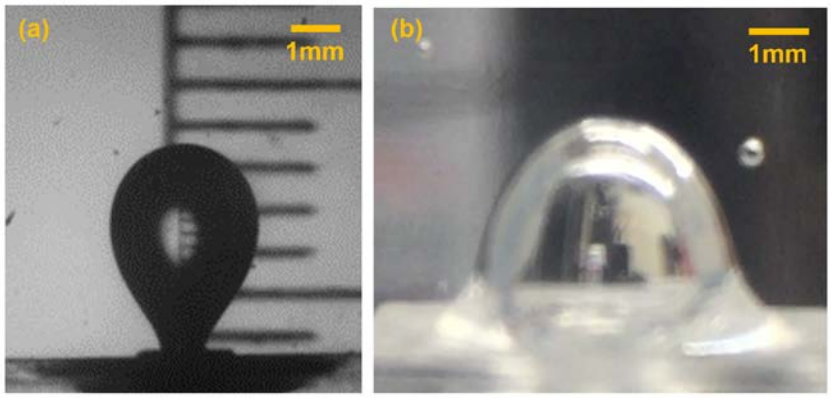

Figure 3-4 Typical images of (a) uncoated air bubbles, and (b) silicone oil coated air bubble.

While it is easy to observe the static bubble morphology, it is more challenging to image a rising bubble. The oil layer is not uniform around the whole bubble because of hydrodynamic effects, with a thinner ``front end'' and a thicker ``rear end''. The varying

thickness of the oil layer can be difficult to estimate based on in situ photography alone (see Figure 3-5, a typical image of a silicone oil coated bubble rising in deionized water).

To further characterize the morphology of a rising coated bubble (especially the morphology at the “front end"), we used HDDA with 1.0 % (w.t.) photo-initiator as the bubble coating. It also has positive spreading coefficient and can completely engulf the air bubble. It took less than 2 s for the polymerization to initiate under UV irradiation. We added xanthan gum into deionised water to increase the viscosity such that the coated-bubble can stay in the column for at least 10 s, which is enough for the polymerization to complete. Solid hollow spheres were formed before the bubbles reached to the top of the column (Figure 3-6). It is obvious that the oil layer is uneven around the whole bubble when it is rising. It is thinner at the ``front end" than the ``rear end", but the oil layer is indeed complete and continuous even at the front. It should be mentioned that the amount of HDDA used to produce the solid bubble coat shown in Figure 3-6 is exaggerated for experimental convenience, while all the following observations of bubble size, trajectory, velocity and shape are based on coated bubbles with a much smaller amount of oil (as shown in Figure 3-5). The added weight of oil was taken into account by using a volume averaged bubble density (200 $kg \bullet m^{-3}$), which was estimated based on the experimental air and oil flow rates (0.05 mL/min for the gas and 0.01 mL/min for the oil).

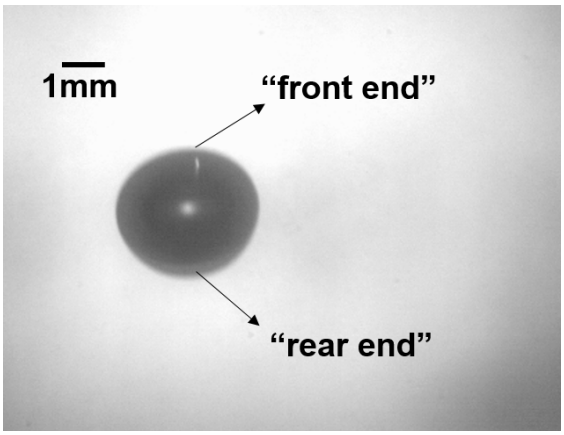

Figure 3-5 Image of a silicone oil coated bubble rising in deionized water.

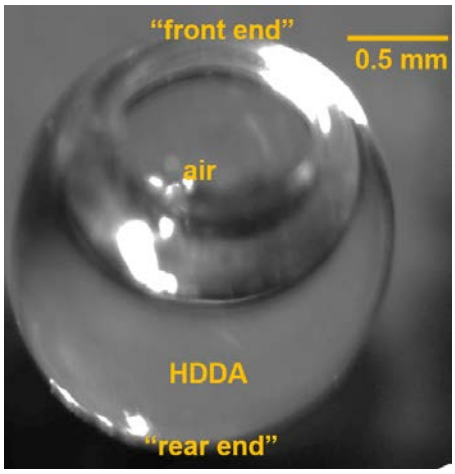

Figure 3-6 Image of a HDDA-coated bubble after polymerization.

3.3.2 Bubble Size

The detachment of an air bubble at the orifice inside the water medium can be obtained by balancing the buoyancy and surface tension forces. The size of a standard bubble just prior to pinch off can be estimated as follows (Tate's law)[11]

$$(\rho_w - \rho_a) g V = \pi d \gamma_{aw}, \tag{3-5}$$

where d is the orifice diameter, V is bubble volume, and ρ_w and ρ_a are the densities of water and air, respectively. We define D as the equivalent volume spherical bubble diameter and express the bubble volume in terms of D as $V = \pi D^3 / 6$. Neglecting air density from Equation 3-5 by assuming $\rho_a \ll \rho_w$, we obtain

$$\frac{D}{d} = 1.82 Bo^{-1/3}, \tag{3-6}$$

where

$$Bo = \frac{g d^2 \rho_w}{\gamma_{aw}} \tag{3-7}$$

is the so-called Bond number or Eötvös number. Equation 3-6 expresses the non-dimensional bubble diameter with respect to a non-dimensional group. It is worth noting that Tate's law is based on the assumption that the bubble neck is vertical at the orifice and the surface tension force is completely downwards. However, this is typically invalid, and the exponent and coefficient need to be corrected accordingly.[12] Here we obtained an empirical correlation (Equation 3-8) by fitting our experiment results (as shown in Figure 3-7)

$$\frac{D}{d} = 1.65 Bo^{-0.41}. \tag{3-8}$$

The discrepancy of the exponent and coefficient relative to Equation 3-6 may account for the specific experiment conditions, such as the gas flow rate and the volume of the chamber below the orifice, which have been shown by Davidson et al.[11] to have some influence on the bubble size.

We can also extend this correlation to oil-coated bubbles, but the a/w interfacial tension needs to be replaced with an effective bubble/fluid interfacial tension to account for the joint contributions of two interfaces. This effective tension can be approximated as the sum of the air-oil and oil-water interfacial tensions (62.2 mN/m and 55.4 mN/m for silicon oil coated bubbles and octane coated bubbles, respectively), which is consistent with the simulation results in the following section.

As Figure 3-7 shows, Equation 3-8 is in excellent agreement with experimental data for uncoated bubbles and oil-coated bubbles alike. We see that a model description for the bubble size dependence of uncoated bubbles on surface tension can also be applied to the oil-coated bubbles, provided that the surface tension is replaced by an appropriately chosen effective tension. Given how much more is known about uncoated bubbles than about coated bubbles, one might hope that equivalent behavior can be established more generally between coated bubbles and uncoated bubbles with appropriately chosen effective values for their governing properties.

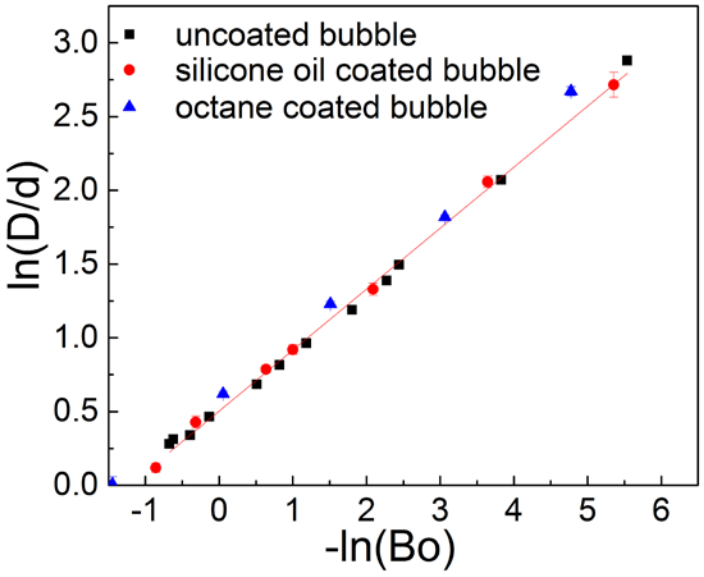

Figure 3-7 Equation 3-8 (line), and experimental results (symbols) for uncoated and oil-coated bubbles.

3.3.3 Bubble Rising Trajectory

Typical trajectories of uncoated and silicone oil coated bubbles of comparable size are shown in Figure 3-8. Both bubbles exhibit zigzagging trajectories when rising in water, but oil-coated bubbles display lateral excursions of lower amplitude.

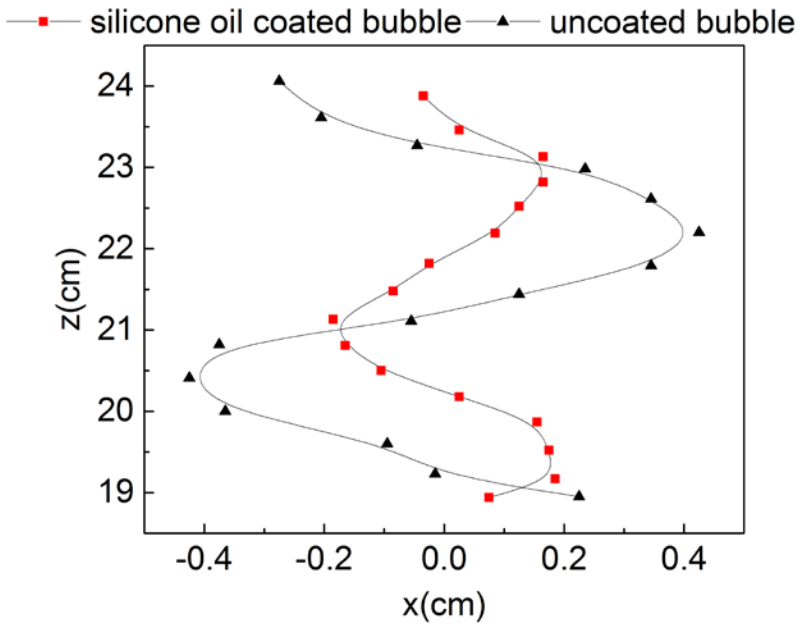

Figure 3-8 Typical trajectories of uncoated and oil-coated bubbles in deionized water. Bubble diameter D = 4 mm.

3.3.4 Bubble Rise Velocity

We measured the terminal rise velocity versus overall bubble diameter for both uncoated and oil-coated bubbles in three different fluids, namely, pure water (Figure 3-9a), 40 % (w.t.) sugar solution (Figure 3-9b) and 50 % (w.t.) sugar solution (Figure 3-9c). In all cases, oil-coated bubbles display lower rise velocity than uncoated bubbles. Lower velocity implies increased residence time for bubbles in a slurry during froth flotation and a consequently longer particle-bubble interaction time, likely to benefit flotation performance. Beyond this, Figure 3-9 is consistent with a well-known trend[13-14] that the bubble rise velocity increases with bubble size up to some threshold size, but decreases for larger bubbles when shape oscillations become more pronounced. The lower rise velocity

of oil-coated bubbles can be attributed to the reduced buoyant force caused by smaller density mismatch between the bubble and the aqueous phase, as shown in the following simulation results.

3.3.5 Bubble Shape

We plot the aspect ratio versus bubble diameter rising in deionized water, 40 % (w.t.) sugar solution and 50 % (w.t.) sugar solution for both uncoated and oil-coated bubbles in Figure 3-10(a), (b) and (c), respectively. An aspect ratio of 0.9 is often set as the threshold for a spherical shape. As we can see, oil-coated bubbles always display a more spherical shape than the uncoated bubbles. The suppression of shape oscillations by the oil coat also allows for a more precise measurement of the bubble size (smaller error bars). As simulation results shown below suggest, both the added weight of the oil and the effective increase in bubble viscosity contribute to keeping the oily bubbles more spherical.

It is interesting to note that oil-coated bubbles rising in pure fluids show similarities with uncoated bubbles rising in surfactant-contaminated fluids. Both of them display a lower rising velocity, a more spherical shape and a more stable trajectory than uncoated bubbles rising in clean fluids. The latter case has been explained by the fact that when surfactant adsorbs onto the bubble surface, it will be swept to and accumulate at the back of the bubble, which decreases the local surface tension and leads to a fore-to-aft surface tension gradient.[15-18] Due to the Marangoni effect, a tangential stress appears on the bubble surface and results the reduction of bubble rise velocity. The accumulated surfactant

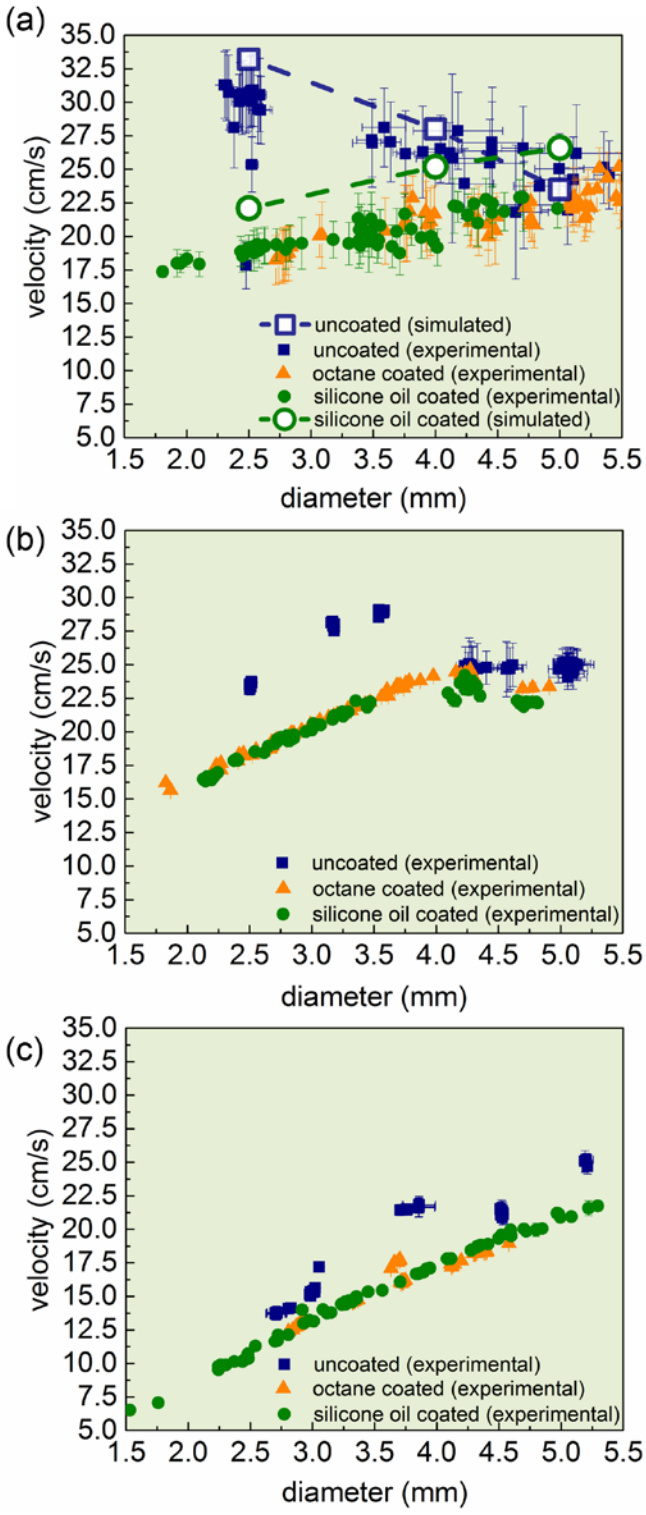

Figure 3-9 Terminal rising velocity of uncoated and oil-coated bubbles in (a) deionized water, (b) 40 % (wt) sugar solution and (c) 50 % (wt) sugar solution.

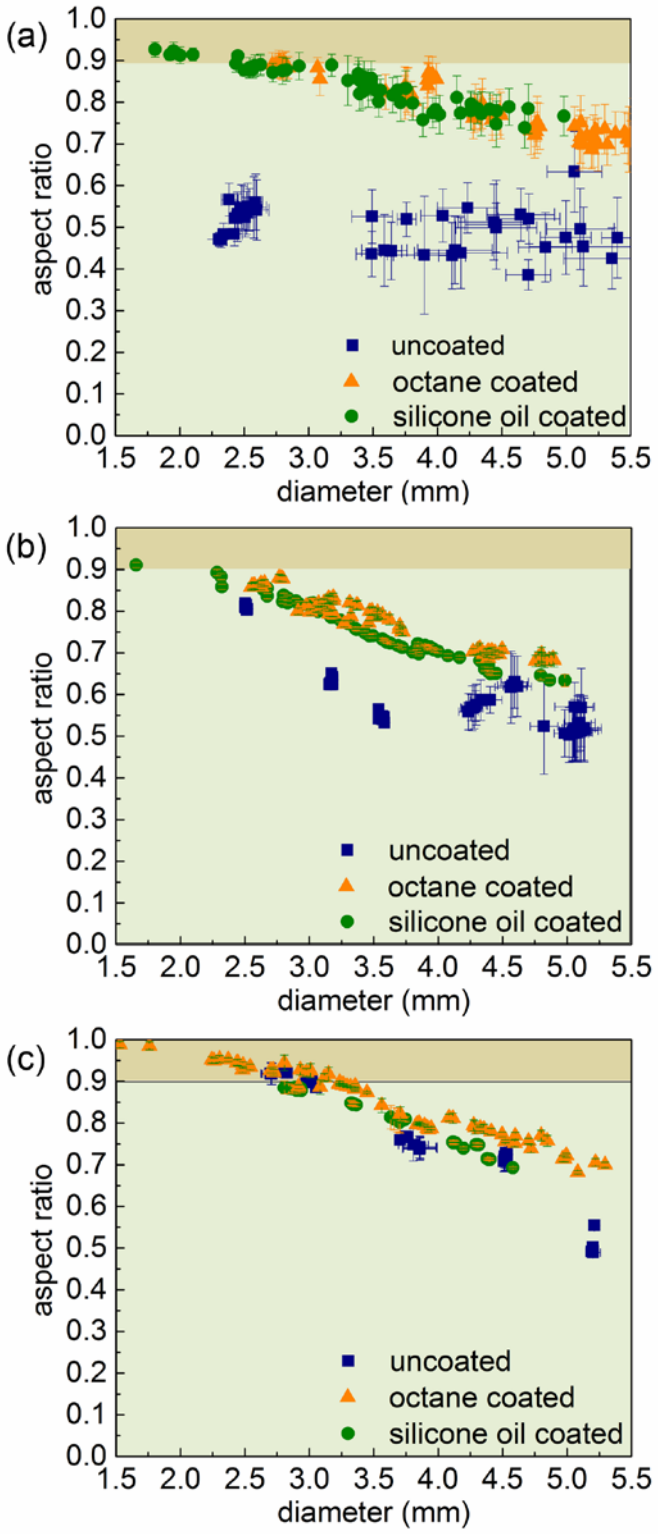

Figure 3-10 Experimental aspect ratio of uncoated and oil-coated bubbles in (a) deionized water, (b) 40 % (wt) sugar solution and (c) 50 % (wt) sugar solution.

at the “rear end” of the bubble forms the so-called rear stagnant cap that resists shape deformation, which is similar to the oil-mediated rigidification of the rising bubbles by an oil layer observed here.

3.3.6 Simulation Results

As mentioned above, oil-coated bubbles in water have been treated in the simulations as a single fluid phase with a bubble of density equal to the volume average of the air and oil density, a viscosity equal to that of the oil, and an interfacial tension equal to the sum of the oil-water and air-oil interfacial tensions. Using the sum of both interfacial tensions as the effective interfacial tension is a reasonable choice to account for the joint contributions of both interfaces. The overall bubble density is estimated based on the flow rate ratio between air and oil, and its effect on the bubble behavior is shown in Figure 3-11, Figure 3-12 and Table 3-2. It is clear that with increased bubble density, the oil-coated bubble displays slower rise velocity and a more spherical and more stable shape. For the effective bubble viscosity, a similar sensitivity analysis is conducted: the bubble viscosity is varied from air viscosity to oil viscosity (with all other parameters fixed), and it is observed that the case with oil viscosity gives the best agreement with experimental results (as shown in Figure 3-13, Figure 3-14 and Table 3-3. The increase of bubble viscosity effectively suppresses bubble shape deformation but does not change the bubble rise velocity significantly.

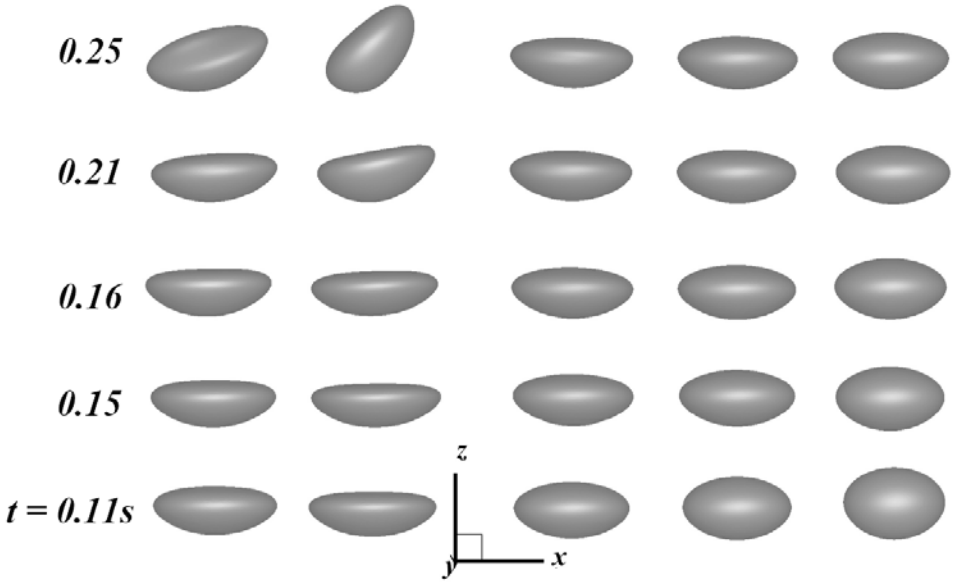

Figure 3-11 Effect of the density of the inner fluid on the bubble shapes: (a) 100 kg•m^{-3}, (b) 200 kg•m^{-3}, (c) 300 kg•m^{-3}, (d) 400 kg•m^{-3} and (e) 500 kg•m^{-3}. The values of viscosity of the inner and outer fluids are kept equal and constant ($\mu_i = \mu_o$ = 1 cP). The initial diameter of the bubble in all these cases is 4 mm.

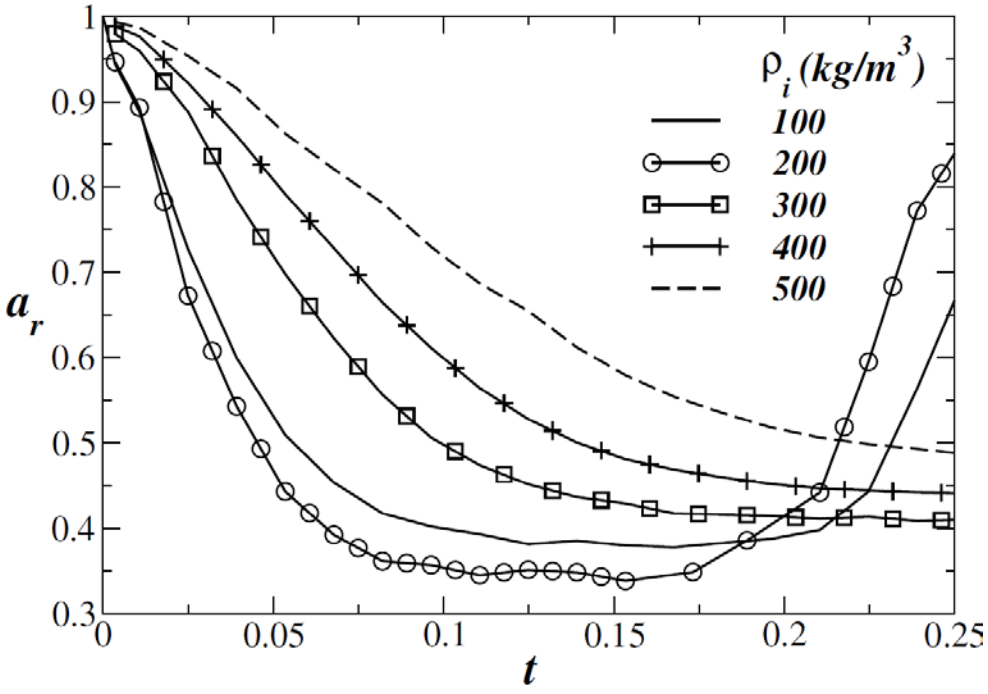

Figure 3-12 Temporal variations of aspect ratios of the bubble for different values of inner fluid density. The rest of the parameters are the same as those used to generate Figure 3-11.

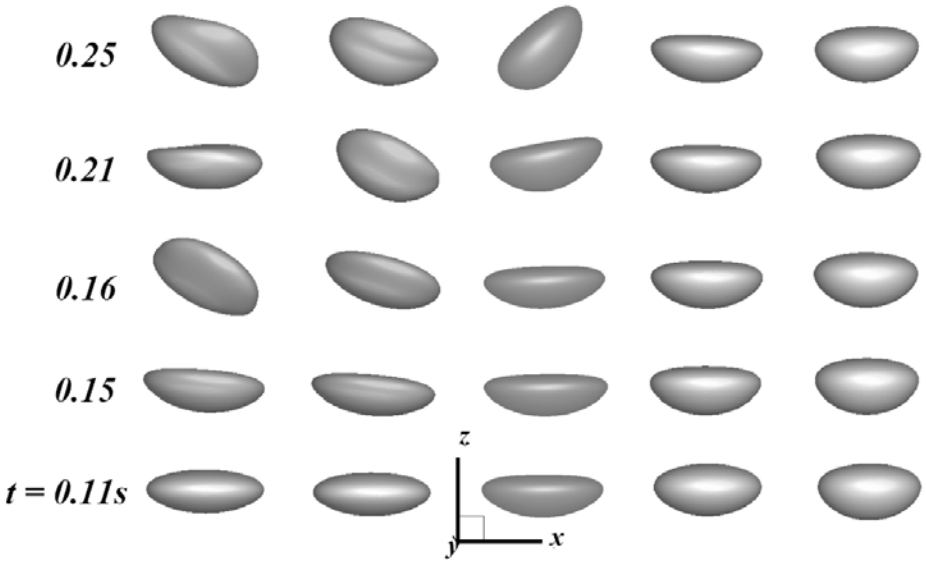

Figure 3-13 Effect of the viscosity of the inner fluid on the bubble shapes: (a) 0.015 cP, (b) 0.15 cP, (c) 1 cP, (d) 5 cP and (e) 9.3 cP. The density of the inner and outer fluids are 200 kg•m^{-3} and 998 kg•m^{-3}. The initial diameter of the bubble in all these cases is 4 mm.

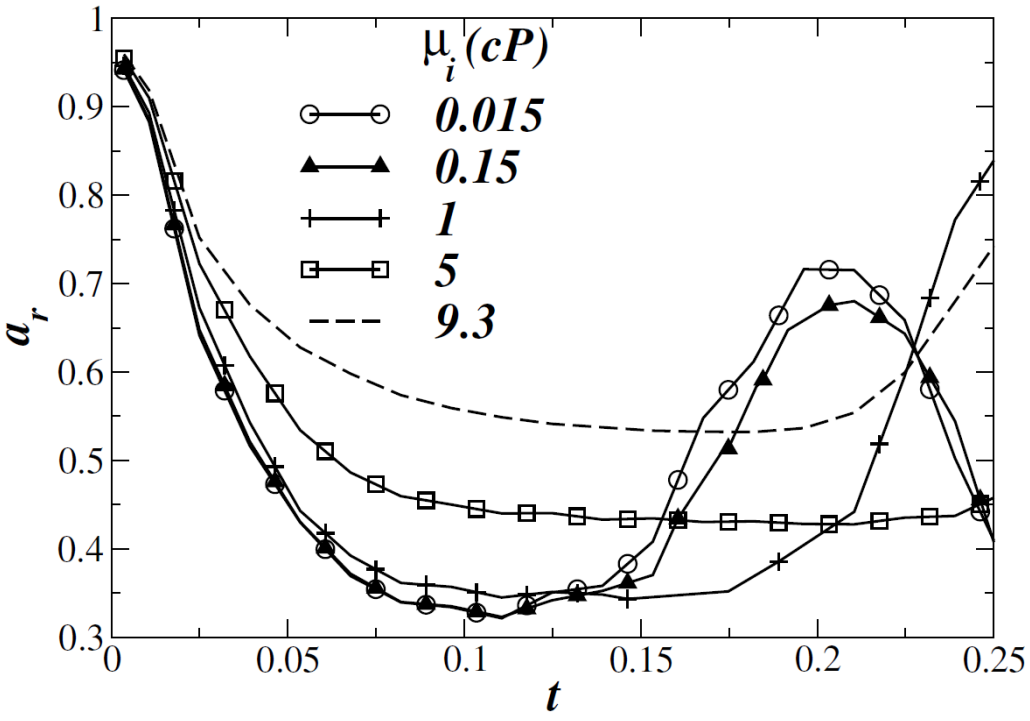

Figure 3-14 Temporal variations of aspect ratios of the bubble for different values of inner fluid viscosity. The rest of the parameters are the same as those used to generate Figure 3-13.

Table 3-2 Average terminal velocities for bubbles with different values of inner fluid density. The rest of the parameters are the same as those of Figure 3-11.

$\rho_i (kg \cdot m^{-3})$	Average $V_T (cm \cdot s^{-1})$
100	28.2
200	25.2
300	24.2
400	23.1
500	22.7

Table 3-3 Average terminal velocities for bubbles with different values of inner fluid viscosity. The rest of the parameters are the same as those of Figure 3-13.

$\mu_i (cP)$	Average $V_T (cm \cdot s^{-1})$
0.015	25.2
0.15	25.3
1	25.2
5	25.3
9.3	25.0

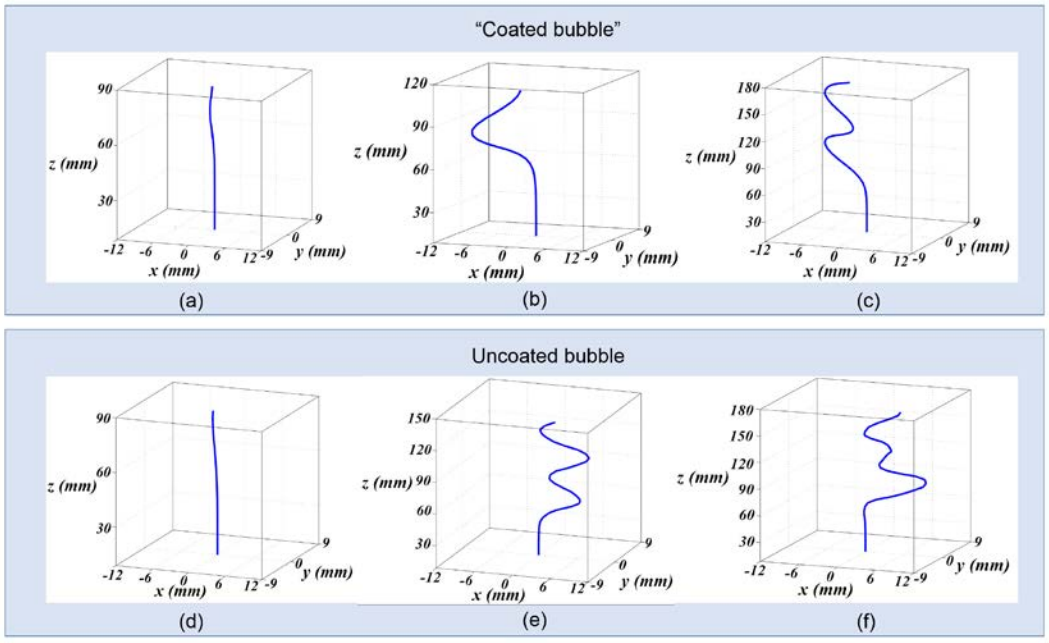

Figure 3-15 Numerical simulation results for trajectories of a "silicone oil coated bubble'' rising in water: (a) D = 2.5 mm, (b) D = 4 mm and (c) D = 5 mm. Numerical simulation results for trajectories of an uncoated bubble rising in water: (d) D = 2.5 mm, (e) D = 4 mm and (f) D = 5 mm. The quotes in the header serve as a reminder that the simulation models the coated bubbles in water as an effective two-phase system, see section 3.2.2: Numerical Method.

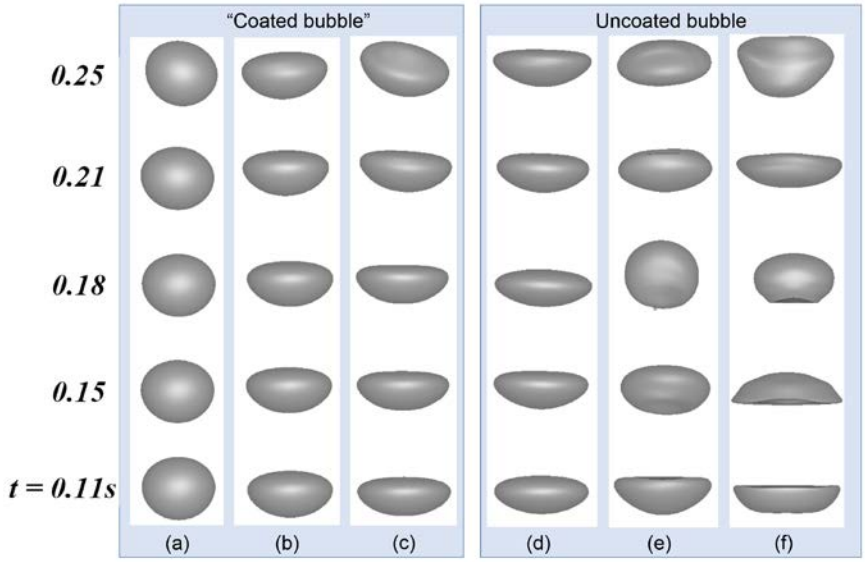

Figure 3-16 Numerical simulation results for shape evolutions of a "silicone oil coated bubble'' rising in water: (a) D = 2.5 mm, (b) D = 4 mm and (c) D = 5 mm. Numerical simulation results for trajectories of an uncoated bubble rising in water: (d) D = 2.5 mm, (e) D = 4 mm and (f) D = 5 mm. The quotes in the header serve as a reminder that the simulation models the coated bubbles in water as an effective two-phase system, see section 3.2.2: Numerical Method.

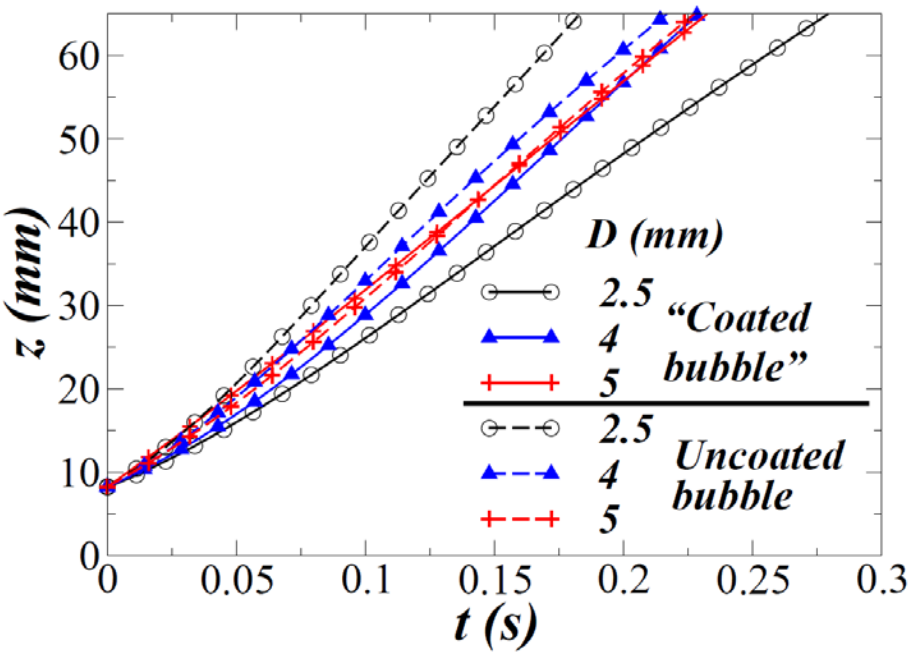

Figure 3-17 Evolution of center of gravity elevation for the bubbles shown in Figure 3-15 and Figure 3-16.

Based on the notion that the bubble buoyancy should be determined by the volume average density of their air and oil portion, considering further that the interfacial tensions of the air-oil and oil-water interface should be added to estimate their combined effect, and accounting for the observed viscosity effect on bubble shape and velocity, appropriate simulation parameters are assigned to enable direct comparison between the coated and uncoated bubbles of comparable size. For silicone oil-coated bubbles, effective bubble density, viscosity and interfacial tension are set to 200 kg•m^{-3}, 9.3 cP and 63 mN/m, respectively. Figure 3-15 and Figure 3-16 show the path (Figure 3-15) and the shape (Figure 3-16) of rising bubbles of D = 2.5 mm, 4 mm and 5 mm respectively, as obtained from the numerical simulations. The bubble shape is observed to oscillate more with increasing bubble size, but in all cases the shape of the "coated bubbles" is more spherical

and fluctuates less than the shape of the corresponding uncoated bubble. A quantitative comparison of the aspect ratio was not possible here, because the bubble undergoes continuous shape oscillations and does not reach a “steady state", even when it has reached the terminal rise velocity. The number of shape fluctuations observed within the limited time window accessible to our simulation was insufficient to compute a meaningful aspect ratio average.

The bubble rise velocity, however, attains a steady state in a very short time period (less than 0.1 s), and the terminal velocity is determined from the final slope in Figure 3-17. It is instructive to compare this simulated rise velocity to the one observed experimentally. For the uncoated bubbles rising in pure water (Figure 3-18 and Figure 3-19), the simulation results agree with the corresponding experimental results both qualitatively and quantitatively within the experimental uncertainty (Table 3-4 and Figure 3-9a), except for a small difference at lowest bubble size. The result is consistent with the well-known trend[13-14] that the rise velocity increases with bubble size up to some threshold size, but decreases for larger bubbles when shape deformation and oscillation become more pronounced. For the simulated “silicone oil coated bubbles", Figure 3-9a shows qualitative agreement with experimental results that the velocity increases monotonically with bubble size, and even the slope of this increase is captured well by the simulation. However, the simulation is seen to systematically overestimate the rise velocity of “coated bubbles". This quantitative disagreement cannot be explained by an uncertainty in the bubble density, as can be seen from Table 3-2: even simulated bubbles with much higher density than we can reasonably assume for the oil-coated bubbles in our experiments, still have higher velocities than were observed experimentally. Similarly, the discrepancy does not come

from misjudging the effective viscosity: as Table 3-3 clearly shows, the simulated velocity is extremely insensitive to bubble viscosity. We attribute the quantitative difference between the measured and simulated rise velocities of the oily bubbles (Figure 3-9a) to the crude single-phase representation of these bubbles in our simulation, which neglects the bubbles' actual composite structure and does not consider the flow recirculation within the thin film. Despite this oversimplification, the simulation is seen to capture the qualitative differences between oil-coated and uncoated bubbles very well.

Table 3-4 Comparison of experiment (Figure 3-9) and simulation (Figure 3-15 and Figure 3-16) with regard to the average terminal bubble velocities.

Diameter $D(mm)$	"Coated" (simulation) $V_T(cm \cdot s^{-1})$	Coated (experiment) $V_T(cm \cdot s^{-1})$	Uncoated (simulation) $V_T(cm \cdot s^{-1})$	Uncoated (experiment) $V_T(cm \cdot s^{-1})$
2.5	22.1	18.5 ± 1.2	33.2	30.0 ± 2.0
4	25.2	19.2 ± 1.4	28.0	26.5 ± 2.5
5	26.6	22.1 ± 1.4	23.5	22.0 ± 2.6

Combining the information from the sensitivity analysis for the effective bubble density and viscosity, it is clear that the reduced rise velocity of oil-coated bubbles can be attributed primarily to the reduced buoyant force due to added weight of oil coat, whereas the more spherical shape and more stable trajectory appear to be caused by both buoyancy and viscosity effects of the oil. Potentially relevant details of the composite bubble

morphology and of flow inside the oil coat obviously cannot be resolved in the present simplified simulations. Much more work in future studies will be required to remove these remaining limitations.

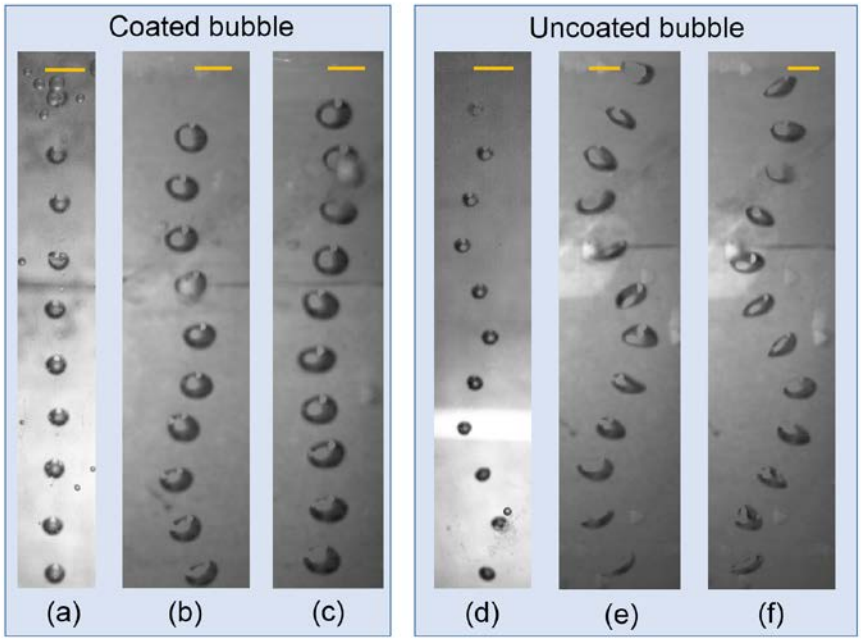

Figure 3-18 Experimental results for trajectories of a silicone oil coated bubble rising in water: (a) D = 2.5 mm, (b) D = 4 mm and (c) D = 5 mm. Experimental results for trajectories of an uncoated bubble rising in water: (d) D = 2.5 mm, (e) D = 4 mm and (f) D = 5 mm. The time interval is 0.03 s and the scale bar is 5 mm.

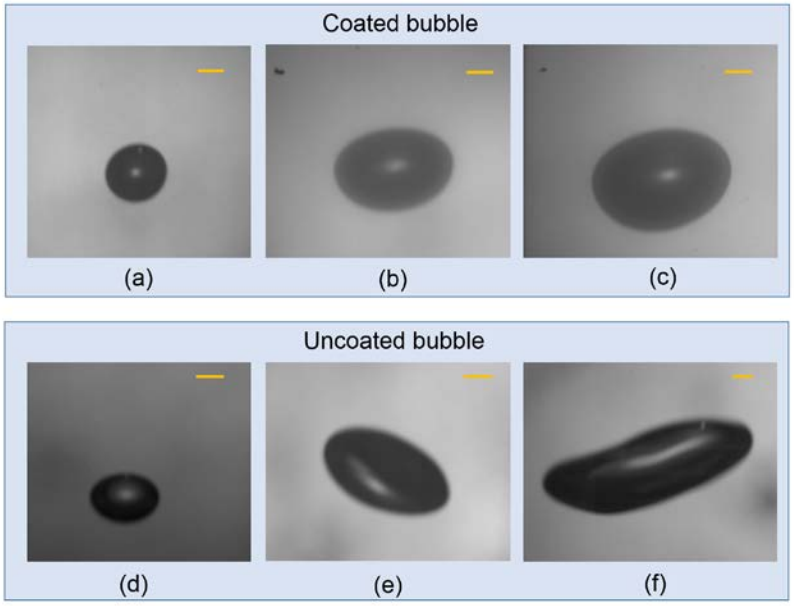

Figure 3-19 Typical images of a silicone oil coated bubble rising in water: (a) D = 2.5 mm, (b) D = 4 mm and (c) D = 5 mm. Typical images of an uncoated bubble rising in water: (d) D = 2.5 mm, (e) D = 4 mm and (f) D = 5 mm. The scale bar is 1 mm.

3.4 Conclusions

In summary, the rise dynamics of a single oil-coated bubble has been systematically investigated for the first time to the best of our knowledge. The bubble morphology, size, velocity, shape and trajectory are obtained from the frames taken by a high speed camera. Oil-coated bubbles display a lower rise velocity, a steadier and more spherical shape, and less pronounced lateral excursion than uncoated bubbles of comparable size.

The experiments were complemented by bubble rise simulations based on the volume-of-fluid (VOF) method with dynamic adaptive grid refinement. Oil-coated bubbles were simulated in a simplified model as a single fluid phase with 1) an effective surface

tension given by the sum of the air-oil and oil-water interfacial tensions; 2) an effective bubble density accounting for the mass contribution of oil coat, and 3) an effective bubble viscosity equal to the oil phase viscosity. Despite the simplicity of this model, the simulations captured the salient qualitative features distinguishing oil-coated and uncoated bubbles with respect to terminal velocity, bubble trajectory and bubble shape dynamics.

3.5 References

[1] Wang, S. C.; Zhang, Y.; Meredith, J. C.; Behrens, S. H.; Tripathi, M. K.; Sahu, K. C. The dynamics of rising oil-coated bubbles: Experiments and simulations. *Soft Matter* **2018,** *14* (14), 2724-2734.

[2] Lindfors, K. R. Surface tension of sugar factory products. *Ind. Eng. Chem.* **1924,** *16*, 813-816.

[3] Vazquez, G.; Alvarez, E.; Navaza, J. M. Density, viscosity, and surface tension of sodium carbonate plus sodium bicarbonate buffer solutions in the presence of glycerine, glucose, and sucrose from 25 to 40 degrees c. *J. Chem. Eng. Data* **1998,** *43* (2), 128-132.

[4] Zhang, Y.; Wu, J.; Wang, H. Z.; Meredith, J. C.; Behrens, S. H. Stabilization of liquid foams through the synergistic action of particles and an immiscible liquid. *Angew. Chem. Int. Ed.* **2014,** *53* (49), 13385-13389.

[5] Popinet, S. An accurate adaptive solver for surface-tension-driven interfacial flows. *J. Comput. Phys.* **2009,** *228* (16), 5838-5866.

[6] Popinet, S. Gerris: A tree-based adaptive solver for the incompressible euler equations in complex geometries. *J. Comput. Phys.* **2003,** *190* (2), 572-600.

[7] Tripathi, M. K.; Sahu, K. C.; Govindarajan, R. Dynamics of an initially spherical bubble rising in quiescent liquid. *Nat. Commun.* **2015,** *6*, 6268.

[8] Mason, S. T. a. S. G. Three-phase interactions in shear and electrical fields. *J. Colloid Interface Sci.* **1970,** *33*, 67-83.

[9] Pannacci, N.; Bruus, H.; Bartolo, D.; Etchart, I.; Lockhart, T.; Hennequin, Y.; Willaime, H.; Tabeling, P. Equilibrium and nonequilibrium states in microfluidic double emulsions. *Phys. Rev. Lett.* **2008,** *101* (16), 164502.

[10] Guzowski, J.; Korczyk, P. M.; Jakiela, S.; Garstecki, P. The structure and stability of multiple micro-droplets. *Soft Matter* **2012,** *8* (27), 7269.

[11] Davidson, L. a. A., E. H. Formation of gas bubbles at horizontal orifices *AlChE Journal* **1956**.

[12] Benzing, R. J.; Myers, J. E. Low frequency bubble formation at horizontal circular orifices. *Ind. Eng. Chem.* **1955,** *47* (10), 2087-2090.

[13] Clift, R.; Grace, J. R.; Weber, M. E. *Bubbles, drops, and particles*; Dover: Mineola, NY, 2013.

[14] Gaudin, A. M. *Flotation*; McGraw-Hill1957.

[15] Ratulowski, J.; Chang, H. C. Marangoni effects of trace impurities on the motion of long gas bubbles in capillaries. *J. Fluid Mech.* **1990,** *210*, 303-328.

[16] Cuenot, B.; Magnaudet, J.; Spennato, B. The effects of slightly soluble surfactants on the flow around a spherical bubble. *J. Fluid Mech.* **1997,** *339*, 25-53.

[17] Takagi, S.; Matsumoto, Y. Surfactant effects on bubble motion and bubbly flows. *Annual Review of Fluid Mechanics, Vol 43* **2011,** *43*, 615-636.

[18] Dukhin, S. S.; Lotfi, M.; Kovalchuk, V. I.; Bastani, D.; Miller, R. Dynamics of rear stagnant cap formation at the surface of rising bubbles in surfactant solutions at large reynolds and marangoni numbers and for slow sorption kinetics. *Colloids Surf., A* **2016,** *492*, 127-137.

CHAPTER 4. CAPILLARY FOAM – A CONVENIENT METHOD TO EVALUATE PARTICLE FLOATABILITY

4.1 Introduction

In previous chapters, we have presented the thermodynamic, kinetic and hydrodynamic benefits of oil-coated bubble flotation over the conventional uncoated bubble flotation. Next, we are interested to evaluate the abilities of particles to be collected and separated by oil-coated bubbles (referred to as "particle floatability" in the remaining thesis). But before we perform large-scale flotation experiments directly (which can be time and material consuming), we will first work on a slightly different but closely related system – the aqueous foam system, to evaluate the impact of some system parameters, which can help us disqualify some specific particle-oil combinations that are unlikely to succeed in the oil-coated bubble flotation.

In the particle-stabilized foam system (Pickering foam and capillary foam), in order to create a significant amount of foams, the particles need to have a good affinity for the air-water interface or the oil-water interface. This is similar to what is happening in froth flotation: in order for efficient particle separation, the particles need to have a good affinity for the bubble surface (either uncoated or oil-coated). With this similarity and connection between the aqueous foam system and the froth flotation system, the foaming test can be used as a convenient assay to study the particle floatability: particles that can create a significant amount of capillary foam (having a good foamability) display better affinity for the oil-water interface, and are therefore more likely to be separated by oil-coated bubbles.

It is worth mentioning that there are two important properties of aqueous foams: stability and foamability. In the context of froth flotation, foamability is of more interest, because it is directly related to the entrainment of particles. Meanwhile, foams that are overly stable are not desired, because they add no additional benefit to particle entrainment but can add more difficulty to the downstream processing steps (*i.e.*, the transport of froth in pumps and pipelines).

The main objective of this chapter is to better understand the foamability of capillary foam system. Silica particles were used because they allow for convenient modification of the surface hydrophobicity to reveal the potential variation in foamability. We followed the standard practice to make capillary foams and measured the initial foam height to describe the foamability. Several important parameters including particle wettability, ionic strength, pH, and frothing speed were evaluated. The knowledge we learned from this chapter will be very useful if applied to the design and optimization of froth flotation. This work also adds to our understanding of the formation mechanism of capillary foams and acts as a useful guide to enhance the foamability for other practical applications.

4.2 Experimental Section

4.2.1 Materials

Trimethylolpropane trimethacrylate (TMPTMA) and octadecyltrichlorosilane (OTS) were purchased from Sigma-Aldrich. Sulfuric acid (95 – 98 wt %) and hydrogen

peroxide (30 wt %) were purchased from BDH Chemicals. Deionized water with a resistivity of 18.2 MΩ·cm was used. Amorphous fumed silica particles with different degrees of hydrophobicity (modified by dichlorodimethylsilane, with 100%, 70%, 50% and 36% residual SiOH on the surface) were provided by Wacker-Chemie AG (Germany). Particle size and zeta potential were determined using a Malvern Zetasizer Nano ZS90. The hydrodynamic radius of the above silica particles in 0.1 mM NaCl solution at neutral pH is shown in Table 4-1.

Table 4-1 Hydrodynamic radius of silica particles with different degree of surface modification by dichlorodimethylsilane.

Particle (residual silanol %)	100 %	70 %	50 %	36 %
Radius (nm)	130.8 ± 3.8	83.0 ± 1.2	89.4 ± 1.7	69.6 ± 0.6

4.2.2 Contact Angle Measurement

Static contact angles of the aforementioned four types of silica have been measured in our previous work using compressed silica pellets as the solid substrate.[1] However, it was observed that the surface roughness of the pellets may affect the angle measurement strongly and in ways that are difficult to assess. Moreover, since the formation of capillary foam relies on the dynamic wetting behavior of oil on the pre-wetted particle surface, it makes more sense to measure the dynamic contact angle instead. To mitigate the effect of surface roughness, the contact angle was measured in an approximate fashion by preparing

surface-modified glass slides instead of using the pressed silica pellets. The glass slide was treated following an otherwise reported procedure to mimic the most hydrophobic silica particle surface.[2] Briefly, the glass slide was first placed in a freshly prepared piranha solution (3 parts of 95 – 98 wt% concentrated sulfuric acid and 1 part of 30 wt% hydrogen peroxide solution) for two hours to remove any remaining organic contaminants. Then the glass slide was dried and placed into toluene containing 2 mM OTS for 12 h. Subsequently, the substrate was transferred to an oven and was baked for 20 min at 120 °C. Finally, the glass slide was rinsed with toluene, ethanol, deionized water and dried in nitrogen.

The contact angle of the treated glass slide was measured in a quartz-cell using a Ramé-Hart goniometer. The substrate was immersed into the quartz cell filled with deionized water, and an oil droplet was then deposited with a 22 gauge needle. The drop volume control device was used to increase or decrease the volume of the oil droplet, and images of oil advancing or receding angles were obtained using the DROPimage software. The reported values are the angles measured through water (supplementary to the angles through oil), and water advancing/receding angles correspond to oil receding/advancing angles, respectively.

4.2.3 Making Capillary Foams

A silica particle suspension in water containing a certain amount of particles (3 wt %, with respect to the water bulk phase) was first prepared in a 7 mL glass vial. Then a small amount of TMPTMA (1 wt %) was added into the vial. Finally, the mixture was mechanically frothed using a rotor-stator homogenizer (IKA Ultra-Turrax T10, stator

diameter of 8 mm and rotor diameter of 6.1 mm) at 30,000 rpm for 1 min. To ensure consistent results, the rotor and stator of the homogenizer were always immersed at the same depth (5 mm) into the bulk phase when the homogenization just started, although it did not have a noticeable impact on foamability because the turbulence was so strong. Images were taken immediately when the process was completed and the initial foam height was also measured immediately.

4.3 Results and Discussion

4.3.1 Effect of Particle Wettability and Ionic Strength

The effect of particle wettability and ionic strength on the foamability are shown in Figure 4-1. For hydrophilic silica particles (100% and 70% SiOH), there is hardly any foam created regardless of ionic strength. However, for partially hydrophobized silica particles (50% and 36% SiOH), a noticeable amount of stable foam was produced even in the absence of salt. This can be explained by the difference in thermodynamic energy benefit (driving force) of particle adsorption. The reduction in the interfacial energy upon adsorption of a single particle to the interface is given by:[3-4]

$$\Delta G_{ad,ij} = -\pi R^2 \gamma_{ij} \left(1 - \left|\cos\theta_{ij}\right|\right)^2 \qquad (4\text{-}1)$$

where γ_{ij} denotes the surface (or interfacial) tension of the clean interface, θ_{ij} is the contact angle of a single particle at the interface, and R is the particle radius. The larger free energy reduction upon particle adsorption, the stronger particle attachment to the interface,

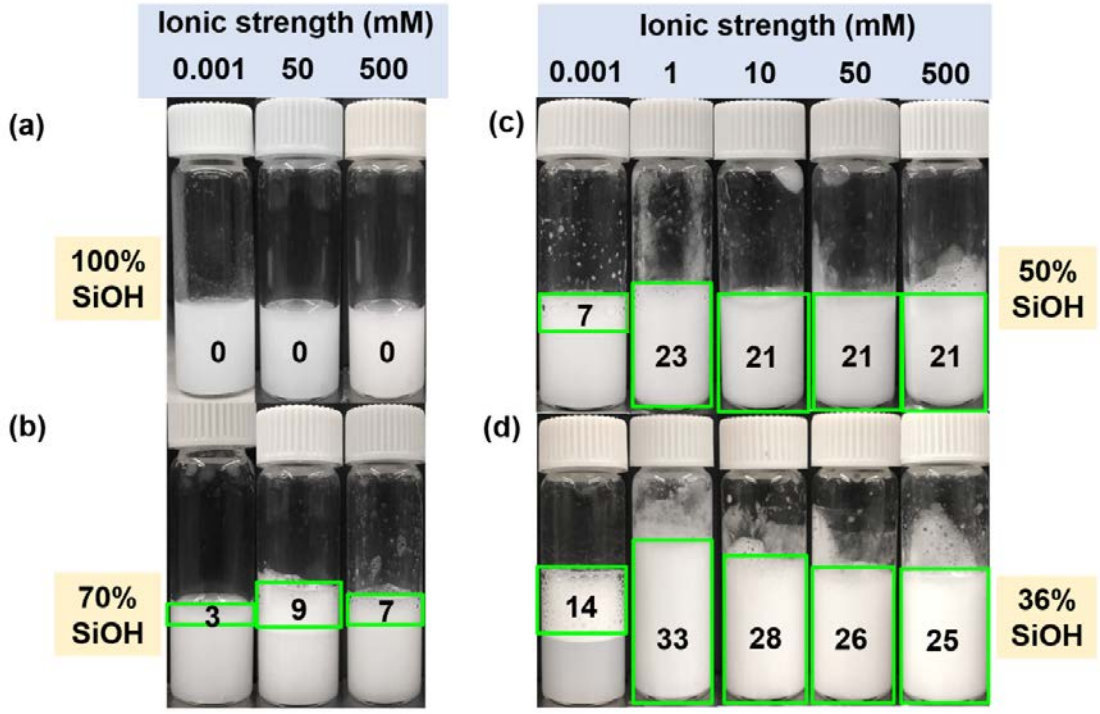

Figure 4-1 Initial foam height (mm) of capillary foams made with different silica particles at various ionic strengths: (a) 100% SiOH, (b) 70% SiOH, (c) 50% SiOH and (d) 36% SiOH. All experiments were performed at neutral pH. pH and ionic strength were controlled using KH_2PO_4/K_2HPO_4 buffer. The ionic strength in this paper only considers the contribution from the additional buffer ingredients, not including the potential trace amount of contaminants in DI water (which can be considered negligible). The green box denotes the capillary foam phase. There exists a clear boundary between the foam phase and the remaining bulk aqueous phase, which can be distinguished easily when measuring foam height.

therefore better foamability would be expected. For the same type of particles with similar size absorbing at the same fluid-fluid interface, the free energy reduction is larger if the three-phase contact is closer to 90°. The above observation is also consistent with our previous studies: with the particles being more hydrophobic, the three-phase contact angle at the oil-water interface gets closer to 90°, which is more thermodynamically favored, thus more stable foams can be created.[1]

When the particle wetting is beneficial (*e.g.*, 36% SiOH silica particles), the boosting of foamability upon adding a small amount of salt can be attributed to the change in the kinetic particle adsorption energy barrier. It is known that silica particles and oil droplets are both negatively charged in aqueous media above pH 4, and a resulting electrostatic energy barrier can hinder the adsorption of silica particles onto the oil-water interface.[5-7] This electrostatic interaction can be screened by adding salt ions. As shown in Figure 4-1, for partially hydrophobized silica particles (50% and 36% SiOH), the foamability is significantly enhanced by adding as little as 1 mM salt (initial foam height increases from 7 mm to 23 mm for 50% SiOH silica and from 14 mm to 33 mm for 36% SiOH silica). This can be explained by the screening of particle surface charge and a resulting lower particle adsorption energy barrier, as confirmed by the zeta potential determination (Figure 4-2) and the calculation in the following section (Figure 4-9).

Adding more salt, however, does not further improve the foamability, arguably because the particle surface charge is already sufficiently screened and the Debye length does not significantly decrease any more (the Debye lengths corresponding to 1 mM, 10 mM, 50 mM, and 500 mM ionic strength are 9.6 nm, 3.0 nm, 1.4 nm and 0.4 nm, respectively). Instead, a slight decrease of the initial foam height is actually observed with the further increase of ionic strength, which is believed to result from the change in particle wettability. To confirm our hypothesis, we prepared some glass slides to mimic the most hydrophobic silica particle surface, and measured the three-phase contact angle at various ionic strengths (as shown in Figure 4-3). We find that the surface becomes more and more hydrophobic at increased ionic strength (or decreased Debye length), and the three-phase contact angle deviates more and more from 90°, thus there is less energy benefit for the

particle to adsorb onto the interface and a decrease in initial foam height can be therefore expected (as indicated by Equation 4-1). This observation is also consistent with Simovic's and Kostakis's previous studies showing that silica particles become more hydrophobic at increased salt concentration.[8-10] For the hydrophilic silica particles (100% and 70% SiOH), however, the initial foam height does not increase no matter how much salt is added. This is because even though the kinetic particle adsorption barrier is significantly lowered, the particles are too hydrophilic to adsorb strongly at the oil-water interface, thus good foamability cannot be observed.

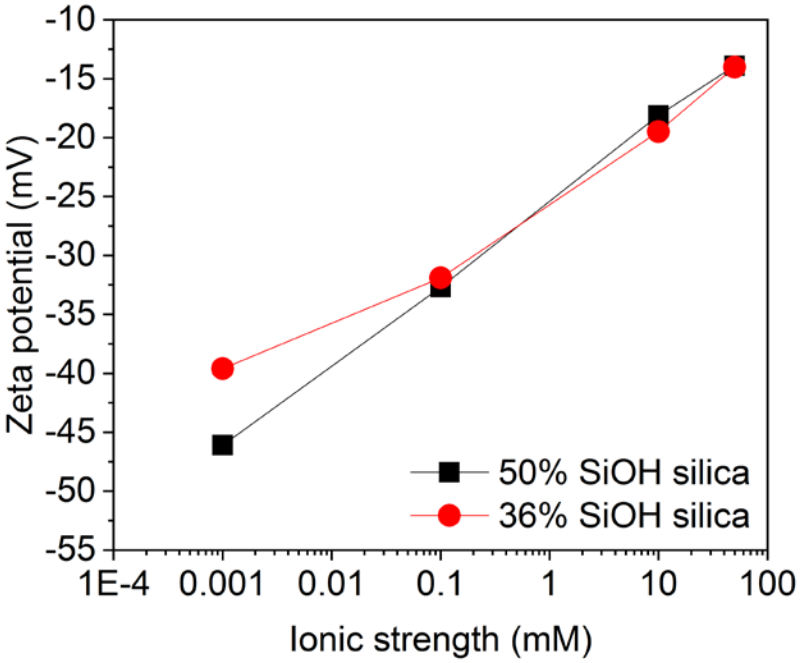

Figure 4-2 Zeta potential of partially hydrophobic silica particles (50% and 36% SiOH) at various ionic strengths. The pH was fixed as neutral using buffer solution.

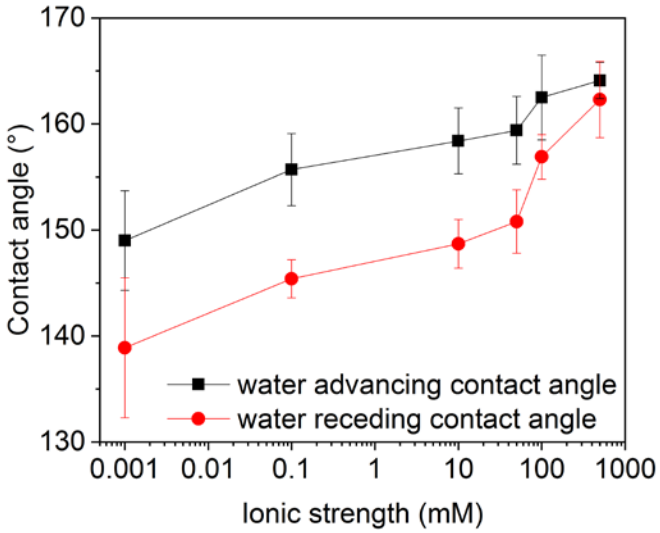

Figure 4-3 Dynamic contact angle of the modified glass slide surface. The pH was fixed as neutral using buffer solution.

4.3.2 Effect of pH

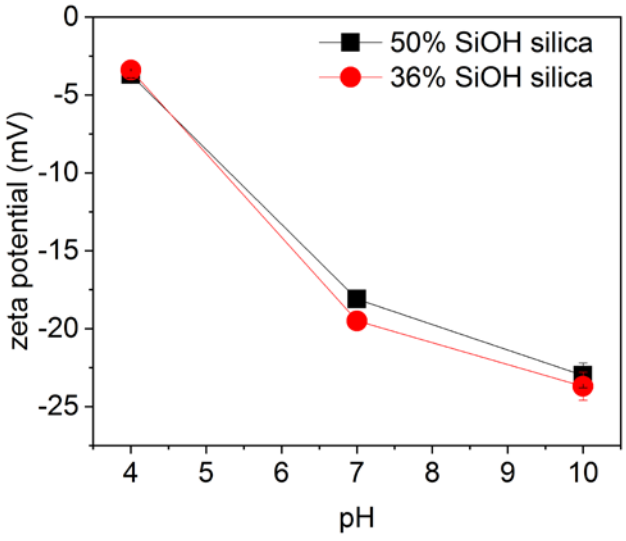

Figure 4-4 Zeta potential of partially hydrophobic silica particles (50% and 36% SiOH) at various pH. The ionic strength was fixed at 10 mM.

The surface charge of silica particles is influenced not only by salt concentration, but also by pH. As pH increases, the silica particle surface develops more negative charges due to the deprotonation of the silanol group (as shown in Figure 4-4). It is worth noting that the particles with 50% and 36% residual SiOH show identical charging behavior (within measurement uncertainty), which may at first be surprising, since the dissociation of the surface silanol group is the (primary) source of surface charge. The reason it makes no significant difference to charging (no matter whether 50% or 64% of silanol groups are unavailable because of the surface modification) – is the dissociation constant and small average spacing between silanol groups on silica surfaces (surface density of ~ 8 nm^{-2}, pKa ~ 7.5): even at 100% SiOH only a fraction of these groups can ever dissociate because of the excessive electrostatic cost of charging neighboring sites.[6]

With higher surface charge and resulting higher particle adsorption energy barrier, lower initial foam height should be expected. To confirm our hypothesis, the foamability of capillary foams made with partially hydrophobized silica particles (50% and 36% SiOH) was investigated at various pH but fixed total ionic strength (10 mM). As we can see from Figure 4-5, the foam height is relatively higher at low and neutral pH, but is significantly suppressed at high pH. This can be explained by the fact that silica particles are more charged at high pH, thus the particle adsorption barrier is higher, which is confirmed by the zeta potential determination (Figure 4-4).

Figure 4-5 Initial foam height (mm) of capillary foams made with partially hydrophobized silica particles (50% and 36% SiOH) at various pH (adjusted by HCl or NaOH). The ionic strength was 10 mM (controlled by NaCl) and the shear speed scale was 6. The green box denotes the capillary foam phase.

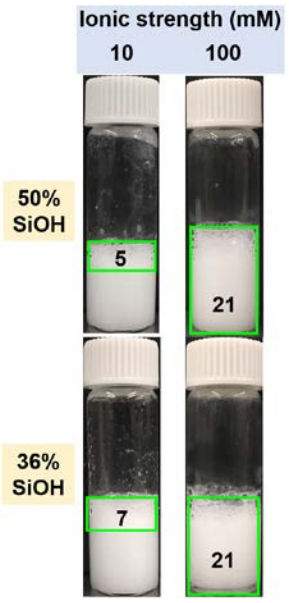

Figure 4-6 Initial foam height (mm) of capillary foams made with partially hydrophobized silica particles (50% and 36% SiOH) with various ionic strength. pH was 10 and the shear speed scale was 6. The green box denotes the capillary foam phase.

After we have demonstrated that foamability is suppressed at high pH due to higher surface charge, we are also interested to find out whether this effect can be counteracted. We added more salt to screen the charge, and better foamability is observed as expected (Figure 4-6). When pH is 10 and ionic strength increases to 100 mM, zeta potential changes to -21.5 mV and foam height increases to 21 mm for 50% SiOH silica particle; zeta potential changes to -20.9 mV and foam height increases to 21 mm for 36% SiOH silica particle.

4.3.3 Effect of Frothing Speed

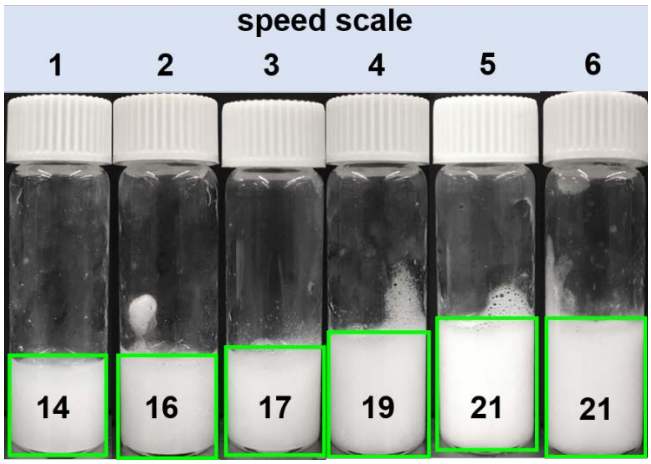

Figure 4-7 Foam height (mm) versus speed for capillary foams made with 50% SiOH silica particles at neutral pH and 50 mM ionic strength. pH and ionic strength were controlled using KH2PO4/K2HPO4 buffer. The speed scale 1 to 6 denotes actual rates of 8,000 rpm, 9,500 rpm, 11,500 rpm, 14,500 rpm, 20,500 rpm and 30,000 rpm, respectively.

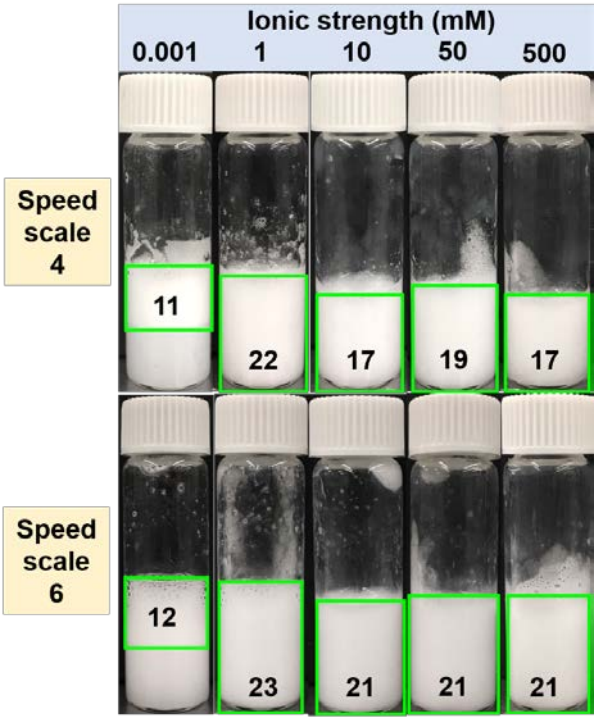

Figure 4-8 Foam height (mm) versus ionic strength for capillary foams made with 50% SiOH silica particles at neutral pH. pH and ionic strength were controlled using KH2PO4/K2HPO4 buffer. The speed scale 4 and 6 denote the actual rate of 14,500 rpm, and 30,000 rpm, respectively.

If the low foamability at high pH and low screening is indeed related to an (electrostatic) adsorption barrier, then it should be possible to improve foamability by introducing more mechanical energy to help particles overcome the barrier. We therefore made some capillary foams with partially hydrophobized silica particles (50% SiOH) at 50 mM ionic strength but different frothing speeds (as shown in Figure 4-7), and compared the impact of ionic strength at two different frothing speeds (as shown in Figure 4-8). It is clear that the initial foam height increases significantly with the increase of frothing speed.

It should be mentioned that both increasing shear rate and ionic strength can boost foam height (as shown in Figure 4-1, Figure 4-7 and Figure 4-8), but the underlying mechanisms are slightly different. We know both the silica particle and oil droplet surfaces are negatively charged in the aqueous phase when pH is above 4, and this same charge imposes a noticeable energy barrier for the particles to overcome prior to adsorption.[6] Increasing shear speed does not change the height of this barrier but provides more energy for the particles to overcome it, while increasing salt concentration can significantly lower the height of the energy barrier, as shown in the following section.

4.3.4 Calculation of Particle Adsorption Energy Barrier at the Oil-Water Interface

The interaction between the silica particle and the TMPTMA-water interface can be calculated based on the extended DLVO (Derjaguin, Landau, Vervey, and Overbeek) theory. The particle adsorption energy barrier results from the joint contributions of van der Waals, electric double layer, and image force interactions.

The van der Waals interaction between a spherical particle and a flat interface is given by Equation 4-2.[11]

$$U_{vdw} = -H_{owp}\frac{r}{6h}, \tag{4-2}$$

where H_{owp} is the nonretarded Hamaker constant (calculated to be 1.30×10^{-21} J) obtained by the mixing rule

$$H_{owp} = (\sqrt{H_{oo}} - \sqrt{H_{ww}})(\sqrt{H_{pp}} - \sqrt{H_{ww}}), \quad (4\text{-}3)$$

and where r is the particle radius and h is the separation distance. H_{oo}, H_{ww} and H_{pp} are the Hamaker constants from the exact Lifshiftz theory results for the symmetric interaction of TMPTMA (estimated from the value of polymethyl methacrylate), water, and silica across vacuum.[12-13]

The electrostatic double layer (EDL) energy of interaction between the particle and the interface was calculated as[12]

$$U_{EDL} = 64\pi\varepsilon_0\varepsilon_r r(\frac{k_B T}{ze})^2 \tanh(\frac{ze\psi_p}{4k_B T}) \tanh(\frac{ze\psi_o}{4k_B T}) \exp(-\kappa h) \quad (4\text{-}4)$$

where ε_0 is the dielectric permittivity of the vacuum, ε_r is the relative dielectric constant of water, k_B is Boltzmann constant, T is temperature, z is the ion valence (1 for NaCl solution), e is the elementary charge, κ^{-1} is the Debye length , ψ_p is the particle surface potential (taken as the determined zeta potential), and ψ_o is the surface potential of the oil-water interface, which is estimated from literature values for the xylene-water interface.[5] Equation 4-4 is based on a linear superposition of the Gouy-Chapman solutions for the electrostatic potential near flat charged surfaces and implements the Derjaguin approximation to account for the particle curvature, against which the curvature of the fluid-fluid interface is neglected.

It is well-known that a charged particle near an interface with discontinuity of dielectric permittivity experiences a force pointing towards the more polarizable medium.[12] The magnitude of the "image charge" is given by

$$q_{image} = q\frac{\varepsilon_1 - \varepsilon_2}{\varepsilon_1 + \varepsilon_2}, \tag{4-5}$$

where ε_1 is the dielectric constant of the medium where the particle is located, and ε_2 is the dielectric constant of the particle-free medium. The interaction between two spherical particles is given by[12]

$$U_{image} = 32\pi\varepsilon_0\varepsilon_r r(\frac{k_B T}{ze})^2 \tanh(\frac{ze\psi_p}{4k_B T})\tanh(\frac{ze\psi_i}{4k_B T})\exp(-2\kappa h), \tag{4-6}$$

where ψ_i, the surface potential of the image charge, is given by Equation 4-7.[12]

$$\psi_i = \frac{2k_B T}{e}\sinh^{-1}[\frac{\varepsilon_w - \varepsilon_o}{\varepsilon_w + \varepsilon_o}\sinh(\frac{e\psi_p}{2k_B T})] \tag{4-7}$$

In Equation 4-7, ε_w is the dielectric constant of water and ε_o is the dielectric constant of TMPTMA (estimated from the value of butyl methacrylate[14]).

The total interaction is the sum of Van der Waals interaction, electrostatic double layer interaction and image force interaction. Figure 4-9 shows the interaction profile at different ionic strengths. The particle adsorption energy barrier significantly exceeds the energy of regular thermal flocculation, thus substantial additional energy input (such as the

mechanical energy of mixing) is required for the particles to overcome this barrier and reach the interface. It is clear that when ionic strength is 1 mM, the barrier has been significantly lowered compared with 0.001 mM, thus it becomes relatively easier for the particles to reach the interface, which is consistent with the dramatic increase of foam height as shown in Figure 4-1. Although higher ionic strength (above 1 mM) can further reduce the adsorption energy barrier, the particle surface actually becomes more and more hydrophobic (Figure 4-3), thus better foamability is not observed (Figure 4-1) beyond the initial increase between 0.001 mM and 1 mM. In other words, there exists an optimal ionic strength corresponding to the optimal foamability for partially hydrophobic silica particles.

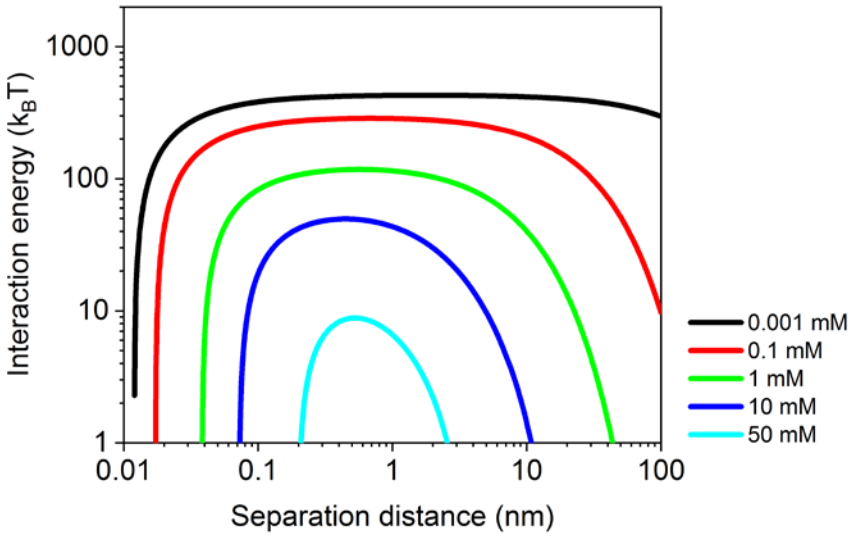

Figure 4-9 Calculated extended DLVO interaction energy profiles between the 50% SiOH silica particle and the TMPTMA-water interface.

One may argue that in a system subject to a large input of irreversible mechanical work (i.e., homogenization) system, the balance of interaction forces is more relevant than

the balance of interaction energies. Theoretically, the formation of a capillary foam must meet the requirement that the maximum repulsive force between the particle and the interface must be overcome by the hydrodynamic force pushing the particle toward the interface[15]:

$$\max(F_{vdw} + F_{EDL} + F_{img}) > F_{mix}, \tag{4-8}$$

where F_{vdw}, F_{EDL}, F_{img} and F_{mix} are the Van der Waals force, electrostatic double layer force, image force and the mechanical mixing force, respectively, and they are calculated in the same manner as in our previous work.[16] The force profile between 50% SiOH silica particle and the TMPTMA-water interface at different ionic strengths is shown in Figure 4-10. It is interesting that for some intermediate ionic strengths, the overall interaction force between the particle and the interface has a maximum value, but it is on the same order of magnitude as the mixing force; for extremely low or extremely high ionic strength, there is no such maximum and the overall interaction force is always smaller than the mixing force. This observation explains why capillary foam can be successfully made at all these conditions (as shown in Figure 4-1c). It is worth noting that the calculation of each single component in the overall interaction force typically contains significant uncertainty, thus the sum of the three large numbers also contains significant uncertainty that is difficult to estimate. Therefore, one should not take it for granted that $F/F_{mix} > 1$ indicates no capillary foam can be created.

4.3.5 Relation between Foamability and Stability

Both foamability and stability are important criteria to describe foam properties, but there has been no systematic study elucidating the relationship between them. Although the main topic of this paper is foamability, we were also interested to evaluate the long-term stability of capillary foams. Capillary foams stabilized by partially hydrophobized silica particles (50% and 36% SiOH) at neutral pH but various ionic strengths (adjusted by the buffer ingredients) for a period of up to seven days are shown in Figure 4-11 and Figure 4-12 in the supporting information. It is observed that at low ionic strength (less than 10 mM), the foamability is good, but the long-term foam stability is poor. This result indicates that good foamability does not necessarily lead to good foam stability. To identify a more general and universal relation between foamability and stability, more future studies will be required.

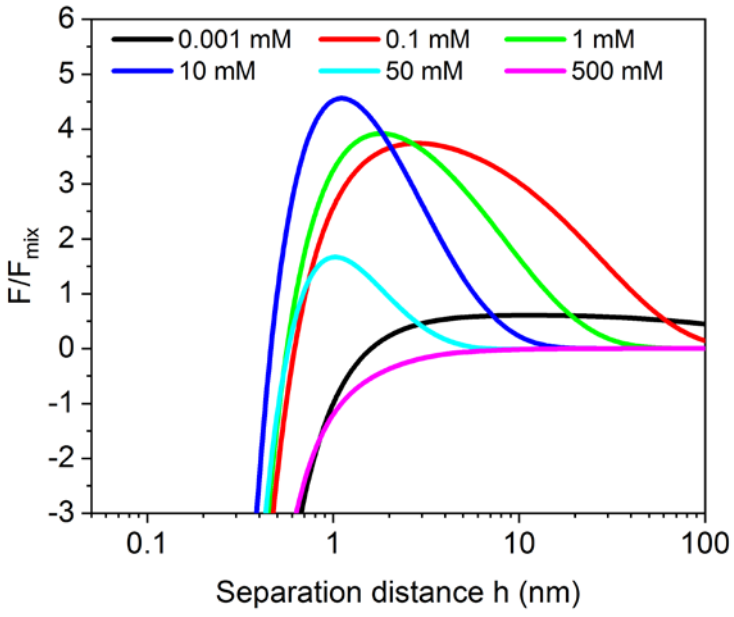

Figure 4-10 Calculated force profile between 50% SiOH silica particle and the TMPTMA-water interface. F is the total interaction force, and F_{mix} is the mechanical mixing force.

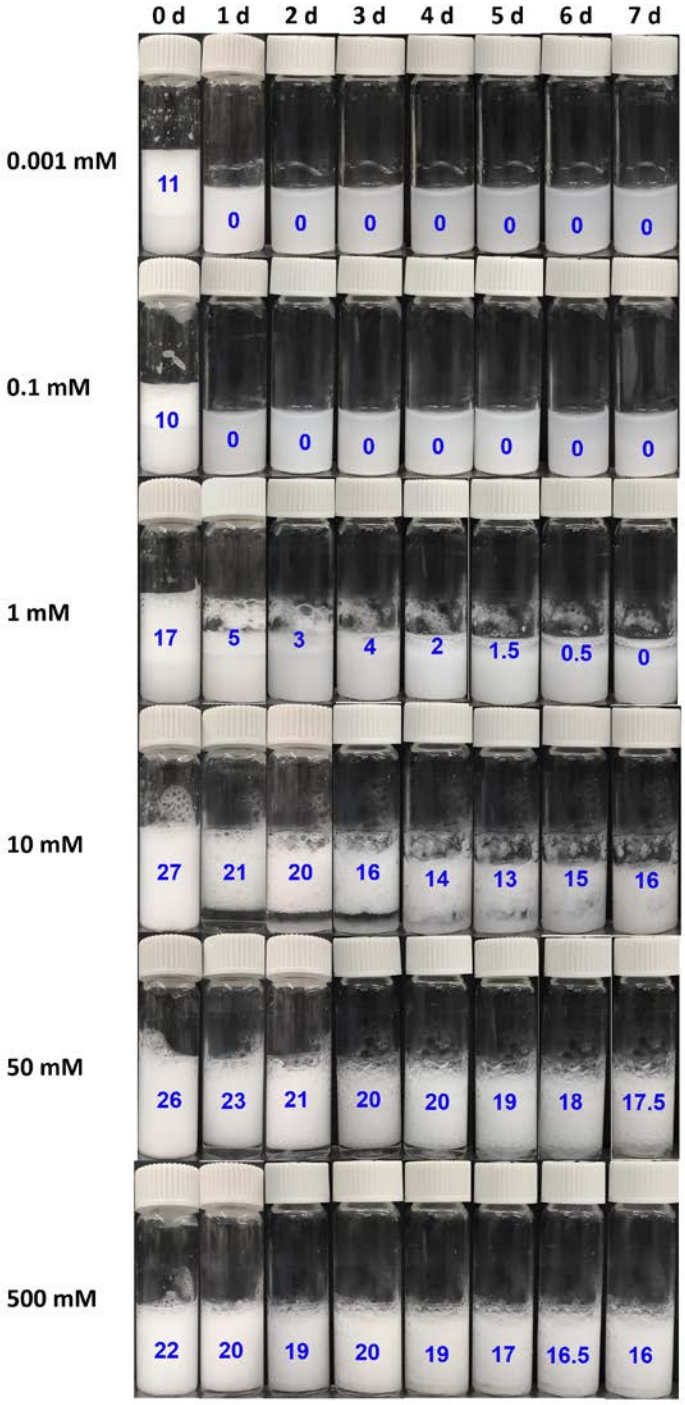

Figure 4-11 Foam height (mm) over time of capillary foams made with partially hydrophobized silica particles (50% SiOH) at natural pH but with various ionic strength. pH and ionic strength were controlled using KH_2PO_4/K_2HPO_4 buffer. The blue numbers in the figure denote the height of the capillary foam.

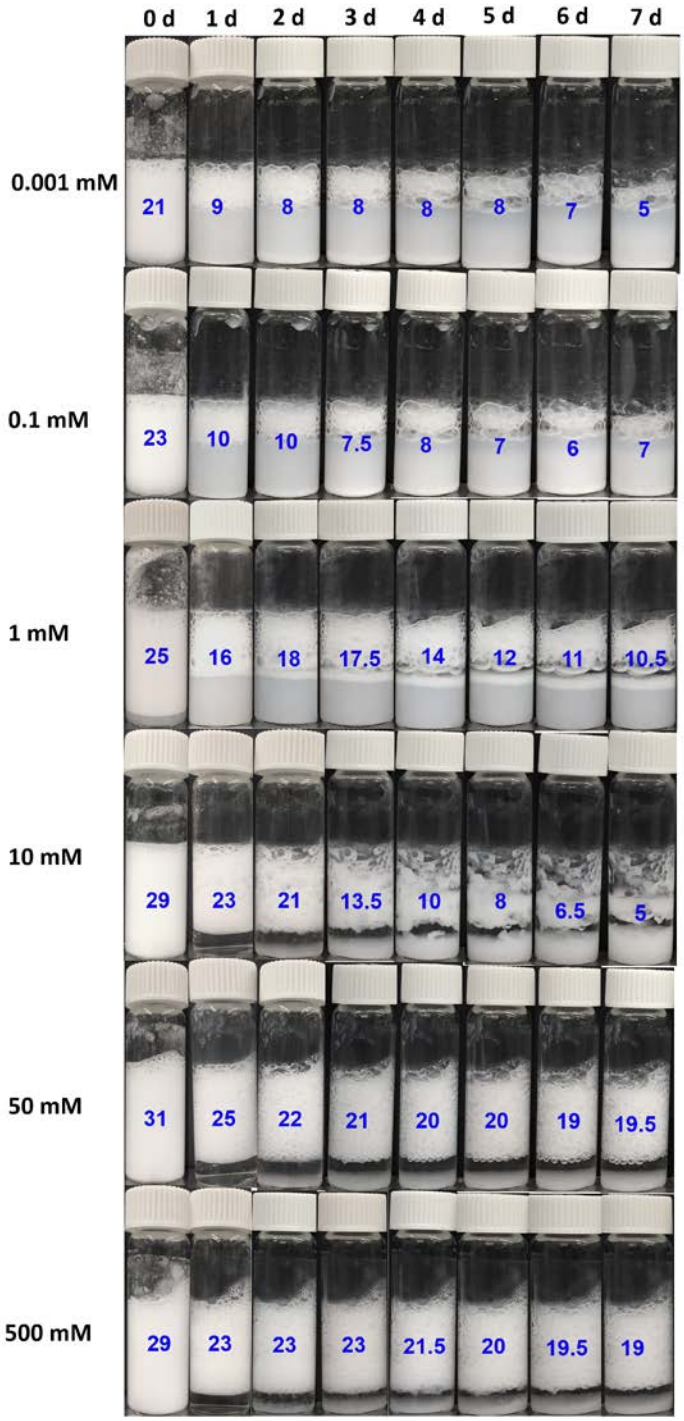

Figure 4-12 Foam height (mm) over time of capillary foams made with partially hydrophobized silica particles (36% SiOH) at natural pH but with various ionic strength. pH and ionic strength were controlled using KH_2PO_4/K_2HPO_4 buffer. The blue numbers in the figure denote the height of the capillary foam.

4.4 Conclusions

In this work, the foamability of capillary foams made with partially hydrophobized silica particles was investigated systematically. We find that particles need to have beneficial wetting at the oil-water interface in order to achieve good foamability, and the foamability is further impacted by the ionic strength. There exists an optimal ionic strength corresponding to the optimal foamability, below which the kinetic adsorption barrier is too high for the particles to overcome, above which the particle wetting is no longer beneficial because the silica particle becomes too hydrophobic. Increasing the homogenization intensity during frothing can also enhance the foamability by providing more energy for particles to overcome the adsorption energy barrier. We have also confirmed that silica particles are less charged at low pH, and a lower particle adsorption barrier and better foamability are therefore observed. We expect that the option to enhance foamability by adjusting the effective particle surface charge will prove useful in the design of new foam-based materials (e.g., personal care products, food and beverages) and the operation of foam-related processes (*e.g.*, washing, firefighting).

4.5 References

[1] Zhang, Y.; Wang, S. C.; Zhou, J. R.; Benz, G.; Tcheimou, S.; Zhao, R. Y.; Behrens, S. H.; Meredith, J. C. Capillary foams: Formation stages and effects of system parameters. *Ind. Eng. Chem. Res.* **2017,** *56* (34), 9533-9540.

[2] Yang, H.; Shin, K.; Tae, G.; Satija, S. K. Structure of a monolayer of poly(ethylene glycol) end-capped with a fluoroalkyl group and its relationship with protein adsorption at the aqueous interface. *Soft Matter* **2009,** *5* (14), 2731-2737.

[3] Pieranski, P. Two-dimensional interfacial colloidal crystals. *Phys. Rev. Lett.* **1980,** *45* (7), 569-572.

[4] Binks, B. P.; Lumsdon, S. O. Influence of particle wettability on the type and stability of surfactant-free emulsions. *Langmuir* **2000,** *16* (23), 8622-8631.

[5] Marinova, K. G.; Alargova, R. G.; Denkov, N. D.; Velev, O. D.; Petsev, D. N.; Ivanov, I. B.; Borwankar, R. P. Charging of oil-water interfaces due to spontaneous adsorption of hydroxyl ions. *Langmuir* **1996,** *12* (8), 2045-2051.

[6] Behrens, S. H.; Grier, D. G. The charge of glass and silica surfaces. *J. Chem. Phys.* **2001,** *115* (14), 6716-6721.

[7] Dugyala, V. R.; Muthukuru, J. S.; Mani, E.; Basavaraj, M. G. Role of electrostatic interactions in the adsorption kinetics of nanoparticles at fluid-fluid interfaces. *PCCP* **2016,** *18* (7), 5499-5508.

[8] Kostakis, T.; Ettelaie, R.; Murray, B. S. Effect of high salt concentrations on the stabilization of bubbles by silica particles. *Langmuir* **2006,** *22* (3), 1273-1280.

[9] Simovic, S.; Prestidge, C. A. Adsorption of hydrophobic silica nanoparticles at the pdms droplet-water interface. *Langmuir* **2003,** *19* (20), 8364-8370.

[10] Simovic, S.; Prestidge, C. A. Hydrophilic silica nanoparticles at the pdms droplet-water interface. *Langmuir* **2003,** *19* (9), 3785-3792.

[11] Bhattacharjee, S.; Elimelech, M. Surface element integration: A novel technique for evaluation of dlvo interaction between a particle and a flat plate. *J. Colloid Interface Sci.* **1997,** *193* (2), 273-285.

[12] Israelachvili, J. Intermolecular and surface forces. Elsevier: Amsterdam, 2011.

[13] Feldman, K.; Tervoort, T.; Smith, P.; Spencer, N. D. Toward a force spectroscopy of polymer surfaces. *Langmuir* **1998,** *14* (2), 372-378.

[14] Christian, W. *Static dielectric constants of pure liquids and binary liquid mixtures*; Springer2008.

[15] Tcholakova, S.; Denkov, N. D.; Lips, A. Comparison of solid particles, globular proteins and surfactants as emulsifiers. *PCCP* **2008,** *10* (12), 1608-1627.

[16] Wang, H.; Singh, V.; Behrens, S. H. Image charge effects on the formation of pickering emulsions. *J. Phys. Chem. Lett.* **2012,** *3* (20), 2986-2990.

CHAPTER 5. OIL-COATED BUBBLE FLOTATION FOR SEPARATING HYDROPHILIC INK PARTICLES

5.1 Introduction

In previous chapters, we have discussed some fundamental aspects (thermodynamics, kinetics and hydrodynamics) of oil-coated bubble flotation, showing its potential advantages over the traditional froth flotation. We have also talked about the capillary foam system, which can be used as a convenient method to evaluate the particle floatability (the ability to be collected and removed by gas bubbles). For instance, it is reasonable to predict that partially-hydrophobized silica particles have better floatability than hydrophilic silica particles, based on their better ability to create capillary foams.

We now want to work on some applied, industrially-relevant separation systems to examine the performance of oil-coated bubble flotation. Flotation de-inking is such an application where the newer type of hydrophilic ink particles are difficult to separate with conventional technology. Inspired by the use of oil as collectors in mining operation, oil-assisted flotation de-inking has been initiated in the past few decades. Pelton et al.[1-2] found that air bubbles coated with silicone oil can enhance deinking performance in the 1990s, and Gomez et al.[3] further investigated an aerosol enhanced deinking process using oil-coated bubbles in 2001. However, these efforts received very little attention (only 2 citations in the last 10 years), and the underlying de-inking mechanism and the impact of each individual system parameter were not fully understood.

The objective of this chapter is to systematically evaluate the possibility of applying oil-coated bubbles to ink removal and to better understand the de-inking mechanism. We started with some miniaturized de-inking tests by adopting similar frothing protocol when we created capillary foams, to evaluate the impact of each individual system parameter efficiently. We also built a lab-scale flotation de-inking column and made some paper pads from recycled office paper. Improvement in paper brightness and effective residual ink concentration (ERIC) demonstrated the feasibility of oil-coated bubble de-inking. We believe the hydrophilic ink particle can serve as a model particle to demonstrate the broader applications of oil-coated bubble flotation for separating other mildly hydrophilic particles.

5.2 Experimental Section

5.2.1 Materials

The hydrophilic ink (HPI-4060D) was purchased from InkTec Co., Ltd. Ink particle size and zeta potential were determined using a Malvern Zetasizer Nano ZS90. Silicone oil, decane, hexadecane, paraffin oil, $NaClO_4$, and NH_4Cl were purchased from Sigma-Aldrich. NaCl and $CaCl_2$ were purchased from Honeywell Fluka. $MgCl_2 \cdot 6H_2O$, HCl and NaOH were purchased from EMD Chemicals Inc. Oleic acid was purchased from ICN Biomedicals Inc. H_2O_2 was purchased from BDH Chemicals. $Na_2SiO_3 \cdot 5H_2O$ was purchased from Fisher Scientific. 1-octanol was purchased from Tokyo Chemical Industry Co., Ltd. All chemicals were used as received.

5.2.2 Miniaturized De-Inking Test

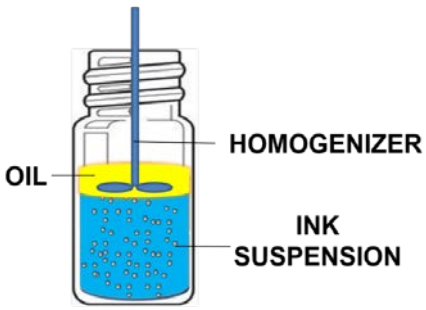

Figure 5-1 Diagram of the miniaturized de-inking test.

To evaluate the de-inking performance under different conditions more efficiently, we designed and carried out the miniaturized de-inking test (as shown in Figure 5-1). An ink particle suspension in water containing certain amount of particles (adding 6 μL concentrated ink suspension into 10 mL DI water) was first prepared in a 20 mL glass vial. Different salt was then added and pH was adjusted. A small amount of immiscible oil (0.5 mL) was added into the vial subsequently. Finally, the mixture was mechanically frothed using a rotor-stator homogenizer (IKA Ultra-Turrax T10, stator diameter of 8 mm and rotor diameter of 6.1 mm) at 30,000 rpm for 3 min (with a 20 s pause between each minute). To ensure consistent results, the rotor and stator of the homogenizer were always immersed at the same depth (5 mm) into the bulk aqueous phase when the homogenization just started, although it did not have a noticeable impact on the test because the turbulence was so strong. The treated sample was then analyzed using a UV-vis spectrophotometer (Shimadzu UV-1800) to determine the residual ink concentration. The absorbance at 300

nm wavelength and the actual ink concentration were correlated based on Beer-Lambert Law. The ink particle removal efficiency was calculated as the following:

$$\text{Efficiency}\ (\%) = \frac{\text{initial ink (ppm)} - \text{remaining ink (ppm)}}{\text{initial ink (ppm)}} \times 100\ \%. \qquad (5\text{-}1)$$

5.2.3 Lab-scale De-Inking Test

Figure 5-2 shows the diagram of the lab-scale de-inking test apparatus, which is similar to the experimental set up designed by Chen et al.[4] It consists of a nebulizer (Shenzhen Fitconn Technology Co., Ltd.), a gas flowmeter (Cole-Parmer Instrument Company, LLC.) and a Denver D12 Laboratory Flotation Machine (Metso Co. Inc.). Oil is added into the nebulizer and is transformed into oil mist. Additional compressed air is added to the oil mist to ensure the same gas flow (~ 15 L/min) both in the presence and absence of oil mist.

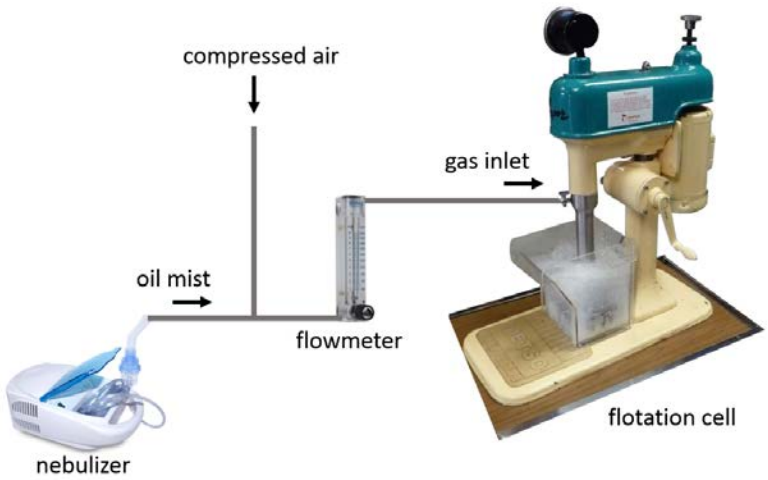

Figure 5-2 Diagram of lab-scale de-inking test.

The lab-scale de-inking test was performed following a standard procedure (Method 11: Assessment of Print Product Recyclability – Deinkability Test) suggested by International Association of the Deinking Industry (INGEDE) (as shown in Figure 5-3).[5] The INGEDE standard printing pattern for de-inking test was first printed on some newsprint paper (ISO brightness 49.20 % ± 0.11 %) using the hydrophilic inkjet ink (InkTec HPI-4060D) and a HP DESKJET 100 printer. Then the paper was shredded into small pieces and was dried in the oven. A certain amount of oven-dried recycled paper (200.00 g) was mixed with 400.00 g de-inking solution (containing 1.20 g NaOH, 1.60 g oleic acid and 6.26 g $Na_2SiO_3 \cdot 5H_2O$) and 630 g hard water (containing 0.30 g $CaCl_2 \cdot 2H_2O$). The mixture was pulped using a food mixer (KitchenAid Artisan KSM150PSER 5) in 45 ℃ water bath for 2 min, followed by another 18 min after 100.00 g deionized water and 1.40 g H_2O_2 were added. After pulping, the mixture was conditioned: 302.70 g pulp mixed with 600 mL hard water (containing 0.28 g $CaCl_2 \cdot 2H_2O$) was conditioned in 45 ℃ hot water bath for 60 min. Subsequently, the conditioned pulp was mixed with 4.5 L hard water (containing 2.12 g $CaCl_2 \cdot 2H_2O$). Finally, flotation was performed in the flotation machine. Oil-coated bubble flotation was performed in a similar fashion except that oil mist was introduced into the system. After flotation, paper pads were made by filtering the de-inked pulp and were air-dried for at least 24 h. The ISO paper brightness and ERIC were measured using the ColorTouch 2 instrument (Technidyne Co. Inc.).

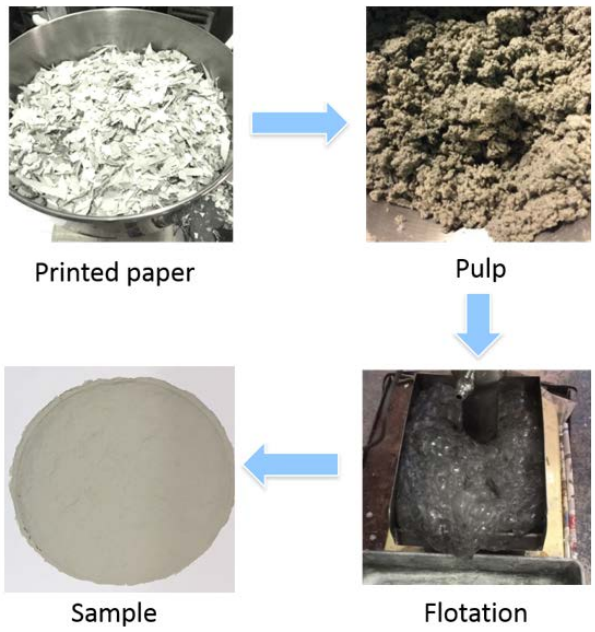

Figure 5-3 Procedure of lab scale de-inking test.

5.3 Results and Discussion

5.3.1 Miniaturized De-inking Test

5.3.1.1 Effect of Oil Type

There are several important system parameters involved in the oil-coated bubble de-inking, such as oil type, salt type, salt concentration and pH. To evaluate the impact of each individual parameter more efficiently, we designed a miniaturized de-inking test performed by mechanically frothing a mixture of particles, water and oil in a small vial (Figure 5-1). Our recent studies suggest that in such a homogenized system, air bubbles are introduced into the bulk aqueous phase and the small amount of oil supplied can wrap

around them to form oil-coated bubbles (either partially coated or completely coated, depending on the spreading coefficient of the oil).[6-8] It is reasonable to argue that the miniaturized de-inking test serves as a very convenient and efficient screening method for larger scale flotation de-inking test that uses either uncoated or oil-coated gas bubbles, in the sense of being able to create sufficient air-water or oil-water interfaces that allow for particle adsorption.

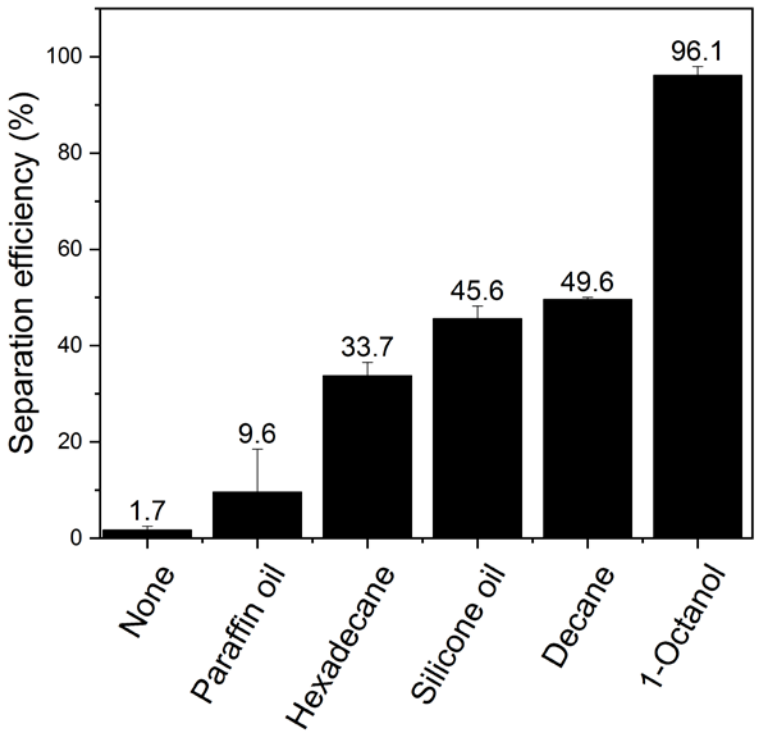

Figure 5-4 Effect of oil type on the ink particle separation efficiency. NaCl concentration is 50 mM and pH is neutral.

The effect of oil type on the ink particle removal efficiency is shown in Figure 5-4. In the presence of a small amount of oil, the ink separation efficiency is significantly enhanced. It is interesting that there is noticeable difference using different types of oils,

arguably resulting from the variance of interactions between the oil and the hydrophilic ink particles. One possible reason can be related to the oil polarity. Being the most polar oil among all that we have tested (as indicated by the literature value of relative permeability shown in Table 5-1), 1-octanol has a more dominant "hydrophilic" part compared to the "hydrophobic" part and has a strong interaction with the hydrophilic ink, therefore giving the highest ink removal efficiency of 96.1 % ± 1.9 %. The other four types of oil share similar relative permeability, but still display different ink particle removal behavior. It is possible that the oils we use are of different grades from the oils reported in the literature (especially for paraffin oil and silicone oil) and can have different dielectric constants, therefore the order of performance is different from what we expected.

Table 5-1 Relative permeability (dielectric constant) of oils used in the miniaturized de-inking test. Measurement uncertainty was not reported in the literatures.

Oil	Paraffin oil	Hexadecane	Silicone oil	Decane	1-Octanol
Relative permeability ε_r (10^{-12})	2.2[9]	2.0[10]	2.2– 2.8[9]	2.0[11]	10.3[12]

5.3.1.2 Effect of Salt Type

The impact of salt type on the ink particle removal efficiency in the presence and absence of decane is shown in Figure 5-5. Decane is used because it exhibits intermediate ink removal performance compared with other oils (as shown in Figure 5-4), therefore it can better reveal the different de-inking abilities of various types of salts. It is obvious that

even at the same ionic strength, there is significant variance between different salts, with divalent salts performing better than monovalent salts. This can be explained by their different ability to screen particle surface charge and promote particle aggregation. Figure 5-6 shows the change of particle size over time in the presence of different salts, and Figure 5-7 shows the zeta potential of ink particle at different conditions. It is worth noting that dynamic light scattering (DLS) determination is known to be less accurate for particles larger than 1 μm, but it still gives valuable insights that $CaCl_2$ and $MgCl_2$ enhance the aggregation and agglomeration of the ink particles more efficiently compared with other salts, therefore promoting the removal of ink particles by rising gas bubbles. These observations are consistent with the well-known Schulze-Hardy Rule: multivalent counter ions destabilize colloidal suspensions much more effectively than monovalent counter ions.[13-14]

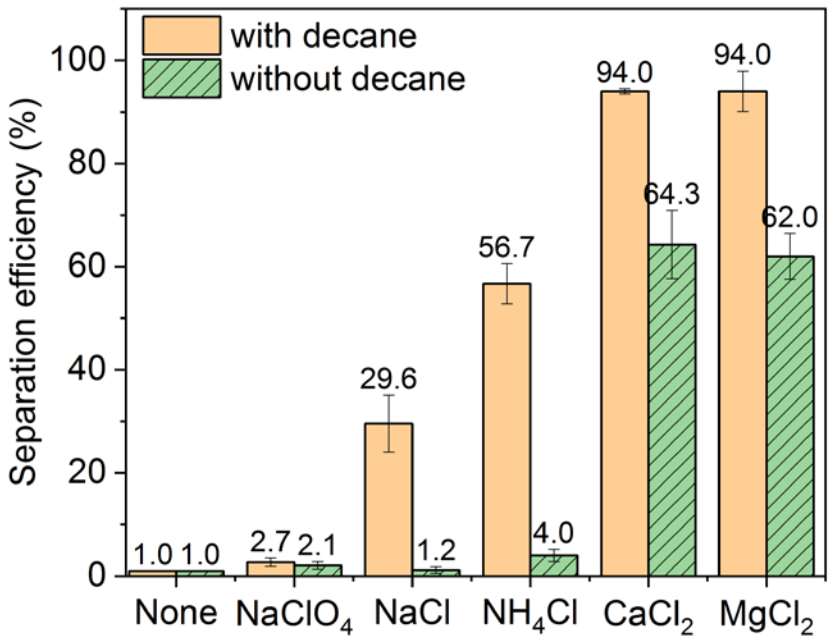

Figure 5-5 Effect of salt type on the ink particle removal efficiency. Ionic strength is 30 mM and pH is neutral.

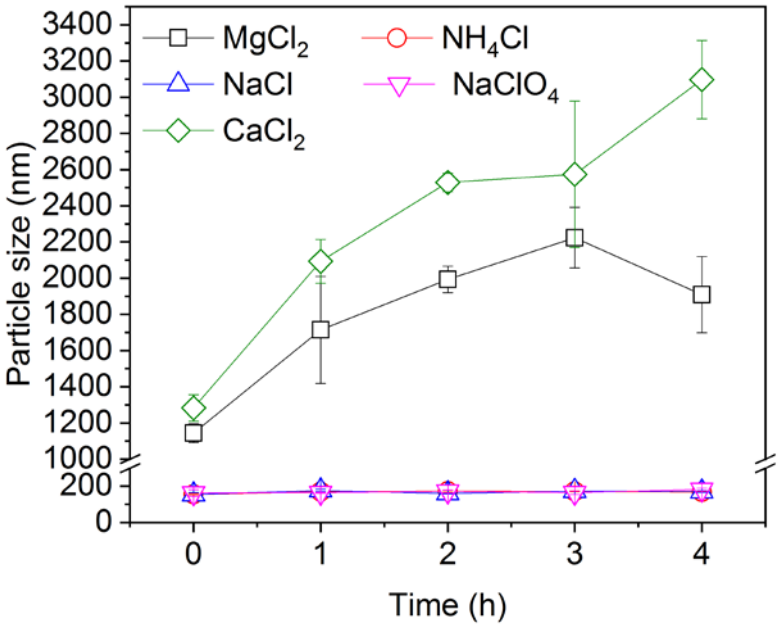

Figure 5-6 Ink particle size over time in the presence of different salts. Ionic strength is 30 mM and pH is neutral.

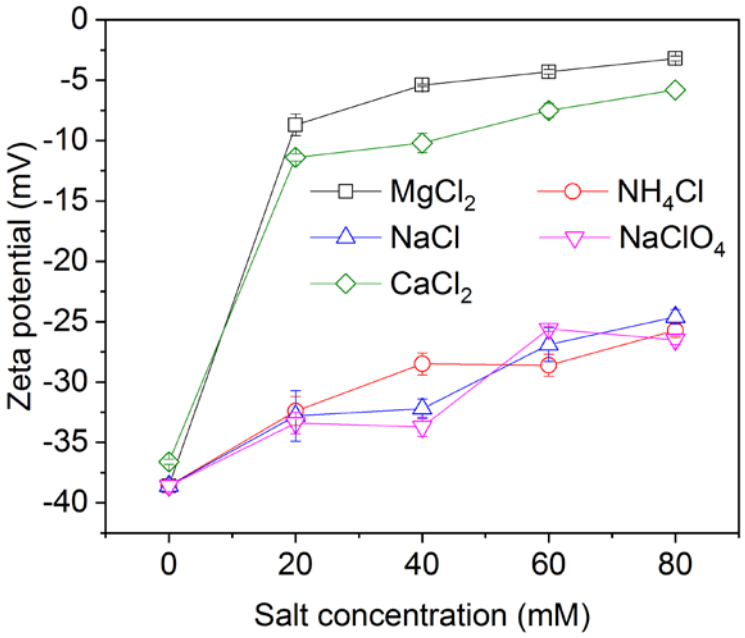

Figure 5-7 Ink particle zeta potential versus salt concentration at neutral pH.

5.3.1.3 Effect of Salt Concentration

The impact of salt concentration on ink particle removal efficiency is shown in Figure 5-8, and the impact on particle zeta potential and particle size are shown in Figure 5-7 and Figure 5-9, respectively. It is clear that in the absence of decane, increasing salt concentration does help screen the surface charge of ink particles (Figure 5-7), but hydrophilic ink particles do not have good affinity for the air-water interface and will largely remain in the aqueous phase (Figure 5-8). On the contrary, in the presence of decane the additional salt is also expected to screen particle surface charge, but the ink particles have better affinity towards the oil-water interface. The affinity provides a driving force for particle adsorption onto the oil-water interface of the bubble and the charge screening lowers the electrostatic repulsive barriers.

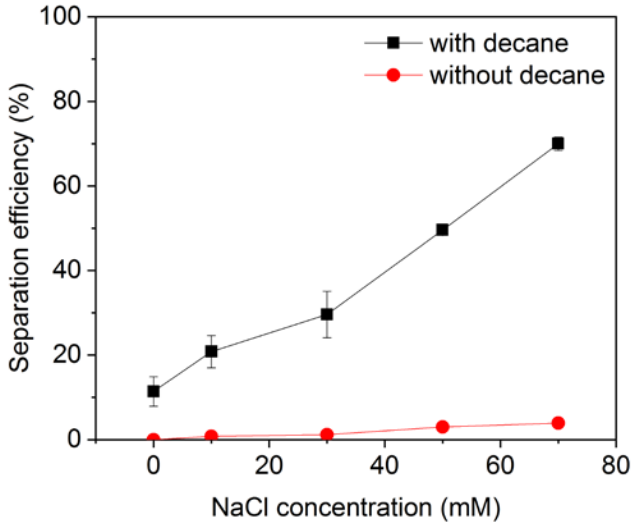

Figure 5-8 Ink particle separation efficiency at different NaCl concentration. pH is neutral.

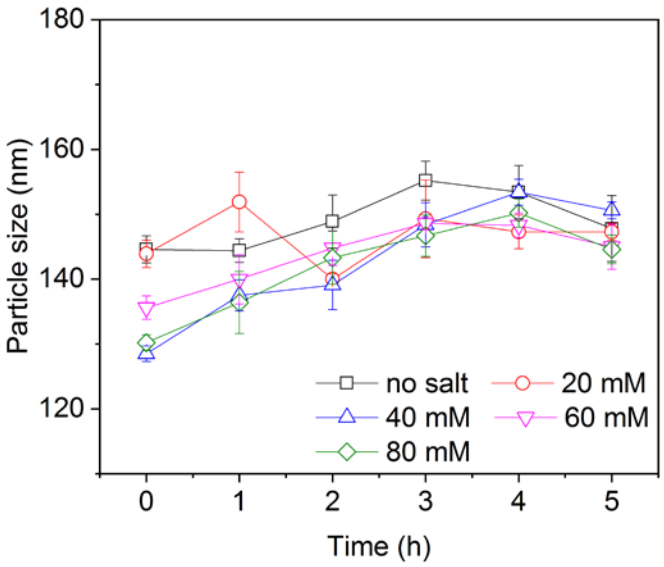

Figure 5-9 Ink particle size as a function of time in aqueous dispersions of different NaCl concentrations. The pH is neutral. The dispersion is prepared by diluting 6 µL original concentrated ink with 100 mL deionized water.

5.3.1.4 Effect of pH

Figure 5-10 shows the impact of pH on the ink particle removal efficiency both in the absence and presence of decane. It is obvious that lower pH enhances the removal of ink particles from water, regardless of oil. This is consistent with the particle zeta potential and particle size results shown in Figure 5-11 and Figure 5-12. Namely, less surface charges leads to lower particle adsorption energy barrier, therefore ink particles adsorb more readily at the air-water or oil-water interface associated with bubbles. The specific type of hydrophilic ink particles used has an isoelectric point around pH 3. With increasing negative charge developed above this pH, it becomes more difficult for the particles to form large aggregates, and the particle adsorption barrier near the interface is also increased; therefore, the ink removal efficiency is lower.

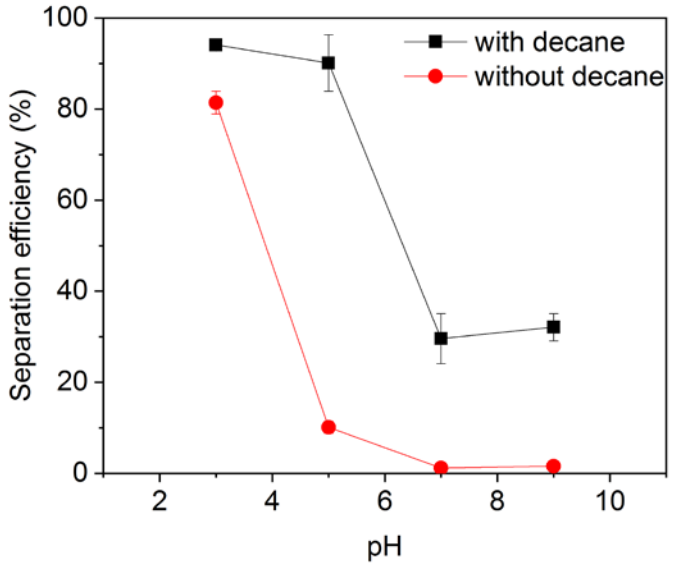

Figure 5-10 Ink particle separation efficiency as a function of pH in the presence of 30 mM NaCl.

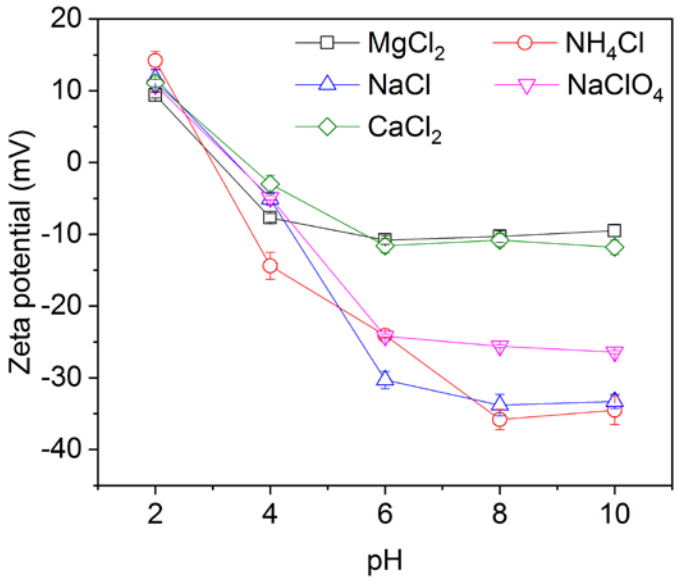

Figure 5-11 Ink particle zeta potential versus pH. Ionic strength is 30 mM.

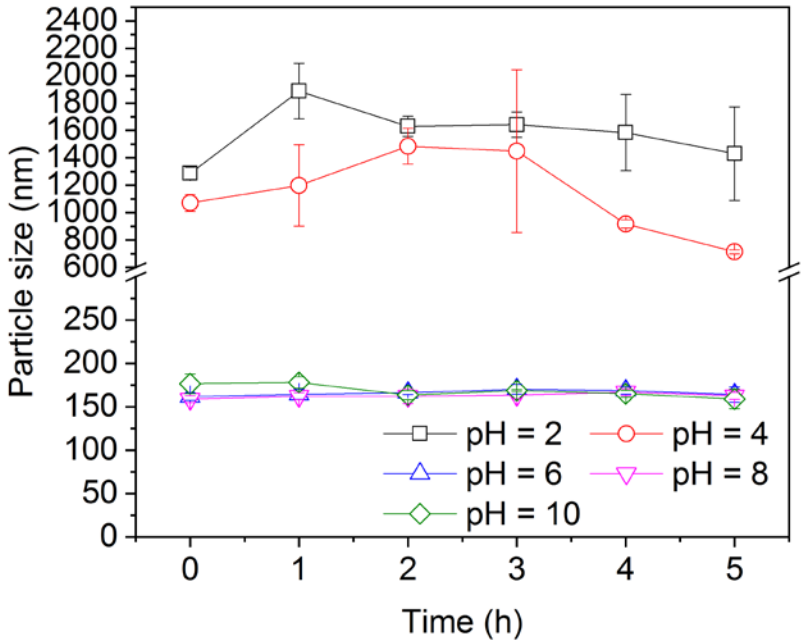

Figure 5-12 Ink particle size over time at different pH in the presence of 30 mM NaCl.

5.3.2 Lab-scale De-Inking Test

Based on the above results from the miniaturized de-inking tests to evaluate the impact of individual system parameters, we conducted lab-scale de-inking tests. Figure 5-13 shows a qualitative comparison between conventional flotation de-inking and decane-assisted flotation de-inking. When the gas flow containing decane mist was fed, the de-inking performance is significantly improved, which is consistent with the previous results of miniaturized de-inking tests.

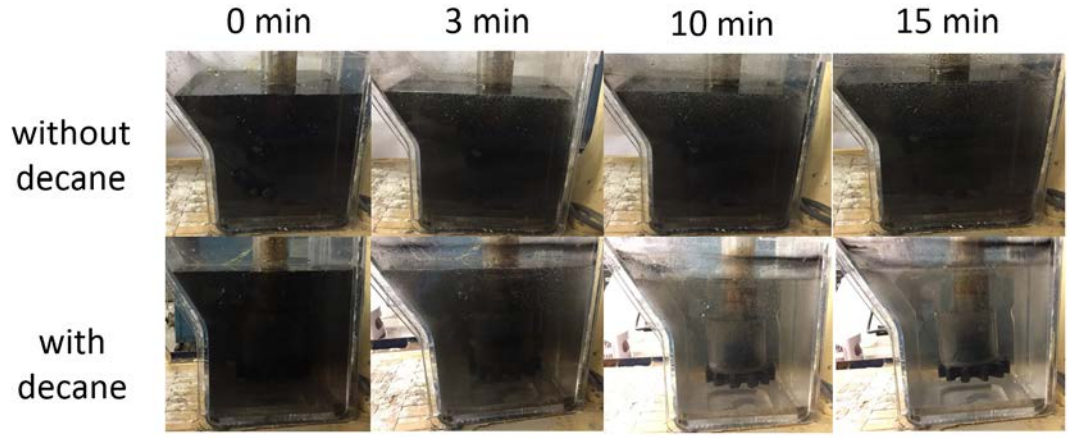

Figure 5-13 Comparison of lab-scale de-inking using conventional flotation and decane-assisted flotation. There is 10 mM $MgCl_2$ in both cases and pH is neutral.

We also followed the standard practice to make some paper pads from recycled papers. The detailed pulping and de-inking procedures are presented in the Experimental Section. Figure 5-14 shows the comparison of brightness and ERIC of paper pads following different de-inking protocols. Scenario B, C and D display significant improvement of paper brightness compared to the paper pad made from the pulp that was not de-inked (scenario A), fully recovering the brightness of the original recycled paper. In scenario C, there was 10 mM $MgCl_2$ added, which was very effective to promote the aggregation of ink particles (as shown in the miniaturized de-inking tests). However, since there is no oil involved, the uncoated bubbles alone are not able to collect those aggregated ink particles; therefore the ERIC value is even higher than that on the paper pad made from the pulp de-inked by uncoated bubbles in the absence of salt. The last scenario D involves both salt and oil, where ink particles aggregate easily and are adsorbed and removed easily, achieving the lowest ERIC value among these four scenarios. In scenario D, both brightness and

ERIC show significant improvement compared to the scenario B using conventional flotation de-inking (with t-test p-values being less than 0.001).

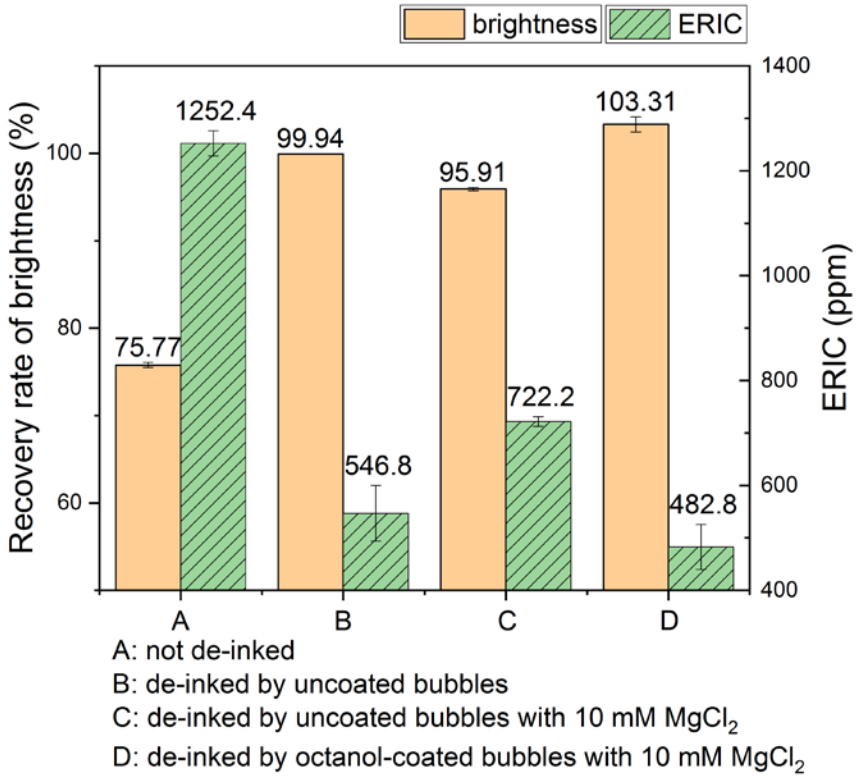

Figure 5-14 Comparison of paper brightness and ERIC of paper pads underwent different de-inking methods.

There can be concerns on the product yield and fiber loss in the flotation de-inking, especially when we introduce oils such as 1-octanol that may have higher affinity for both the hydrophilic ink particles and paper fibers. Our hypothesis is that better paper brightness and lower ERIC value can be achieved, yet not at the cost of losing more fibers. To test this hypothesis, we measured the exact amount of fibers lost in scenarios B and D. In the absence of 1-octanol (groups B1 through B3 in Table 5-2), there are huge amount of foam

created, leading to a significant amount of overflow which entraps paper fibers physically and causes a higher fiber loss. In the presence of 1-octanol (groups D1 through D3 in Table 5-2), however, it is observed that the foamability of the system is slightly suppressed (yet still good enough to maintain a reasonable amount of froth layer that can be skimmed off), therefore less paper fibers are rejected along with the overflow. Based on the results shown here, we believe the concern on fiber loss can be alleviated.

Table 5-2 Comparison of conventional de-inking and oil-assisted de-inking. Group B and D have the same condition as in Figure 5-14, and they are run in triplicates.

Group	Rejected volume (mL)	Rejected fiber (g)	Accepted fiber (g)	Fiber loss (%)	Pad brightness (%)	Pad ERIC (ppm)
B1	1500	14.05	33.40	29.61	50.23 ± 0.38	571.1 ± 15.6
B2	925	11.71	36.09	24.50	48.43 ± 0.52	481.5 ± 26.5
B3	1120	11.20	33.21	25.22	48.87 ± 0.75	587.7 ± 25.4
D1	450	7.59	40.30	15.85	50.33 ± 0.16	526.9 ± 8.2
D2	550	7.46	40.46	15.57	50.85 ± 0.26	498.4 ± 5.6
D3	540	7.12	40.73	14.88	51.26 ± 0.24	429.3 ± 6.4

It is worth noting that the actual de-inking process in the paper recycling industry is much more complicated than the simplified experiments we have presented here. For instance, the detachment of ink particles from paper fibers into water is another essential step, but is out of the scope of our current work. However, this is the first systematic study to evaluate the impact of each individual system parameter of flotation de-inking using

both uncoated and oil-coated bubbles, to the best of our knowledge. Future work will be necessary to help us understand the process more thoroughly in order to apply this method in the larger manufacturing scale.

5.4 Conclusions

In this work, flotation de-inking using both uncoated and oil-coated bubbles was performed with miniaturized homogenized samples and lab-scale flotation de-inking testing. System parameters including oil type, salt type, salt concentration and pH were systematically evaluated. We found that oil-coated bubble flotation often dramatically outperforms the standard technique with uncoated bubbles; the highest ink removal efficiency was observed in systems containing multivalent salts at low pH when using bubbles coated with 1-octanol. This work sheds light on the mechanism of oil-coated bubble flotation in the separation of less hydrophobic or even mildly hydrophilic particles, and is expected to trigger broader interests in many other separation systems.

5.5 References

[1] Beverly Wasmund, R. P. Model deinking studies-carbon black removal by oil-coated plastic beads. *Pulping Conference: Sheration Harboro Island, San Diego, California* **1994**, 1005-1009.

[2] Maiolo, J.; Pelton, R. Aerosol-enhanced flotation - a possible approach to improved flotation deinking. *J. Pulp Pap. Sci.* **1998,** *24* (10), 324-328.

[3] Gomez, C. O.; Acuna, C.; Finch, J. A.; Pelton, R. Aerosol-enhanced flotation deinking of recycled paper - silicone oil offers an effective way of forming a layer on the bubble surface. *Pulp & Paper-Canada* **2001,** *102* (10), 28-30.

[4] Chen, S., Tang, L., Tao, X., He, H., Yang, Z., Chen, L. Exploration on the mechanism of oily-bubble flotation of long-flame coal. *Fuel* **2018,** *216*, 427-435.

[5] Ingede method 11. Available at: https://www.ingede.com/ingindxe/methods/ingede-method-11-2018.pdf (accessed August 2018).

[6] Zhang, Y.; Wu, J.; Wang, H.; Meredith, J. C.; Behrens, S. H. Stabilization of liquid foams through the synergistic action of particles and an immiscible liquid. *Angew. Chem. Int. Ed. Engl.* **2014,** *53* (49), 13603-13607.

[7] Zhang, Y.; Allen, M. C.; Zhao, R. Y.; Deheyn, D. D.; Behrens, S. H.; Meredith, J. C. Capillary foams: Stabilization and functionalization of porous liquids and solids. *Langmuir* **2015,** *31* (9), 2669-2676.

[8] Zhang, Y.; Wang, S. C.; Zhou, J. R.; Benz, G.; Tcheimou, S.; Zhao, R. Y.; Behrens, S. H.; Meredith, J. C. Capillary foams: Formation stages and effects of system parameters. *Ind. Eng. Chem. Res.* **2017,** *56* (34), 9533-9540.

[9] Engineering toolbox. Available at: https://www.engineeringtoolbox.com (accessed August 2018).

[10] Dortmund data bank. Available at: http://www.ddbst.com (accessed August 2018).

[11] Dielectric constants of common materials. Available at: https://www.kabusa.com/Dilectric-Constants.pdf (accessed August 2018).

[12] Table of dielectric constants of pure liquids. Available at: http://www.dtic.mil/dtic/tr/fulltext/u2/a278956.pdf (accessed August 2018).

[13] Schulze, H. Schwefelarsen in wässriger lösung. *J. Prakt. Chem.* **1882,** *25*, 431-452.

[14] Hardy, W. B. A preliminary investigation of the conditions which determine the stability of irreversible hydrosols. *Proc. R. Soc. London, Ser. A* **1900,** *66* (426), 110-125.

CHAPTER 6. CONCLUSIONS AND FUTURE WORK

6.1 Conclusions

Oil-coated bubble (gas bubble coated with a thin film of oil) displays many interesting properties because of its unique structure. Inspired by our previous studies on capillary foam (which consists of oil-coated bubble as the unit structure) and the current challenges in selective solid-liquid separation processes, we explored a new principle in froth flotation that will facilitate the separation of those components from aqueous dispersions or slurries that are not easily removed by traditional flotation because of their unfavorable interaction with gas bubbles.

We started by investigating the fundamental aspects of oil-coated bubbles. Oil-coated bubble flotation is found to exhibit advantages over the traditional method from the following perspectives: 1) thermodynamics: for some hydrophilic particles, the adsorption energy benefit is higher at the oil-water interface compared to air-water interface, therefore particles attach more strongly to the interface; 2) kinetics: the particle adsorption barrier is lower at the oil-water interface compared with air-water interface, therefore particles adsorb onto the oil-water interface more readily; 3) hydrodynamics: oil-coated bubbles rising in water display lower rising velocity, reduced magnitude of lateral excursions and more spherical shape compared with uncoated bubbles. These hydrodynamic differences can be beneficial to the flotation process. For example, lower rising velocity means the bubbles can stay longer in the slurry, therefore having more opportunities to interact with the particles.

Next, we are interested to evaluate its performance to separate some less hydrophobic or even mildly hydrophilic particles, which are usually difficult to separate using the current technology. Inspired by our previous studies on capillary foams, we have developed a simple and convenient method – a foaming test to evaluate the abilities of particles to be collected and separated by gas bubbles. Particles that can create a noticeable amount of capillary foams typically indicate high affinity to the oil-water interface, therefore are more likely to be separated using oil-coated bubble flotation.

Finally, we focused on an industrially-relevant separation system to examine the performance of oil-coated bubble flotation. Flotation de-inking is such an interesting application where the newer type of hydrophilic ink particles are difficult to separate with current technology, but which might be accomplished with oil-coated bubble flotation. It is also a convenient system to investigate, because the absorbance of ink particles at UV-vis wavelength range allows for quantitative evaluation of the flotation performance. The ink particle also serves as a good model to demonstrate the broader applications of oil-coated bubble flotation for separating other hydrophilic particles. In this study, flotation de-inking using both uncoated and oil-coated bubbles was performed with miniaturized and larger-scale tests. System parameters including oil type, salt type, salt concentration and pH were systematically evaluated. We found that oil-coated bubble flotation often dramatically outperforms the standard technique with uncoated bubbles; the highest ink removal efficiency was observed in systems containing multivalent salts at low pH when using bubbles coated with 1-octanol. This work sheds light on the mechanism of oil-coated bubble flotation in the separation of less hydrophobic or even mildly hydrophilic particles, and is expected to trigger broader interests in many other separation systems.

6.2 Future Work

6.2.1 Bubble Rise Dynamics

In Chapter Three, we have presented the dynamics of oil-coated bubbles rising in water, but only focused on completely engulfed oil-coated bubbles.[1] It would be interesting to carry out a parallel study on partially engulfed oil-coated bubbles because not all the oils have a positive spreading coefficient and are able to completely engulf the gas bubbles. Some people may argue that the partially engulfed oil-coated bubbles will not perform well because the bubble surfaces are not fully utilized for particle attachment. In the meantime, however, some previous studies have suggested that the particle-bubble attachment occurs mainly in the "rear end" of the bubbles,[2-3] therefore there should be no difference in particle separation between these two types of oil-coated bubbles. In the future, a systematic study will be very instructive to see whether there is any difference in their rise dynamics and to what extent it may impact the flotation performance.

In addition, our simulation for the rise dynamics of oil-coated bubbles is based on a crude and simplified single-phase representation of these bubbles, which neglects the bubbles' actual composite structure and does not consider the flow recirculation within the thin film. To obtain more precise simulation results, a more realistic multi-phase representation of the oil-coated bubbles will be required.

6.2.2 Measurement of Particle Adsorption Energy Barrier

As presented in Chapter Two, there exists some particle adsorption energy barrier at the interface, and it is shown to be lower at the oil-water interface than that at the air-water interface based on some theoretical estimation. A more precise and convincing experimental determination will be necessary to confirm this claim. Our preliminary experimental results were based on the dynamic surface tension measurement using pendant bubble (or droplet) method. However, as pointed out by some recent studies,[4-7] the pendant bubble (or droplet) falls into the diffusion-limited region, therefore the kinetic adsorption energy barrier is not well revealed. As an alternative, the micro-tensiometer developed by Alvarez et al.[7] is promising for further investigation, because the bubble or droplet size is below the critical value and the particle mass transfer is truly controlled by the adsorption/desorption kinetics.

6.2.3 Flotation De-Inking

The real flotation de-inking process includes the following essential steps: [8]

- Ink particles detach from the fibers;
- Ink particles collide with the air bubbles (or oil-coated bubbles)
- The collision must provide sufficient energy to overcome the repulsive forces between the particles and the bubbles in order to form a stable complex;
- The air bubble must carry ink particles to the top;
- The air bubble/ink particle complex must be removed and cannot be recycled back into the slurry.

The detachment of ink particles from fibers is a pre-requisite step to ensure good ink removal efficiency, but was not investigated in our study. In addition, after we introduce oil to the de-inking system, it will be necessary to evaluate oil carryover and oil

consumption, to ensure this new method is feasible both technically and economically.[9-11]

6.2.4 Oil-Coated Bubble Flotation for Polycyclic Aromatic Hydrocarbons Removal

Polycyclic aromatic hydrocarbons (PAHs) are organic compounds with at least two aromatic rings, and they usually come with great human health risks. PAHs may enter the environment through industrial burning, such as coal plants, from which dust or sediment enters surface waters and attaches to the soil. Extracting PAHs from soil has proven to be difficult since PAHs have low water solubility, absorb tightly to soil particles and are resistant to chemical breakdown. Although some companies that are responsible for the PAHs contamination are aware of the potential risks of exposure, they do not have a strong incentive to clean up contaminated sites since it is cheaper to pay the government fines instead of finding a solution to clean the sites. Some methods such as accelerated solvent extraction[12] and microwave-assisted solvent extraction[13] have been reported to remove PAHs from soil, but they may not be economic and efficient, and therefore a better solution is needed.

We believe the oil-coated bubble flotation method might be promising to address this separation challenge in situ. A section of the river can be isolated with walls. In this walled section, a carrier gas and a solvent can be pumped below the soil, such that the PAHs can be carried by oil-coated bubbles to the top of the water, where they can be skimmed off readily. It would be very interesting to evaluate the feasibility of this method in the future.

6.2.5 Customizable Flotation

We have shown that after coating with a thin film of oil, gas bubbles are able to selectively separate some certain particulates from water (for instance, some less hydrophobic or even mildly hydrophilic particles, which are difficult to remove with current methods). For broader applications of oil-coated bubble flotation, it will be very instructive to learn whether "chemically matching" the oil coat to the particle target provides a substantial added benefit. Recently, our group have explored a broader range of particle-oil combinations that have high affinity (such as hydrophobic-hydrophobic interaction, π-π interaction and acid-base interaction).[14] Future work will be meaningful to demonstrate the feasibility of "affinity flotation".

6.3 References

[1] Wang, S. C.; Zhang, Y.; Meredith, J. C.; Behrens, S. H.; Tripathi, M. K.; Sahu, K. C. The dynamics of rising oil-coated bubbles: Experiments and simulations. *Soft Matter* **2018,** *14* (14), 2724-2734.

[2] Verrelli, D. I.; Koh, P. T. L.; Nguyen, A. V. Particle–bubble interaction and attachment in flotation. *Chem. Eng. Sci.* **2011,** *66* (23), 5910-5921.

[3] Nguyen, A. V.; Evans, G. M. Attachment interaction between air bubbles and particles in froth flotation. *Exp. Therm Fluid Sci.* **2004,** *28* (5), 381-385.

[4] Pan, R. N.; Green, J.; Maldarelli, C. Theory and experiment on the measurement of kinetic rate constants for surfactant exchange at an air/water interface. *J. Colloid Interface Sci.* **1998,** *205* (2), 213-230.

[5] Jin, F.; Balasubramaniam, R.; Stebe, K. J. Surfactant adsorption to spherical particles: The intrinsic length scale governing the shift from diffusion to kinetic-controlled mass transfer. *J. Adhes.* **2004,** *80* (9), 773-796.

[6] Alvarez, N. J.; Walker, L. M.; Anna, S. L. Diffusion-limited adsorption to a spherical geometry: The impact of curvature and competitive time scales. *Phys. Rev. E.* **2010,** *82* (1).

[7] Alvarez, N. J.; Walker, L. M.; Anna, S. L. A microtensiometer to probe the effect of radius of curvature on surfactant transport to a spherical interface. *Langmuir* **2010,** *26* (16), 13310-13319.

[8] McKinney, R. W. J. Technology of paper recycling. 1994.

[9] Zhu, J. Y.; Tan, F. Y. On fiber rejection loss in flotation deinking. *Can. J. Chem. Eng.* **2005,** *83* (2), 377-382.

[10] Deng, Y. Effect of fiber surface chemistry on the fiber loss in flotation deinking. *Tappi J.* **2000,** *83* (6), 61.

[11] Deng, Y. L.; Abazeri, M. True flotation and physical entrainment: The mechanisms of fiber loss in flotation deinking. *Nordic Pulp & Paper Res. J.* **1998,** *13* (1), 4-9.

[12] Giergielewicz-Mozajska, H.; Dabrowski, L.; Namiesnik, J. Accelerated solvent extraction (ase) in the analysis of environmental solid samples - some aspects of theory and practice. *Crit. Rev. Anal. Chem.* **2001,** *31* (3), 149-165.

[13] Basheer, C.; Obbard, J. P.; Lee, H. K. Analysis of persistent organic pollutants in marine sediments using a novel microwave assisted solvent extraction and liquid-phase microextraction technique. *J. Chromatogr. A* **2005,** *1068* (2), 221-228.

[14] Essenmacher, D. S. Particle affinity for oil-water interfaces and selective adsorption. Master's Thesis., Georgia Institute of Technology. 2018.